A SEARCH FOR ASTROPHYSICAL ULTRA HIGH ENERGY NEUTRINOS WITH THE ANITA-IV EXPERIMENT

by

Peng Cao

A dissertation submitted to the Faculty of the University of Delaware in partial fulfillment of the requirements for the degree of Doctor of Philosophy in Physics

Fall 2018

A SEARCH FOR ASTROPHYSICAL ULTRA HIGH ENERGY NEUTRINOS WITH THE ANITA-IV EXPERIMENT

by

Peng Cao

Approved: _____

Edmund Nowak, Ph.D.
Chair of the Department of Physics and Astronomy

Approved: _____

John Pelesko, Ph.D.
Interim Dean of the College of Arts and Sciences

Approved: _____

Douglas Doren, Ph.D.
Interim Vice Provost for Graduate and Professional Education

I certify that I have read this dissertation and that in my opinion it meets the academic and professional standard required by the University as a dissertation for the degree of Doctor of Philosophy.

Signed: _____

John Clem, Ph.D.
Professor in charge of dissertation

I certify that I have read this dissertation and that in my opinion it meets the academic and professional standard required by the University as a dissertation for the degree of Doctor of Philosophy.

Signed: _____

David Seckel, Ph.D.
Member of dissertation committee

I certify that I have read this dissertation and that in my opinion it meets the academic and professional standard required by the University as a dissertation for the degree of Doctor of Philosophy.

Signed: _____

Matthew Decamp, Ph.D.
Member of dissertation committee

I certify that I have read this dissertation and that in my opinion it meets the academic and professional standard required by the University as a dissertation for the degree of Doctor of Philosophy.

Signed: _____

Liao Li, Ph.D.
Member of dissertation committee

I certify that I have read this dissertation and that in my opinion it meets the academic and professional standard required by the University as a dissertation for the degree of Doctor of Philosophy.

Signed: _____

Stephanie Wissel, Ph.D.
Member of dissertation committee

I certify that I have read this dissertation and that in my opinion it meets the academic and professional standard required by the University as a dissertation for the degree of Doctor of Philosophy.

Signed: _____

Dermott Mullan, Ph.D.
Member of dissertation committee

ACKNOWLEDGEMENTS

First of all, I'm extremely grateful to my advisor, Dr. John Clem, for giving me this excellent opportunity to work on the ANITA project. Needless to say, Dr. Clem's patience and guidance is responsible for both my research and study. Achieving both Computer Science Master and Astro-particle Physics Ph.D. in the same period would not have been possible without the support and nurturing of Dr. Clem.

Secondly, I would also like to extend my deepest gratitude to Dr. David Seckel because his help with my research was an invaluable resource. Dr. Seckel's excellent insight in physics always impress me and guide me through the last five years of research.

I would like to express my deepest appreciation to my committee: Dr. Liao Li, Dr. Stephanie Wissel, Dr. Matthew Decamp and Dr. Dermott Mullan for their valuable advice in my Ph.D. defense and profound belief in my work.

Furthermore, I would like to extend my sincere thanks to the whole ANITA collaboration, where I was granted the opportunity to meet and work with a variety of bright and enthusiastic minds. Without their excellent work there is no change for me to complete my dissertation. Especially thanks to Dr. Cosmin Deaconu who is so smart, patient and always give me an immediate response. Thanks should also go to Dr. Ben Strutt for the knowledge and experiences I honed from his presentations and thesis. Many thanks to Dr. Linda Cremonesi for her help in IceMC simulation. I also had a great pleasure of working with Andrew Ludwig, and he is my battle companion in the University of Chicago. I gratefully acknowledge the help from Dr. Steven Prohira's in the analysis of the Hical data. I would like to acknowledge the help from Dr. Ben Rotter. I very much appreciate John Russell, who provide Antarctica's base information. Thanks to Dr. Patrick Allison and Dr. Oindree Banerjee for their work

in TUFFs. Finally, I cannot leave the University of Delaware without mentioning the most experienced ANITA individuals, who organized the collaboration and discussions: Dr. Peter Gorham, Dr. Abby Vieregg, Dr. Ryan Nichol, Dr. Amy Connolly, Dr. David Saltzberg, Dr. Martin Israel, Dr. Andrew Romero-Wolf, among others involved with the team.

I must also thank Dr. Daniel De Marco for his great help in GSE programming. Thanks should also go to Dr. Katherine Mulrey and Dr. Amir Javaid who guided me at the beginning of my ANITA journey. I also had great pleasure of working with Matt Collins and Victor Arriaza in building WebANITA. I would also like to thanks Elle Bornemann for her help in my dissertation writing.

At last, I am deeply indebted to my parents. They always understand and support me to pursue dreams in physics. Pursuing a Ph.D. degree abroad isn't easy, but even more difficult is leaving my parents at home to further my education career. I would like to extend my sincere thanks to all my friends who gave me encouragement and patience throughout my Ph.D. study.

TABLE OF CONTENTS

LIST OF TABLES

LIST OF FIGURES

ABSTRACT

The Antarctic Impulsive Transient Antenna (ANITA) is a balloon-based experiment designed to search for ultra-high energy(UHE) neutrinos and cosmic rays in Antarctica. A successful detection would be an important step in understanding the most energetic cosmic accelerators in the universe. The fourth flight of ANITA (ANITA-IV) funded by NASA took place in December 2016. It uses a radio antenna array designed to detect Askaryan radiation from UHE neutrino-induced showers in ice and geomagnetic radiation from Extensive Air Showers (EAS) induced by cosmic rays.

In this dissertation, I present my analysis of the ANITA-IV flight data with the objective to search for ultra-high energy neutrino and cosmic ray events. The data analysis includes six major aspects: instrument calibrations, event direction reconstruction, event quality cuts, thermal events cut, anthropogenic events cut (clustering), and background estimation. Twenty-four cosmic ray candidates and one neutrino candidate events were found each with an estimated background of 0.34 event. Although the signal significance for a single neutrino event is consistent with background, it still leads to the world's best limit on the ultra-high energy neutrino flux for energy above 4×10^{19} eV.

Chapter 1

ULTRA HIGH ENERGY PARTICLES AND THEIR DETECTIONS

1.1 Introduction

Observations of our universe are accomplished by using detectors to record messenger particles produced by stars or galaxies and propagated through the universe. Using optical light is the classical way, which has a history of thousands of year. Over the last century, astronomers began to look at spectra other than visible light. Moreover, other high energy particles like protons and neutrinos open a new window into the universe. The detection of high energy particles, such as protons, nuclei, neutrinos and photons, makes up the modern multi-messenger astronomy. Section 1.2 introduces the properties of these fundamental particles and their interactions in the Standard Model.

Cosmic rays (CR) are high energy particles, most of which are protons and nuclei. Cosmic rays also include high energy photons (gamma rays), neutrinos and electrons. Protons and nuclei can be accelerated from energetic sources, propagate through the universe and be detected on the Earth. Gamma rays and neutrinos are usually the products from cosmic rays interacting with photons and matter either in the source or during propagation. Electrons can be accelerated in the same way as protons, however they can not travel a long distance in the universe since they are charged and have low mass. The energy spectrum of cosmic rays spans more than twelve decades: from 10^8 eV to 10^{20} eV. The origin of cosmic rays varies from the solar system and our galaxy to extra-galactic sources at an Ultra High Energy (UHE), which is larger than 10^{18} eV. An overview of cosmic ray detection, spectrum and origin is presented in Section 1.3.

Astrophysical neutrinos are distinguished from other CRs because they are neutral particles that rarely interact with matter. The only means to detect neutrinos is through the weak interaction. So far astrophysical neutrinos have been observed from three sources: the Sun, SuperNova 1987a and blazar TXS 0506+056. IceCube has also demonstrated a diffuse flux at energy larger than 10^{14} eV. UHE neutrinos, i.e above 10^{18} eV, can be produced from Ultra High Energy Cosmic Rays (UHECR) interacting with Cosmic Microwave Background (CMB) photons. UHE neutrinos are messengers which open up a new window to the universe where photons and cosmic rays are limited. An overview of neutrino properties, interactions, production and detection in laboratory and natural processes is presented in Section 1.4.

Although there are many ways to detect UHE cosmic rays and neutrinos, in this work we focus on the mechanism of the Antarctic Impulsive Transient Antenna (ANITA) radio techniques. ANITA is a series of balloon-borne experiments that flew over Antarctica, searching for impulsive radio signals. An UHE neutrino could generate a particle cascade (or shower) in the ice that produces Askaryan radiation. An UHE cosmic ray could generate an Extensive Air Shower (EAS) in the atmosphere that produces geomagnetic radiation. Both Askaryan radiation and geomagnetic radiation are impulsive RF signals that the ANITA experiments have been searching for since 2004. Section 1.5 discusses the mechanism of how radio signals are generated from incident UHE neutrinos or cosmic rays as well as a brief introduction to ANITA's impact on UHE astrophysics.

The other chapters focus on the details of the ANITA-IV experiment. Details about the ANITA-IV instrument and hardware are provided in Chapter 2. Data telemetry to the ground and the system of ground support software, maintained and developed by myself, are introduced in Chapter 3. A summary of the ANITA-IV flight is described in Chapter 4. In Chapter 5, the event reconstruction and calibration are explained in detail, which are the foundation of my data analysis in Chapter 6. In Chapter 7, I summarize my analysis results and give an outlook on the future of UHE neutrino astronomy.

1.2 The Standard Model

Despite the complexity of our universe, there are simply four fundamental interactions in physics describing almost every phenomenon. These four interactions are electromagnetic, weak and strong interactions and gravity. The first three can be combined into the Standard Model (SM), which is a $U(1) \times SU(2) \times SU(3)$ gauge theory of quantum fields. After a spontaneous symmetry breaking, the low energy model becomes $U(1)_{EM} \times SU(3)_{color}$ via the Higgs mechanism. In Figure 1.1, all the fundamental particles in the SM are divided into fermions and bosons. The fermions are half-integer spin particles, such as quarks q and leptons l with spin $\frac{1}{2}$. The bosons are integer spin particles, such as photons γ, weak bosons $W^{\pm}$ and Z^0, and gluons g with spin 1, and the Higgs boson h with spin 0. Each particle may carry one or more quantum numbers such as electric charge, weak isospin, and color charge.

The three interactions in the Standard Model can be viewed as a process of exchanging bosons between fermions. For example, the electromagnetic interaction is viewed as exchanging photons γ between fermions with electric charge. The weak interaction is viewed as exchanging $W^{\pm}$ and Z^0 between fermions with weak isospin. The strong interaction is viewed as exchanging gluons g between the fermions with color charge. The Higgs boson was the last particle of the Standard Model to be observed[28]. It is the remaining electrically neutral component of the Higgs field after the symmetry breaking of the electroweak interaction. The other components of the Higgs field are "absorbed" by the gauge bosons. The Higgs mechanism provides mass to the $W^{\pm}$, Z^0, and the charged leptons and quarks.

The quarks have six flavors which are in three generations of weak isospin doublets:

$$\begin{pmatrix} u \\ d \end{pmatrix} \begin{pmatrix} c \\ s \end{pmatrix} \begin{pmatrix} t \\ b \end{pmatrix}$$

Quarks carry electric charges, weak isospins and color charges so they are involved in all the three interactions. Similarly, the leptons have six flavors and are in three

generations of weak isospin doublets:

$$\begin{pmatrix} e \\ \nu_e \end{pmatrix} \begin{pmatrix} \mu \\ \nu_\mu \end{pmatrix} \begin{pmatrix} \tau \\ \nu_\tau \end{pmatrix}$$

While all leptons carry weak isospin, leptons e, μ and τ carry electric charge. Leptons ν_e, ν_μ and ν_τ, known as the neutrinos, do not carry any electric charge. Since the neutrinos only carry weak isospin, they can only interact with matter through the weak interaction.

Due to the infra-red behavior of the strong interaction, the quarks and gluons can never be found isolated, and they are always confined into colorless hadrons. The hadrons have two types: 1) baryons formed by three quarks, such as protons (uud) and neutron (udd); 2) mesons formed by quark and anti-quark pairs, such as $\pi^+(u\overline{d})$, $\pi^-(\overline{u}d)$, $\pi^0(\frac{1}{\sqrt{2}}(u\overline{u} - d\overline{d}))$ and other heavier mesons. The electrons, photons and atomic nuclei formed by protons and neutrons give rise to the most common matter and forces in our daily experience. The messenger particles of interest, neutrinos and gamma rays, are mostly produced in the decay of mesons produced by pp or $p\gamma$ collisions. Most important are the decays of π^0 and $\pi^\pm$, which produce gamma rays and neutrinos:

$$\begin{aligned} \pi^0 &\to \gamma + \gamma \\ \pi^+ &\to \nu_\mu + \mu^+ \\ \mu^+ &\to \nu_e + e^+ + \overline{\nu}_\mu \end{aligned} \tag{1.1}$$

These decays are not only the source for the messenger particles but also the most important processes for describing air cascades.

1.3 Cosmic Ray Overview

Cosmic rays are high energy particles, i.e. protons, nuclei, electrons, photons and neutrinos, that propagate through the universe and bombard the Earth. The most abundant cosmic rays are protons and nuclei, presumably accelerated in energetic sources and then propagate over a long distance with small energy loss. Electrons may also be accelerated but they lose energy quickly during the propagation. Gamma rays

Figure 1.1: The Standard Model with elementary particles. Figure from [1].

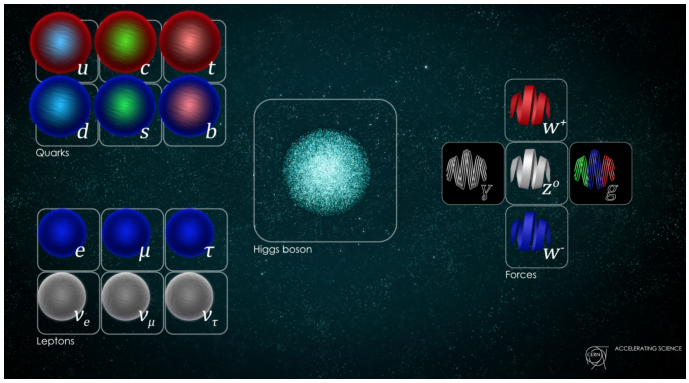

and neutrinos are not accelerated directly in the sources but could be produced in interactions either in the sources or during propagation of the cosmic rays. Gamma rays with energy above TeV interact with extra-galactic photons via $\gamma\gamma \rightarrow e^+e^-$ and their energy cascades to a multitude of 10-100 GeV gamma rays. The detection of gamma rays and neutrinos is a useful probe to explore the origin of cosmic rays. Since ANITA's purpose is to look for neutrinos, a separate overview of neutrinos is given in Section 1.4. This section focus on the detection, spectrum and origin of hadronic based cosmic rays.

1.3.1 Cosmic Ray Detection

When cosmic rays impact the Earth's atmosphere, they collide with air nuclei and produce cascades of many secondary particles, known as Extensive Air Showers (EAS). This cosmic radiation was discovered in 1912 by Hess through a series of balloon flights and the radiation was assumed to be primarily gamma rays, and consequently coined cosmic rays (CR) by Milliken. The observed ionizing radiation measured by the balloon-borne instrumentation increased [29] as the balloon ascended to 4800 m, implying the radiation did not originate from the Earth, but was instead arriving from space. It was later observed the flux of cosmic rays also has a strong variation with latitude implying the incident trajectories at the top of the atmosphere are influenced

by the geomagnetic field and therefore composed of mostly electrically charged particles [30].

In 1939 Auger showed that coincident radiations from different particle detectors in the Alps were associated with a single air shower [31], which launched a new era of studying cosmic rays. In 1962 John Linsley detected a 10^{20} eV cosmic ray using a particle detector array [32], which led to a hypothesis that UHECRs have extra-galactic origins. In the 1990s, the AGASA experiment claimed to observe a continuous cosmic rays spectrum above 5×10^{19} eV. However, the HiRes experiment observed a cutoff of UHECR flux. Although the discrepancy was later explained by calibration uncertainty, the question of where the UHECR energy spectrum ends drew the attention of astrophysicists. Larger detectors were built in recent decades, such as Pierre Auger Observatory (PAO) and Telescope Array (TA), with hybrid surface detectors and fluorescence detectors to provide better sensitivity to cosmic rays.

1.3.2 Cosmic Ray Spectrum

The cosmic ray energy spectrum is shown in Figure 1.2. For energy below the "knee" (3 PeV), the spectrum follows an $E^{-\alpha}$ power law, where $\alpha = 2.7$. A zoomed spectrum starting from the knee is shown in Figure 1.3. The spectral index α increases to 3 from the knee to the "ankle" (3 EeV) and then begins to decrease. The cosmic rays below the knee have a galactic origin, most commonly thought due to the Fermi acceleration mechanism in supernova remnants [33]. The cosmic rays above the ankle are thought to be of an extra-galactic origin. The shape of the spectrum near the ankle may be explained as the transition between the galactic and extra-galactic sources, complicated by a "dip" due to proton and nucleus energy losses as they propagate through the intergalactic medium [34]. There are two hypotheses to explain the cutoff near 10^{20} eV. One hypothesis is the cosmic rays already reach the maximum energy that the astrophysical objects can accelerate and contain. The other hypothesis is that extra-galactic protons interact with photons in the Cosmic Microwave Background

Figure 1.2: Cosmic Ray Energy Spectrum of Various Experiments. [2]

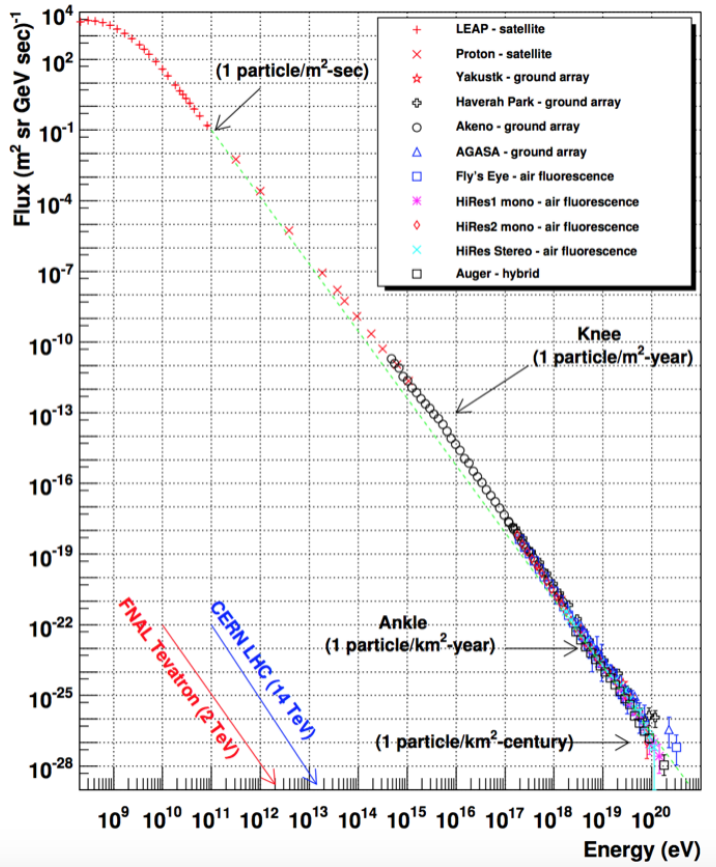

(CMB) via a process known as the GZK effect [35, 36]. See more discussions in Section 1.4.6.

1.3.3 Cosmic Ray Sources

The source of cosmic rays below the knee is thought to be shock acceleration in supernova remnants which have sufficient magnetic field and energy to contain and accelerate the cosmic rays. The Fermi mechanism describes that electrically charged particles gain energy through repeated reflection off magnetic structures in the converging flow at the shocks present in supernova remnants. It predicts an $\alpha = 2$ cosmic ray spectral index for non-relativistic shocks and $\alpha = 2.3$ for relativistic shocks. The

Figure 1.3: The energy spectrum per particle from air shower measurements. The spectrum has been multiplied by $E^{2.6}$ to reveal the slope changes in the spectrum. [2]

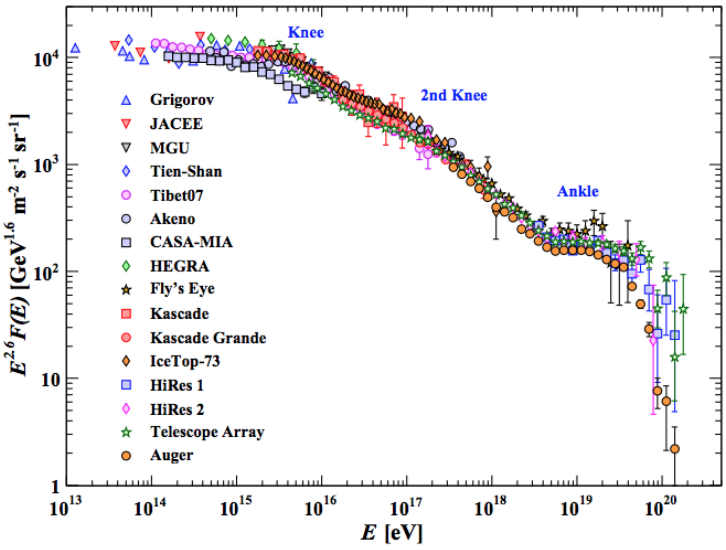

difference with the measured cosmic ray flux $\alpha = 2.7$ can be explained as higher energy cosmic rays are more likely to escape from our galaxy.

It is still a mystery how the cosmic rays are accelerated above the knee. From the knee to the ankle, one possibility is to extrapolate the Fermi acceleration mechanism with a second unknown population of galactic objects. The astrophysical structures that can produce shocks, such as AGNs and GRBs, are the most plausible sources for UHECRs. The gyro-radius of cosmic rays must be confined by the maximum size of the accelerator: $R = \frac{m\gamma v}{qB}$, where R is the characteristic size of the astrophysical structure, $m\gamma v$ is the relativistic momentum of the particle, q is the charge of the particle which equals to Ze, B is the magnetic field for the astrophysical structure. As a result, the maximum energy of the cosmic rays that can be accelerated can be estimated by $E_{max} = ecZBR$, where Z is the number of protons in the nuclei, e is the proton's charge, and c is the speed of light. In Figure 1.4, the plausible sources are plotted in a $\log B - \log R$ space [3]. The red and blue lines are the thresholds to produce a 10^{21} eV proton and 10^{20} eV iron nuclei respectively. The source for UHECR is thought to be

Figure 1.4: An updated Hillas Plot of the most powerful candidate UHECR sources shown with uncertainties in the plot [3]. Above the blue line protons can be confined to a max energy of 10^{20} eV. Above the red line iron nuclei can be confined to a max energy of 10^{20} eV.

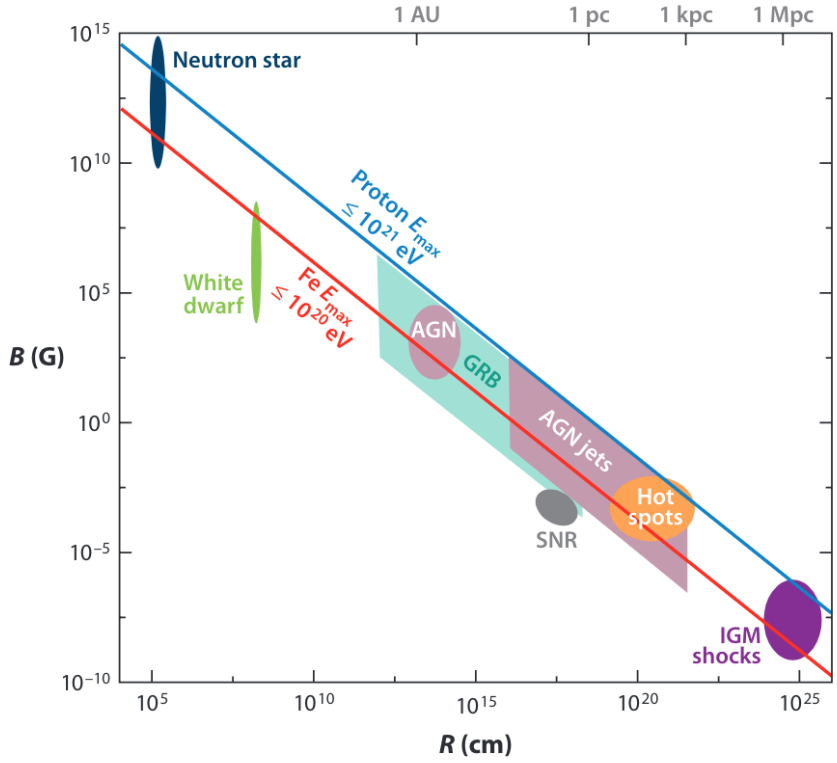

extra-galactic because UHECR would escape from our galaxy, of which the thickness is about 10^{21} cm and the magnetic field is about 10^{-6} G. Figure 1.4 suggests two possible extra-galactic sources for UHECR: active galactic nuclei (AGN) and gamma ray bursts (GRB), which can produce relativistic jets and shocks to accelerate cosmic rays to UHE.

1.3.4 Gamma Rays

Gamma rays are high energy photons. They cannot be accelerated directly by the electromagnetic field, and they are thought to be produced from high energy cosmic rays either leptonically via inverse Compton or as a result of hadronic processes. At high energy CRs interact with CMB/IR/OPT/UV photons and produce π^0 and $\pi^{\pm}$. π^0

will decay into gamma rays and $\pi^{\pm}$ will decay into neutrinos and other particles. The gamma rays could form electromagnetic cascades from pair production and inverse-Compton radiation, producing a spectrum of gamma rays which will be shown in Figure 1.8.

The detection of gamma rays is similar to the detection of cosmic rays since they both produce particle cascades in media. Although it is difficult, modern experiments, such as MAGIC, HESS, VERITAS, Fermi LAT and HAWC, can distinguish them in following two ways: 1)gamma rays point back directly to the sources while charged cosmic rays are diffuse due to propagation, creating an excess in skymaps of detected events; 2)cascades from gamma rays have less hadronic component than those of cosmic rays, leading to cascades that have smoother profiles (Section 1.5) and fewer muons.

1.4 Neutrino Overview

In 1930, neutrinos were first postulated by Wolfgang Pauli to explain how beta decay conserves energy and momentum. He considered that an undetected neutral particle, in addition to an electron, was emitted from the nucleus in beta decay:

$$n \rightarrow p^{+} + e^{-} + \overline{\nu}_{e}.$$

In 1956, Clyde Cowan and Frederick Reines detected reactor neutrinos [37] via inverse beta decay:

$$\overline{\nu}_{e} + p^{+} \rightarrow n + e^{+}.$$

Both positron annihilation and neutron capture can produce detectable gamma rays indicating a $\overline{\nu}_{e}$ interaction. In 1962, Leon Lederman, Melvin Schwartz and Jack Steinberger first found evidence to distinguish ν_{μ} from ν_{e} [38], suggesting a lepton flavor symmetry as part of the SM. In 2000, the DONUT collaboration at Fermilab announced the detection of ν_{τ} by observing the decay of τ leptons [39].

1.4.1 Neutrino Interactions

Neutrinos are mainly involved in the weak interaction by exchanging $W^{\pm}$ or Z^0 with other fermions. Depending on whether $W^{\pm}$ or Z^0 is exchanged, there are two types of interactions, Charged Current (CC) and Neutral Current (NC) interactions. The Feynman diagrams for these two interactions are shown in Figure 1.5.

In the Standard Model, the neutrino's cross-section with nuclei increases as the energy increases as shown in Figure 1.6 [6]. At UHE, the cross-section between ν and electrons can be neglected in comparison with the cross sections between ν and nuclei. The interaction length in matter for neutrinos can be calculated using the cross section and density of matter. For example, a 10^{19} eV neutrino has an interaction length of 150 km in rock and 400 km in water. As a result, the Earth is opaque to UHE neutrinos.

1.4.2 Solar Neutrinos

Solar neutrinos are produced through various fusion chains which process $4p \rightarrow He + 2e^+ + 2\nu_e$. The energy spectra of neutrinos from different reactions are shown in Figure 1.7.

In the early 1970s, the Homestake Mine Experiment [40] observed that the flux of solar ν_e was less than expected. The so called "solar neutrino problem", was not solved until 2000. The Sudbury Neutrino Observatory (SNO) [41] confirmed that the total solar neutrino flux was consistent with the solar nuclear reaction model but their flavor distribution was not. This phenomenon of neutrino changing flavor can be explained by neutrino oscillations: the flavor eigenstates ν_e, ν_μ, ν_τ are not equal to the mass eigenstates ν_1, ν_2, ν_3. Moreover, the flavor eigenstates can be transformed from a linear combinations of the mass eigenstates as follow:

$$\begin{bmatrix} \nu_e \\ \nu_\mu \\ \nu_\tau \end{bmatrix} = \begin{bmatrix} U_{e1} & U_{e2} & U_{e3} \\ U_{\mu 1} & U_{\mu 2} & U_{\mu 3} \\ U_{\tau 1} & U_{\tau 2} & U_{\tau 3} \end{bmatrix} \begin{bmatrix} \nu_1 \\ \nu_2 \\ \nu_3 \end{bmatrix}.$$

The 3×3 matrix is known as the Pontecorvo–Maki–Nakagawa–Sakata (PMNS) matrix [42]. In this framework, as the neutrinos propagate, the distribution of flavor could

Figure 1.5: The Feynman diagrams for CC and NC interactions between neutrinos and electrons and nuclei. Note the lepton scattering diagrams only interfere for the ν_e case. They would be separate processes for ν_μ and ν_τ. The $\overline{\nu}$ diagrams are not shown here. They look similar except for $\overline{\nu}_e e^- \rightarrow W^-$, which is an s-channel process leading to the Glashow resonance. The νN scattering takes place via underlying νq or $\nu \overline{q}$ sub-processes. Figure from [4].

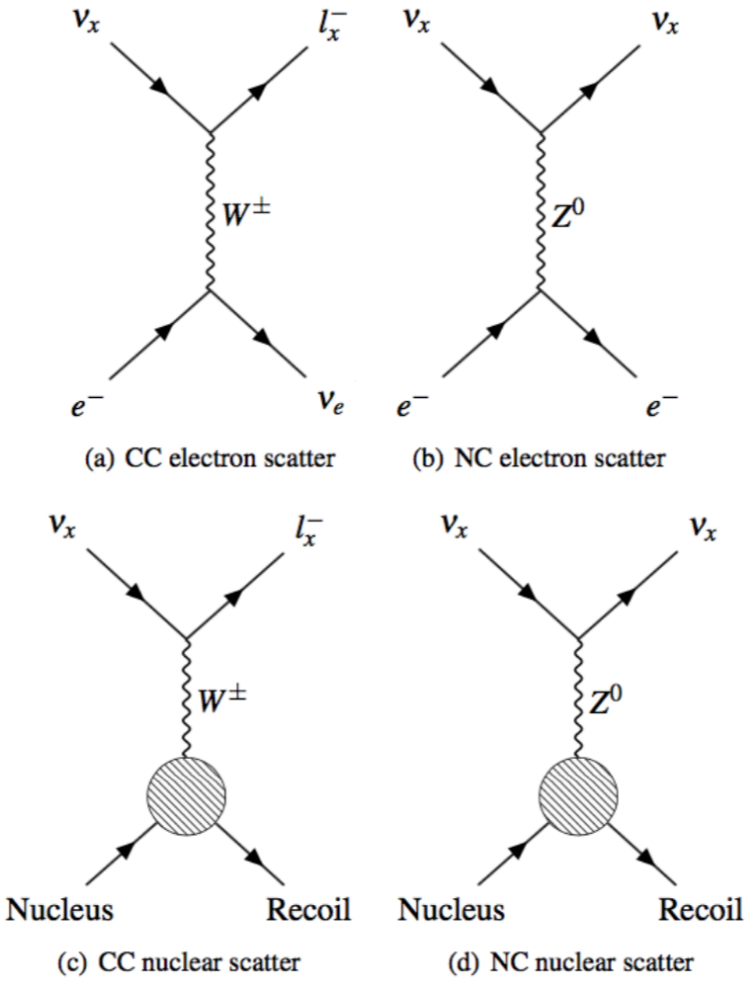

Figure 1.6: Left: the cross sections for νN interactions, where N is an isoscalar nucleon averaged by proton and neutron. CTW uses MSTF parton distribution functions. GQRS is an older model using CTEQ parton distribution functions [5]. The dotted line refers to NC interactions. The dashed line refers to CC interactions. The solid line refers to the total interaction. Right: the cross sections for $\overline{\nu}N$, which is similar to the left plot at high energy but different at low energy. Figure from [6].

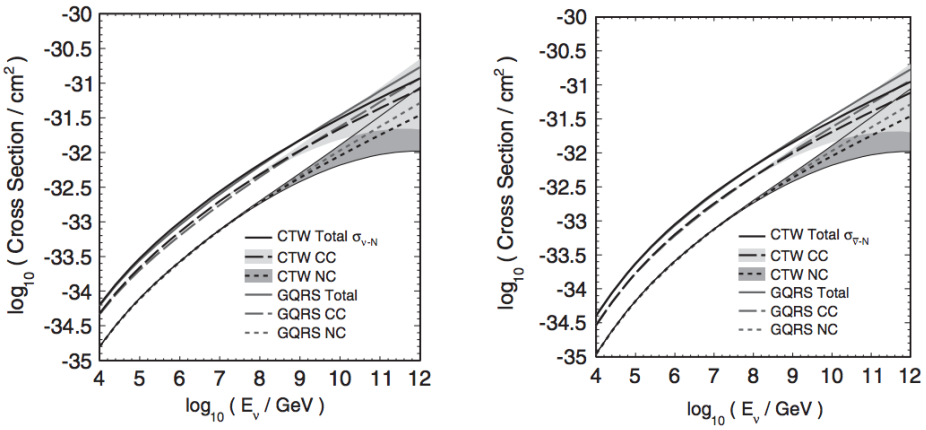

oscillate as a function of distance and energy. The phenomenon of neutrino oscillation were confirmed by the Sudbury Neutrino Observatory (SNO) [41] and Super-Kamiokande Observatory (SK) [43].

1.4.3 Atmospheric Neutrinos

As cosmic rays enter the Earth's atmosphere, they can produce showers of particles, including $\pi^{\pm}$ and $K^{\pm}$, which are unstable and may decay into atmospheric neutrinos, μ and other particles. See more in Section 1.5.1. The atmospheric neutrinos extend from below GeV to above a hundred TeV in energy and they are produced uniformly around the Earth. In the 1980s, the Kamiokande and Irvine–Michigan–Brookhaven (IMB) experiments observed a deficit of ν_{μ} propagating through the Earth, providing strong evidence for neutrino oscillations [44, 45]. This was later interpreted as ν_{μ} and ν_{τ} oscillations within the PMDS framework [43]. Atmospheric neutrinos are background for all astrophysical neutrinos experiments up to 100 TeV and other low background

Figure 1.7: The solar neutrino spectrum from different nuclear reactions. [7]

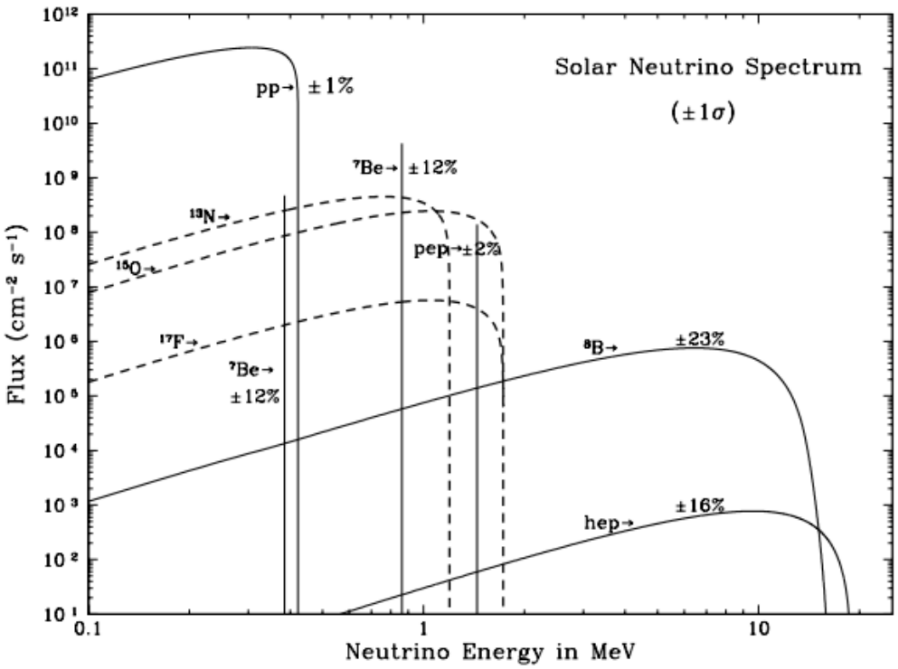

experiments. For example, Kamiokande and IMB experiment were designed to detect proton decay but atmospheric neutrinos are always background to these experiments.

1.4.4 Artificial Neutrinos

Nuclear reactors are sources of artificial neutrinos. About 5% of fission power are released as antineutrinos [46], which are generated from the beta decay of the nuclear fission products. An average nuclear power plant can produce 30000 antineutrinos/sec but only 3% of them are above the detection threshold of 1.8 MeV.

Particle accelerators can also be used to produce neutrino beams. The method is to bombard a fixed target with a proton beam, focus the resulting $\pi^{\pm}$ and produce a neutrino "beam". The generated neutrino beam can be detected locally or travel thousands of km to a detector as part of long baseline neutrino oscillation experiments.

1.4.5 Astrophysical Neutrinos

In 1987 a supernova (SN1987a) was observed in the Large Magellanic Cloud, a satellite galaxy of the Milky Way. A burst of neutrinos with energy of a few MeV was produced by SN1987a and it was the first astrophysical neutrino event observed from a known source other than the Sun. As a star collapses to form a very dense neutron star, the core of the star enters into a thermal equilibrium of extremely hot photons, electrons and neutrinos. Since neutrinos have longer interaction length than other particles, they can penetrate through the surface of the star and almost all of the gravitational energy is released as neutrinos. This neutrino burst was recorded by Kamiokande II experiment [47] and IMB experiment [48].

In seven years of IceCube data (through 2018), more than 100 astrophysical neutrinos have been detected between 100 TeV and 10 PeV [8]. The neutrino flux is shown in Figure 1.8 and it is the state of the art for measuring the neutrino flux above 100 TeV. These neutrino events do not exhibit any significant anisotropy in their distribution, indicating they originated from extra-galactic sources.

Figure 1.8: The astrophysical neutrino flux is observed by IceCube (black line) and the gamma ray spectrum flux by Fermi (red line). The blue area indicates the best fit for the ν_μ flux. Cosmic rays could be the original source for both of these spectra. See more in Section 1.5.1. The background of atmospheric neutrinos prevents identification of astrophysical neutrinos below ~ 100 TeV. [8]

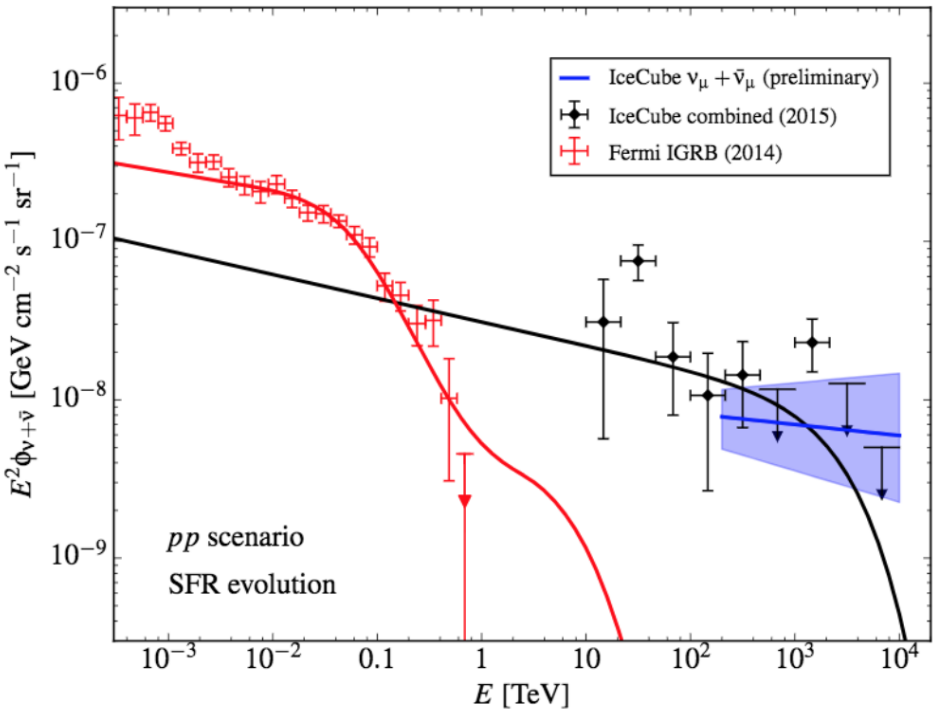

In Sept 2017, IceCube saw a neutrino event (above 300 TeV) from blazar TXS 0506+056 [49]. The space-based Fermi-LAT and ground-based MAGIC air Cherenkov telescope showed activities in γs. Also IceCube looked back at its data and found an excess of ν_μ events above background from the same source in Dec 2014 [50]. Blazar TXS 0506+056 is a massive black hole with powerful jets, which is 5.7 billion light years from the Earth. This exciting news is the first-ever identification of a likely extra-galactic high energy neutrino source.

1.4.6 GZK Effect and Cosmogenic Neutrinos

In 1966, Kenneth Greisen, Georgiy Zatsepin, and Vadim Kuzmin predicted the GZK effect through theoretical calculation. When an UHE proton's energy is larger than 5×10^{19} eV, it starts to interact with CMB photons (with energies of order 10^{-3} eV) through the Δ resonance [35]:

$$\begin{aligned} \gamma_{CMB} + p &\rightarrow \Delta^+ \rightarrow p + \pi^0 \\ \gamma_{CMB} + p &\rightarrow \Delta^+ \rightarrow n + \pi^+ \end{aligned} \tag{1.2}$$

The cross-section for these processes are such that, given the presence of several hundred CMB photons per cm^3 in the universe, the attenuation length for UHE protons is found to be around 50 Mpc. This GZK process can be calculated in the center of mass frame, where the photon and proton's momenta cancel out. When the center-of-mass energy of the collision reaches the mass of Δ^+, they form the Δ^+ resonance which quickly decays into π^0 or π^+.

If the UHECR are mainly composed of protons, then we would expect a cut off at the energies of 5×10^{19} eV in the cosmic ray spectrum, known as the GZK cutoff. As discussed in Section 1.2, π^0 and π^+ are unstable particles and will easily decay. Gamma rays are produced from π^0 decay and cosmogenic neutrinos are produced from $\pi^\pm$ decay. The energy of the neutrinos from π^+ decay is less than the original proton by a factor of ten. Other facts are that the CMB was hotter in the early universe decreasing the effective GZK threshold and neutrinos produced in the early universe experience a cosmological redshift during propagation. As a result, the UHECR from

Figure 1.9: The cosmogenic neutrino flux model (black line) from several interaction mechanisms if UHECR were composed of pure protons. All the simulations are made under an SFR1 and dip model. SFR1 is one of the star formation rate models that describe the source emissivity. The dip model invokes energy loses due to pair production to explain the CR spectrum at the ankle. The green line represents the cosmogenic neutrino flux from the interaction between UHECR and CMB photons. The blue line represents the cosmogenic neutrino flux from the interaction between UHECR and IR/UV/OPT photons. The red line represents the cosmogenic neutrino flux from neutron decay. [9]

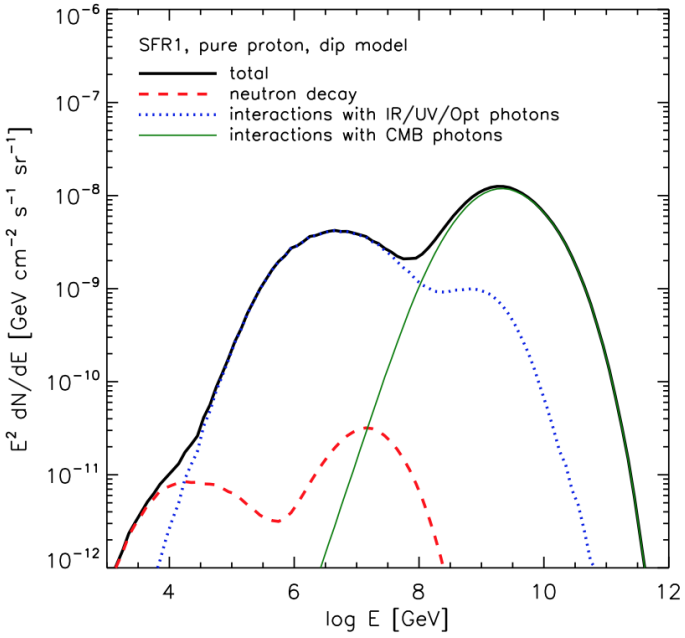

the early universe (further distance) tend to have a lower GZK cutoff. Figure 1.9 shows the UHE neutrino (UHEN) flux model if the UHECR were composed entirely of protons.

Recent results from the PAO (Auger) experiment indicate that the UHECR component is mainly iron nuclei instead of protons alone [51]. Since the energy per nucleon is the total energy of an UHECR divided by the number of nucleons, this feature leads to a significantly higher GZK cutoff at 2.5×10^{21} eV. The situation is more complex since iron rapidly loses energy via pair production and experiences fragmentation. The uncertainty of UHECR composition still exists because the UHECR from the Auger

Figure 1.10: The UHEN flux models for different assumed composition models. The black line is the UHEN flux model by pure proton assumption, and it is the same as the black line in Figure 1.9. The purple dotted line has an assumption of mixed composition. The dark blue line has an assumption of a pure iron composition. The red dashed line has the assumption of pure iron composition and lower accelerator maximum energy [9].

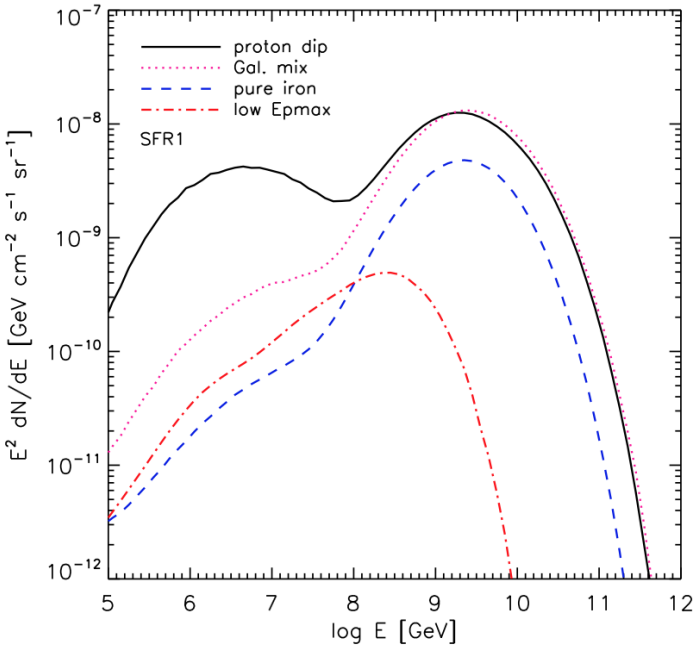

Figure 1.11: The macroscopic distance from the Earth to the Universe.

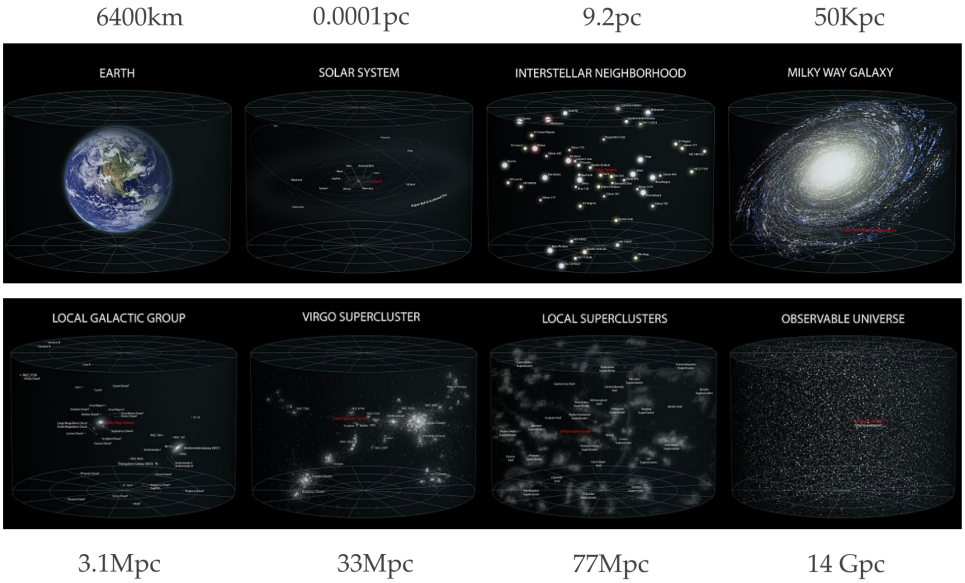

experiment [52] originate in the local universe. It may not be true that UHECR sources at high red shift have the same composition. Even so, as a consequence of a heavier composition in CR, the latest cosmogenic neutrino models have a lower expected neutrino flux than before. Figure 1.10 compares the UHEN flux model with different UHECR compositions.

1.4.7 Messengers of UHE Universe

Figure 1.11 lists the length scales from the Earth, galaxy, to the universe. As discussed in Sections 1.2, 1.3 and 1.4, high energy photons, protons, and neutrinos are created by related astrophysical processes. Their observation contributes to modern multi-messenger astronomy. However, each messenger particle has a different horizon as shown in Figure 1.12. For example, a high energy photon could be absorbed by pair production with a CMB photon (or infra-red photon). A high energy proton deflects in the galactic magnetic field, so it cannot trace back to the accelerator source. A high energy neutron decays during its inter-galactic propagation, so it does not survive the passage from source to Earth. On the other hand, a neutrino propagates in an

undeflected path between its source and the Earth. Moreover, the neutrinos only interact with matter through the weak interaction. The arrival direction of a neutrino is not affected by the electromagnetic field in the universe. Their observation opens a window into the universe on the extra-galactic scale.

1.5 Radio Detection of Ultra High Energy Cosmic Particles

When UHE particles interact at the Earth, they produce cascades which can be detected either directly from high energy particles in the cascades or remotely through the radiation produced from the cascades. The radiation could be optical Cherenkov or fluorescent light, acoustic signals or, as for ANITA, radio emissions. The incident UHE particles, such as neutrinos and cosmic rays, can produce particle cascades as discussed in Section 1.5.1. Each charged particle in a cascade is a source of electromagnetic radiation as shown in Section 1.5.2. An UHE neutrino produces Askaryan radiation through a particle cascade in the ice (Section 1.5.3). An UHECR produces geomagnetic radiation through Extensive Air Showers (EAS) (1.5.4). The mechanism of ANITA experiments to detect both UHE neutrinos and cosmic rays are introduced in Section 1.5.5. The impact of ANITA is discussed in Section 1.5.6.

1.5.1 Particle Cascades

When an UHE particle enters a medium and interacts, lower energy secondary particles are produced in the interaction. Each secondary particle may also interact, producing another generation of secondary particles, in a process that continues, resulting in a cascade or shower of particles. The particle population continues to grow and reaches a maximum when the average energy is too low to produce additional secondary particles. The population then decays as particles continue to lose energy and eventually are absorbed in the medium. The geometry of the shower is an important feature for the detection of UHECR or UHE neutrino. The particle density of a

Figure 1.12: The horizon of messengers, i.e. protons, photons, and neutrinos, at different energy scales. The highest energies of observed protons and gamma-rays are labeled in the plot. At an energy of 10^{20} eV, the protons can only be detected from the local universe. The protons have an attenuation length of 100 Mpc due to the GZK effect. As a result, we could not observe the proton from the red shaded area. Gamma rays can interact with the infra-red photons and CMB photons through pair production, thereby excluding them from being UHE messengers. We could not observe the photons from the blue shaded area. For neutrinos, the whole universe is transparent up to 10^{25} eV [10]. Plot by Peter Gorham from private communication.

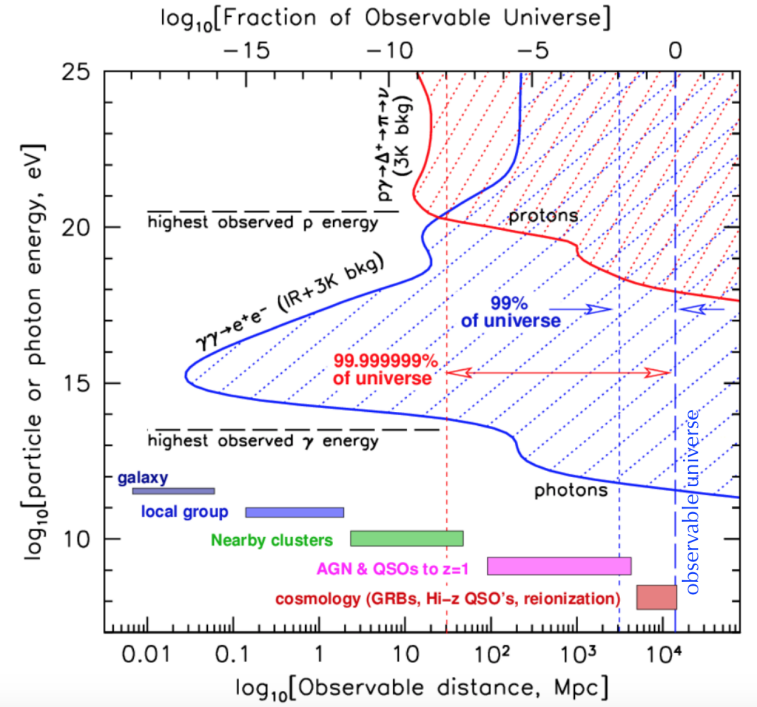

cascade ρ can be characterized by the longitudinal development N, transverse profile f and shower thickness h as follows [53]:

$$\rho_i(x, y, z, t) = N_i(t) f_i(r, t) h_i(\widetilde{z}, r, t) \tag{1.3}$$

where t is the time, i is the index of a particle species, r is the radius from shower axis and $\widetilde{z} = z - ct$. One may distinguish two types of cascades, electromagnetic and hadronic, which are described in turn.

Electromagnetic cascades are initiated by gammas or electrons. There are two major processes contributing to the multiplicity evolution of electromagnetic cascades: bremsstrahlung and pair production [54]. Bremsstrahlung is the process by which high-energy electrons and positrons emit gamma rays when they are deflected by other nuclei. Pair production is the process by which the gamma rays produce electron-positron pairs as they pass through the Coulomb field of the nucleus. As an electromagnetic cascade evolves, the number of particles N increases exponentially, and the average energy of particles decreases until it reaches the critical energy (E_c), where the ionization energy loss rate is equal to the radiation energy loss rate. The shower max X_{max} is defined as the shower depth at this critical energy. The number of particles N in the cascade ceases to increase and reaches the maximum N_{max}. X_{max} and N_{max} can be estimated by:

$$X_{max} = X_0 \ln \frac{E_0}{E_c} \tag{1.4}$$

$$N_{max} \sim \frac{1}{\ln (E_0/E_c)} \frac{E_0}{E_c} \tag{1.5}$$

where E_0 is the initial particle energy, E_c is the critical energy and the radiation length X_0 is defined by the energy losses for high energy electrons with $E \gg E_c$:

$$\frac{dE}{dx} = -\frac{E}{X_0} \tag{1.6}$$

X_0 depends on the medium and is in a unit of g/cm^2. For example, $X_0 = 37\ g/cm^2$ in air and $X_0 = 36\ g/cm^2$ in ice [55]. The physical length of the cascade is proportional

to $\frac{X_0}{\rho}$, where ρ is the density of the medium. From equation 1.4 the distance to shower max scales as $\ln E_0$. From equation 1.5 the maximum number of particles in the shower is proportional to the initial energy E_0. The transverse profile of the cascade is due to Coulomb scattering off the nuclei, which can be approximately described as a Gaussian distribution. Moliere radius is defined as the size of a cylinder that contains 90% of the shower energy, and it can be estimated by:

$$R_M = X_0 \frac{E_S}{E_c} \tag{1.7}$$

where $E_S \approx 21$ MeV [56]. The shower thickness can be roughly estimated as $h \sim X_0(1 - \cos\theta) \approx 0.05X_0$, where $\theta \approx R_m/X_0 \approx 0.3$ is the angular spread because the transverse dimension is small comparing to the radiation length. A full cascade simulation is necessary to get accurate shower thickness.

Hadronic cascades are initiated by nuclei or mesons as primary particles or by recoil quarks in deep inelastic scattering, e.g. by neutrinos. The basic feature of a hadronic cascade is that the outgoing particles of a nuclear interaction can produce hadronic particles such as π^0,$\pi^\pm$, K^0 and $K^\pm$. Almost 1/3 of the interaction energy goes to neutral π^0 mesons, which quickly decay to two gamma rays and initiate an electromagnetic cascade. The other mesons ($\pi^\pm, K^0, K^\pm$) may re-interact to produce more secondary mesons continuing the evolution of the hadronic cascade. Alternatively, they may decay into leptons (Equation 1.1) forming atmospheric muons and neutrinos. Muons are heavy leptons with relatively long interaction lengths, which may decay ($\mu^- \rightarrow \overline{\nu}_e + e^- + \nu_\mu$) or lose energy and stop in the medium. Figure 1.13 shows an example of a cosmic ray induced atmospheric cascade. On the left, a hadronic cascade begins with a p-nucleus reaction. Then the electromagnetic and μ components develop from the hadronic cascade. On the right, the number of shower particles N changes as a function of shower depth X.

In dense media, such as ice and salt, the cascades also contain electromagnetic cascades and hadronic cascades. The major effect of a dense media is that the scale of cascades is proportional to the inverse of density. As a result, both longitudinal profile

Figure 1.13: Left: Cosmic ray air shower components. [11] Right: the mean longitudinal profiles for gamma ray, proton and iron cascade at an energy of 10^{19} eV from MC simulation. The shaded band represents the upper and lower limits at 68% confidence level. [12]

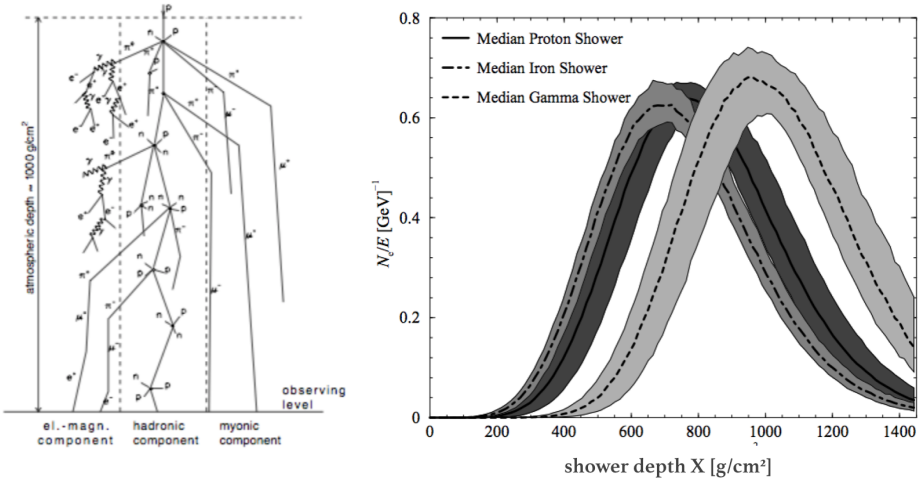

and transverse profile of cascades in dense media are much smaller than in air. Another effect is the LPM effect, where the high energy cross-sections for bremsstrahlung and pair-production decrease in dense media and, as a consequence, the longitudinal profile of electromagnetic cascades increase. In hadronic cascades, the $\pi^{\pm}$ mostly interact with the matter before decaying. So the energy of hadronic cascades is more easily to be transferred to electromagnetic cascades rather than μ and ν.

1.5.2 Electromagnetic Radiation from Moving Particles

The charged particles in cascades can produce electromagnetic radiation as they propagate in the medium. For a short straight segment j of a particle track from a cascade at x_0 and observed at x, the the electric field in the frequency domain can be written as [57]:

$$\boldsymbol{E_j}(\omega, \boldsymbol{x}) = \frac{q_j \mu}{2\pi\epsilon_0 c^2} i\omega \frac{e^{ikR}}{R} e^{i(\omega - \boldsymbol{k}\cdot\boldsymbol{v_j})t_j} \boldsymbol{v_j}_{\perp} \frac{e^{i(\omega-\boldsymbol{k}\cdot\boldsymbol{v_j})\delta t_j} - 1}{i(\omega - \boldsymbol{k}\cdot\boldsymbol{v_j})}, \tag{1.8}$$

Figure 1.14: Illustration of the Cherenkov radiation. v is the speed of particle and c/n is the speed of light in the medium. Left: when $v < c/n$ the radiation wavefront is still spherical. Right: when $v > c/n$, the radiation wavefront forms a light shock wave, which is known as Cherenkov radiation.

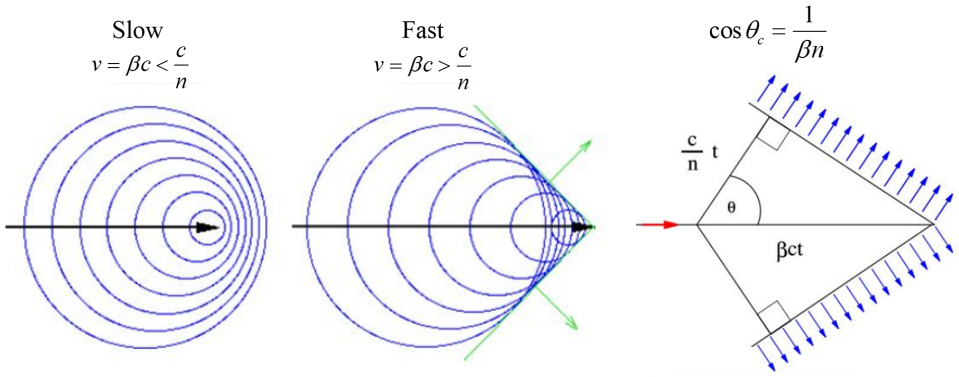

where $q_j = Z_j e$ is the charge of the moving particle, μ is the magnetic permeability, $\boldsymbol{k} = \frac{n\omega}{c}\hat{\boldsymbol{k}}$ is the wave number, n is the refraction index, $R = |\boldsymbol{x} - \boldsymbol{x_0}|$, $\boldsymbol{v_j}$ is the particle velocity, $\boldsymbol{v_{j\perp}} = \hat{\boldsymbol{k}} \times (\hat{\boldsymbol{k}} \times \boldsymbol{v_j})$ is perpendicular to the direction of radiation $\hat{\boldsymbol{k}} = \frac{\boldsymbol{R}}{|\boldsymbol{R}|}$ from the track segment to the observer, t_j is the start time of a given track segment and δt_j is the total time of the segment track. The equation can be derived from the Lienard-Wiechert potentials using a Lorentz covariant approach [57]. The phase term $e^{i(\omega - \boldsymbol{k}\cdot\boldsymbol{v_j})t_j}$ becomes a constant 1 when $1 - n\beta\cos\theta = 0$, which means all contributions to the radiation add coherently along a Cherenkov angle $\theta_c = \arccos\frac{1}{n\beta}$. Cherenkov radiation is the sum of radiation contributions from a long single particle track (Figure 1.14). More generally radiation from a cascade is modeled by simulating all the tracks in the cascade and adding up the contributions.

1.5.3 Askaryan Effect and Askaryan Radiation

In 1965 Gurgen Askaryan postulated that a cascade of high energy particles in a medium would develop an overall negative charge [58]. At the beginning of a cascade, an equal amount of e^- and e^+ pairs are generated. As the shower propagates, atomic electrons e^-_{atomic} in the matter can interact with e^+, e^- and gamma rays in the shower.

Several interaction channels are shown in Figure 1.15. Atomic electrons e^-_{atomic} become free and join the cascade or may annihilate e^+. As a result, there will be 20 - 30% more negative charge than positive charge in the shower [59].

Moreover, the constructive interference of radiation from the negative charge current can produce an impulsive radio frequency (RF) signal, known as Askaryan radiation. Equation 1.8 can be used in conjunction with a particle cascade simulation to track each individual particle and sum all their electric fields. An example of the ZHS Monte Carlo simulation is shown in Figure 1.16 [57], where a 1 PeV electromagnetic cascade was simulated in ice. The electric field from different observation angles are compared: θ_c is the Cherenkov angle. $\theta_c - 5^\circ$ and $\theta_c - 20^\circ$ are angles off the Cherenkov cone. On the Cherenkov cone, the peak frequency is proportional to the inverse of the Moliere radius R_m of the cascades. As shown in Figure 1.17, the coherence of Askaryan radiation is related to the transverse size of the shower disk. Shorter wavelength radiation tends to interfere destructively and longer wavelength radiation tends to interfere constructively. The width of the Cherenkov cone $\delta\theta$ is inversely proportional to the longitudinal dimension and the observing frequency.

The final radiation power per unit frequency, ΔJ_f, is related to the particle energy as follows:

$$\Delta J_f = \frac{Z^2 e^2 v^2}{c} f \Delta f \approx 3 \cdot (10^{-16} E_0)^2 mW \tag{1.9}$$

The radiation from Askaryan effect has been measured and verified in silica sand [60] and in rock salt at SLAC [61] . Figure 1.18 shows an Askaryan impulsive RF waveform observed in ice at the T486 experiment [14]. As shown in Figure 1.19, the SLAC T486 experiment measured the relation between the electric field and frequency, and verified that the RF power is proportional to the square of the shower energy. The Askaryan effect has also been confirmed in high-density polyethylene (HDPE) at the SLAC T510 experiment [62].

Figure 1.15: The Feynman diagrams for shower particles interacting with atomic electrons. The atomic electron gains energy and joins the shower after the interactions, such as Compton Scattering, Bhabha Scattering, and Moeller Scattering. For annihilation e^+ are subtracted from the cascades, also increasing the net negative charge.

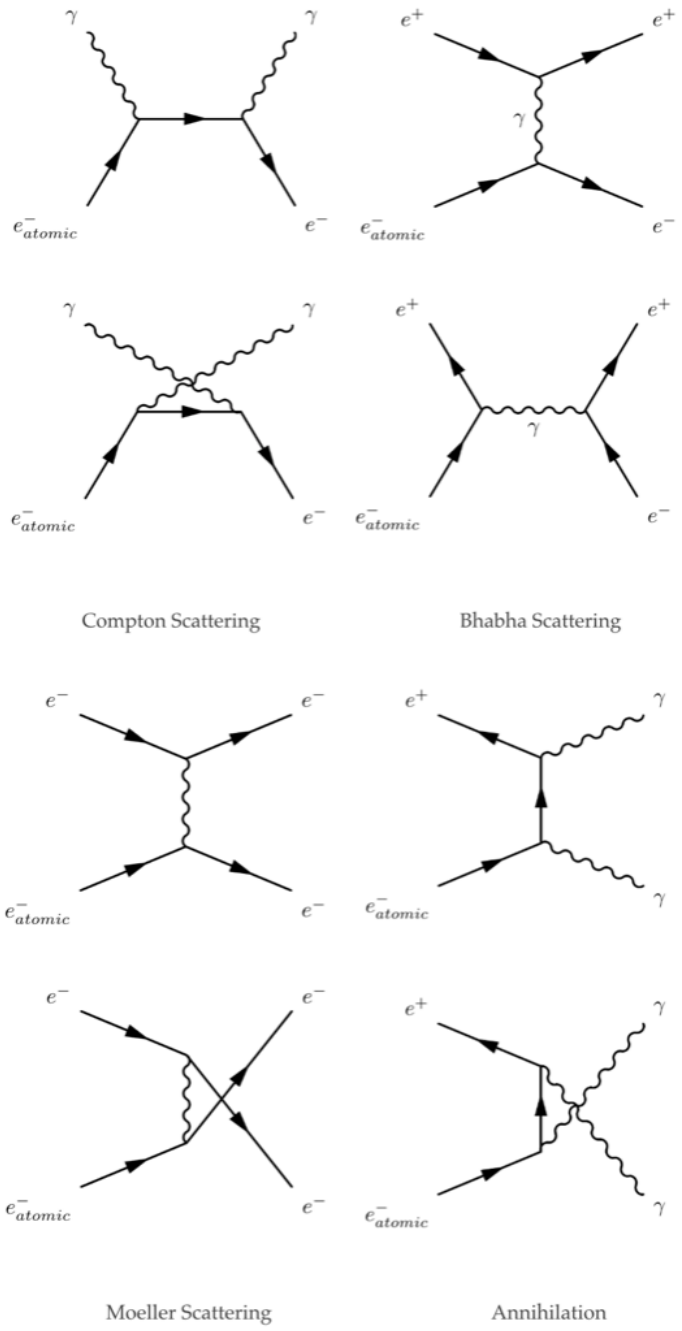

Figure 1.16: The electric field spectrum from various view angles for a 1 PeV electromagnetic shower by ZHS Monte Carlo simulation. Two different time resolutions (the width of sampling time bin), $\Delta T = 0.1$ ns and $\Delta T = 0.5$ ns are used at the Cherenkov angle. The peak frequency of the electric field decreases as an observer moves away from the Cherenkov cone. The amplitude changes as $\hat{\boldsymbol{k}} \times (\hat{\boldsymbol{k}} \times \boldsymbol{v})$ changes. [13]

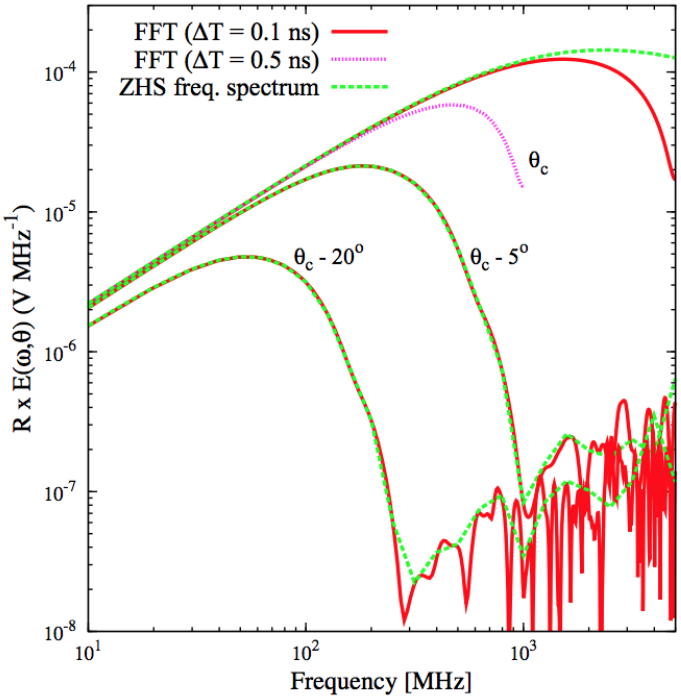

Figure 1.17: "Shower" is a thin disk of primarily electrons and positrons a few mm thick and few cm wide in solids. For wavelengths much greater than the shower width, radiation adds coherently from all the excess electrons while at smaller wavelengths, the radiation experiences destructive interference from electrons from different locations of the shower. At radio wavelengths longer than the size of the shower disk, the shower can be treated as a single charge Ze, where Z is related to the energy of initial particle and the charge excess due to the Askaryan effect.

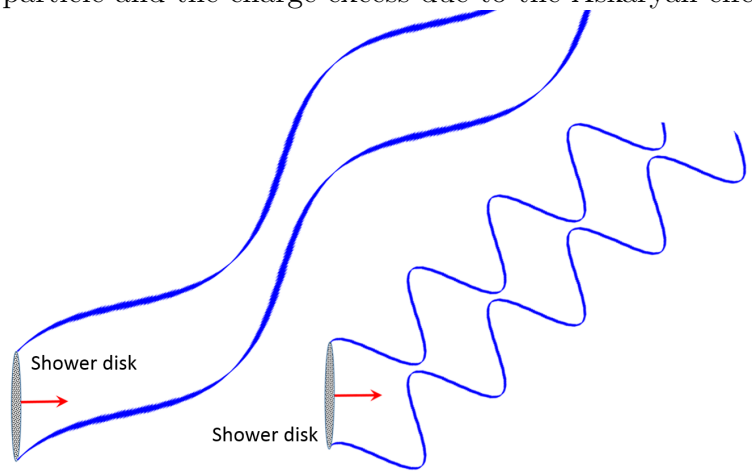

Figure 1.18: The top panel shows the ANITA system response. The bottom shows the recorded waveform by ANITA from Askaryan radiation. The ringing is due to the group delay of the edge response of the bandpass filters. Figure from SLAC T486 experiment. [14]

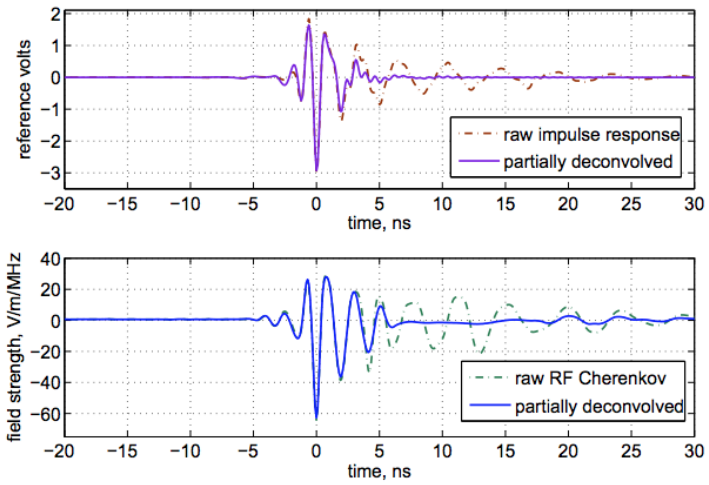

Figure 1.19: Left: electric field vs frequency. The curve is the theoretical expectation. Right: RF total power vs shower energy. It follows quadratic relation as shown in Equation 1.9. Figure from the SLAC T486 experiment [14]

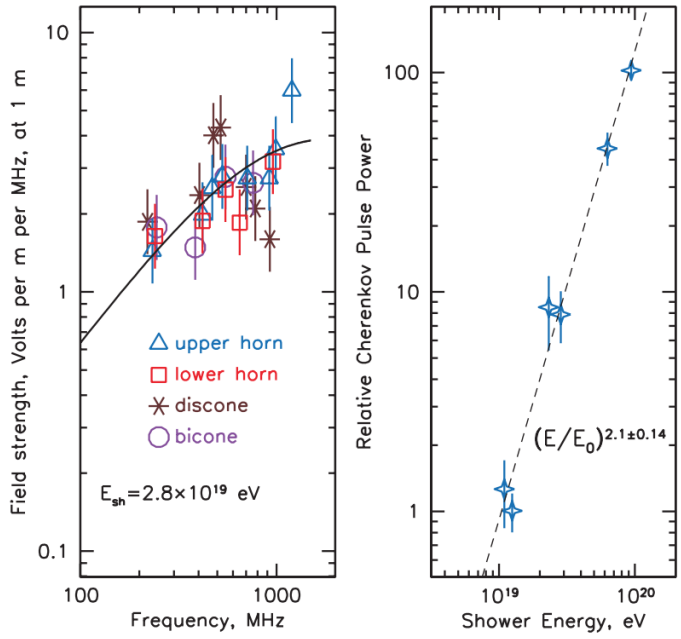

Figure 1.20: Left: The horizontally polarized geomagnetic radiation under the influence of an approximately vertical geomagnetic field. The electron and positron will be deflected in opposite directions under the influence of the geomagnetic field due to the Lorentz force. Right: The Askaryan radiation in air for an EAS event. The plots are made as seen from the direction of the magnetic field. Figure from [15].

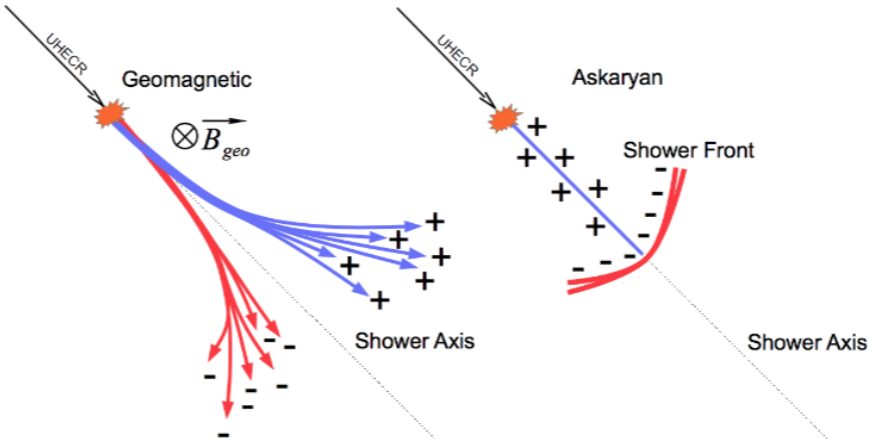

Figure 1.21: Left: RF intensity vs off-axis angle. Using a 10^{19} eV air shower at zenith angle 71°. Right: Radio spectrum for several off-axis angles. [16]

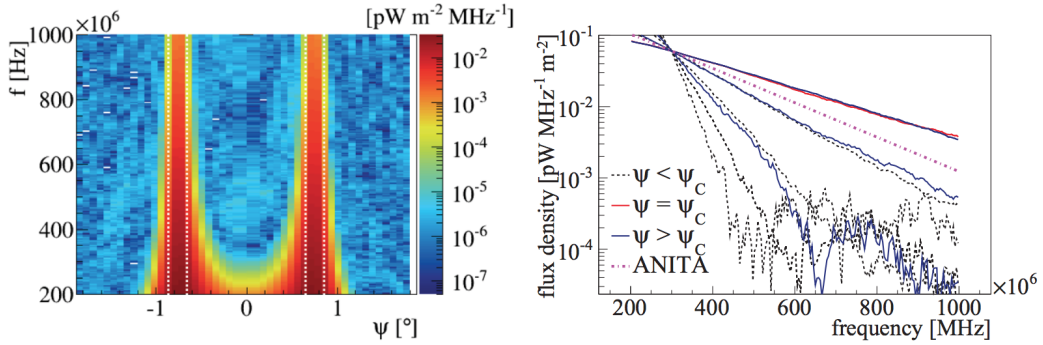

1.5.4 Geomagnetic Radiation from Extensive Air Showers

When cosmic rays propagate into the atmosphere, they interact with nuclei of air molecules to initiate EAS containing electrons, positrons and gamma rays. The high energy particles propagate faster than the speed of light in the air and produce more lower energy charged particles. The pattern velocity of these lower energy charged particles in the EAS is faster than the speed of light in the air, creating coherent radiation at the Cherenkov angle [63].

The polarization of electric field is determined by the term $\boldsymbol{v_{j\perp}} = \hat{\boldsymbol{k}} \times (\hat{\boldsymbol{k}} \times \boldsymbol{v_j})$, as shown in Equation 1.8, where $\boldsymbol{v_j}$ is the velocity of the charged particle for a track segment j. For Askaryan radiation (and Cherenkov radiation from a long single particle track) $\boldsymbol{v_{j\perp}} = \beta c \sin\theta$. For air showers, $1 - n \approx 10^{-4}$ and $\theta_c \approx 10^{-2}$, so the Askaryan radiation is weaker than in dense media. However, due to the Lorentz force of the geomagnetic field, the electrons and positrons gain velocity $v_{perp} = \frac{qvB}{m\rho}\delta t_j$ in opposite directions as shown in the left of Figure 1.20. v_{perp} is perpendicular to the direction of the shower axis and is the transverse component of $\boldsymbol{v_j}$. In this case $\boldsymbol{v_{j\perp}} \sim \cos\theta \approx 1$ for air showers. In Antarctica, the direction of the geomagnetic field is near vertical, so v_{perp} is near horizontal. As a result, this creates a horizontal polarized RF signal known as geomagnetic radiation, which is the major component of EAS radiation [64].

EAS events were detected since the first flight of ANITA. The modern geomagnetic radiation model is well understood, simulated and validated at SLAC T510 [65]. In Figure 1.21, the left plot shows a distribution of Cherenkov angles and the right plot shows the spectrum for an EAS event observed at a various off-axis angles. An energy analysis of 14 ANITA-I EAS events gives an average energy of 2.9×10^{18} eV [63], which is less than the GZK threshold 5×10^{19} eV. Although the details of the radio emissions from EAS and UHE neutrino events are quite different, the analysis to search for them is relatively similar. In analyzing the ANITA-IV experiment, searching for EAS events provides an important validation as we attempt to identify UHE neutrino events in ANITA data.

Figure 1.22: The ANITA detection concept. On the left, a neutrino-induced cascade produces Askaryan radiation. Ice is transparent to RF signals over the range of frequencies which are detected by ANITA (180MHz to 1200MHz). ANITA can receive the refracted RF signal which is dominated by Askaryan radiation with vertical polarization (VPol). On the right, a cosmic ray EAS event produces an RF signal dominated by geomagnetic radiation with horizontal polarization (HPol), which reflects from the ice and is received by ANITA. [17]

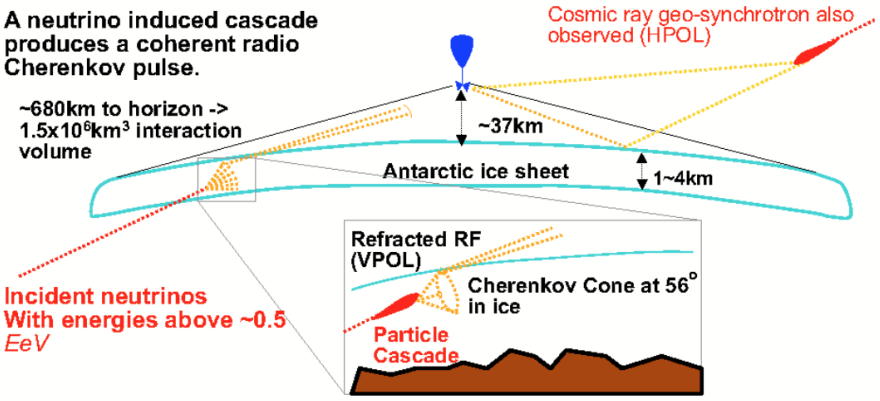

1.5.5 ANITA Experiment

The ANITA experiment is a balloon-borne radio detector designed to collect impulsive RF signals in Antarctica for both UHE neutrinos and cosmic rays [66, 67, 68, 69]. The detection of those two kinds of events is illustrated in Figure 1.22.

For a neutrino event, the Askaryan radiation from the shower vertex in the ice has a long attenuation length O(1000 m). In other words, the ice is relatively transparent to the RF signal. According to measurements at the South Pole, over the range of frequencies which are relevant for ANITA observations, the refractive index in the surface of ice is 1.32, and the refractive index at the deep ice is 1.79 [70]. When the neutrino's incident angle is horizontal, the radiation at the top of the Cherenkov cone will just undergo total internal reflection at the ice surface. This is not by coincidence but due to $\theta_{tol.ref.} + \theta_{Che.} \approx 90°$, where the critical angle is $\theta_{tol.ref.} = \arcsin(n_{air}/n_{ice})$ and the Cherenkov Cone angle is $\theta_{Che.} = \arccos(1/n_{ice})$. However, due to the relatively short longitudinal profile of a cascade in ice, the actual Cherenkov radiation will spread

wider than $\theta_{Che.}$ and the top of the Cherenkov cone can pass through the ice surface as shown in Figure 1.16. The ANITA detector is most sensitive to neutrinos with incoming direction close to horizontal. First, for a neutrino arriving from above the horizontal direction, the Askaryan RF is not likely to pass through the ice surface. Second, for a neutrino arriving from below the horizontal, the neutrino cross-section is such that the neutrino is absorbed on the other side of the Earth. Since only the top part of the Cherenkov cone can emerge from the ice, the radiation generated by a neutrino event, which is detectable by ANITA, is dominated by vertical polarization.

For cosmic ray events, an EAS can produce geomagnetic radiation in air. Since the RF refractive index of air at the shower is close to 1, the Cherenkov angle is so small that the Cherenkov radiation is close to the direction of the cosmic ray. Because the air is very thin in the balloon altitude (37 km), ANITA is not expected to detect cosmic rays coming from directions which are above the horizontal direction ($\theta = 0°$). However, ANITA can detect direct CR and reflected CR events from directions which are below the horizontal direction. For direct CR, the RF signal received by ANITA should arrive from a direction above the horizon of the Earth ($\theta \approx -6°$). For the reflected CR, the RF signal received by ANITA should arrive from a direction which lies below the horizon of the Earth. Since a reflection on the ice would flip the sign of the electric field, the polarity of the waveform for direct CR and reflected CR are opposite. From the explanation in the last section, both CR events have HPol dominated polarization.

In conclusion, the ANITA experiment is looking for impulsive RF events. An UHE neutrino event should be a VPol event from below the horizon (coming from the ice). CR events should be HPol dominated events which arrived along directions that lie below the horizontal. The polarity of a CR event depends on whether it is a reflected or direct event.

1.5.6 Impact of ANITA on UHE Neutrino Physics

Four ANITA flights have been launched successfully. In 2006, ANITA-I stayed aloft for 35 days. In 2008, ANITA-II stayed aloft for 30 days. In 2014, ANITA-III stayed

Figure 1.23: The four ANITA flights. From ANITA-I to ANITA-IV, the colors are red, blue, green and purple. Plot by Ben Strutt from private communication.

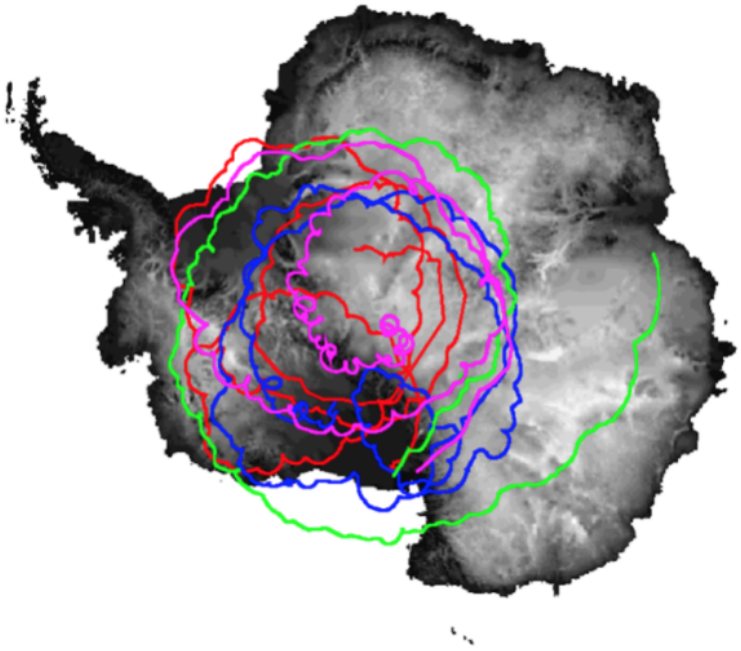

aloft for 22 days. ANITA-IV stayed aloft for 28 days in 2016. The four flight paths are shown in Figure 1.23. These successful ANITA flights demonstrate that the design of the instrument is robust and that the instrument satisfies the flight requirements. The past ANITA flights (before ANITA-IV) put strong constraints on the existing UHE neutrino models. Figure 1.24 summarizes the state of UHEN flux limits from several experiments when ANITA-IV was proposed but before ANITA-III data analysis was finished. A selection of UHE neutrino flux models is also shown in the plot. ANITA-II had the best neutrino flux limit in the UHE and, as a result, it provided constraints on the existing UHEN flux models. IceCube results also put constraints on the neutrino flux limit from PeV to ZeV [71] [72]. Two possible extrapolations of IceCube PeV flux, with spectral index $\alpha = 2.0$ and $\alpha = 2.2$, were used in this plot. Considering that the ANITA-III and ANITA-IV instruments have more and larger antennas and better filters, the neutrino flux limit from those two flights was expected to improve, as shown

Figure 1.24: UHE neutrino flux limits from ANITA-II and IceCube-2013. The expected neutrino flux for a 100-day ANITA-III + ANITA-IV flight is also shown, compared with a selection of UHE neutrino flux models. [16]

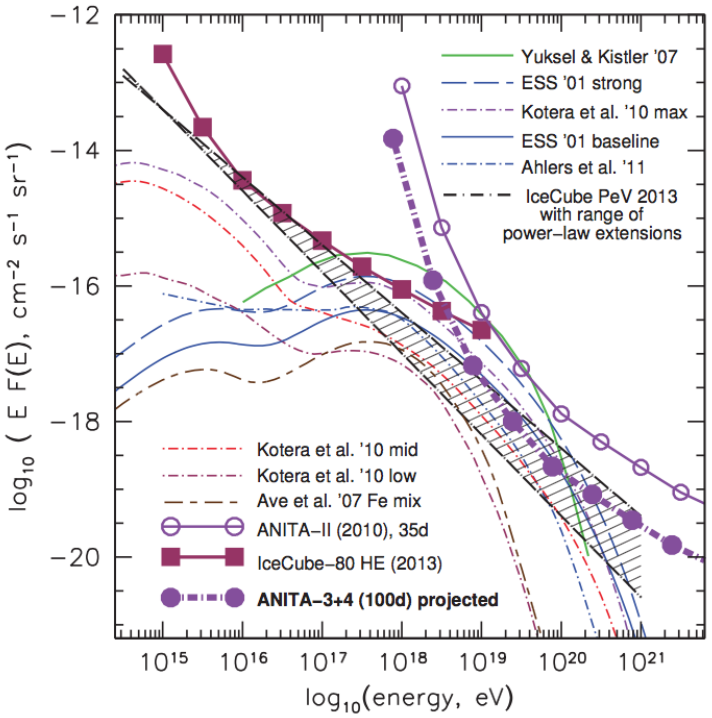

in the figure. However, the real ANITA-III and ANITA-IV flights did not reach the expected 100 day flight time and resulted in a much-reduced neutrino flux limit, which will be discussed in Chapter 7.

ANITA is a pioneering experiment, making the first attempt to detect UHEN with air-borne radio technology. The advantage of the ANITA experiment is that the effective area is larger than for ground-based neutrino radio experiments. In the recent decade, other ground-based radio detection experiments, such as ARIANNA on Ross Ice Shelf [73] and ARA at the South Pole [74], are also in construction and operation. As for IceCube, they embed their detectors in the ice but detect RF rather than visible Cherenkov light. The in ice deployment leads to lower anthropogenic background than ANITA. Since they are closer to the shower vertex, they can set the energy threshold much lower than ANITA, and hope to span the energy gap (10 PeV to 1 EeV) between IceCube and ANITA. Several exciting high-energy astroparticle experiments are also planned: Giant Radio Array for Neutrino Detection (GRAND) [75], AugerPrime [76], TA×4 [77], IceCube-Gen2 [78] and recently proposed Radio Neutrino Observatory (RNO) [79]. Together these complementary experiments will finally characterize a complete picture of UHEN spectrum.

Chapter 2

THE FOURTH FLIGHT OF THE ANTARCTICA IMPULSIVE TRANSIENT ANTENNAS (ANITA-IV)

This chapter describes the hardware details of ANITA-IV payload.

2.1 ANITA-IV Payload

The ANITA-IV payload is an array 48 Seavey antennas in three rings (top, middle and bottom) as shown in Figure 2.1. Each ring contains 16 antennas facing different directions. And the rings are aligned with each other to form 16 phi sectors. Each phi sector has three antennas: one from the top ring, one from mid-ring and one from bottom ring. The phi-angle difference between two adjacent phi sectors is 22.5° ($22.5° \times 16 = 360°$), resulting in an azimuthally symmetric array. All the antennas are canted down 10° for higher sensitivity to an expected ν signal from the ice. The top ring is actually composed of two staggered rings that each has 8 antennas. Figure 2.2 shows the antenna aperture (i.e. the azimuth towards which the antenna is facing) and the antenna center.

Between the middle and top ring, a platform structure supports the instrument, the SIP, and the battery box. The instrument box contains the majority of the ANITA electronics. The NASA Science Instrument Package (SIP) provides bi-direction telemetry for receiving commands to control the payload / sending data to ground. Inside the battery box is the science payload power system that consists of a bank of rechargeable lead-acid batteries and a charge controller. The charge controller charges the batteries using the photo-voltaic (PV) panels which are located below the bottom ring of the payload. The PV panels located on the top of the payload provides power to the SIP and other CSBF flight equipment. More details on each sub-system are discussed in the

Figure 2.1: The view of ANITA-IV payload configuration. Photo from [18].

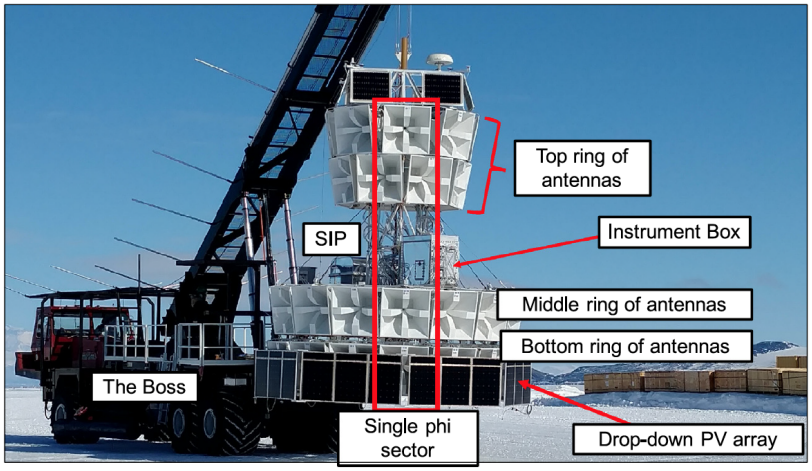

following sections. Figure 2.3 is the photo of the payload right before the ANITA-IV launch in Long Duration Balloon (LDB) station.

2.2 Seavey Antenna

The Seavey antenna is a quad-ridged (two polarization) broadband antenna produced by the Antenna Research Associates, Inc. Figure 2.4 shows several Seavey antennas in the top ring. Each antenna has both horizontal polarization (HPol) and vertical polarization (VPol). The beam pattern and power spectrum are shown in Figure 2.5 and Figure 2.6. Achieving the desired frequency response of the antenna strongly depends on the dimensional constraint in situ. These limitations include the payload launch envelope size requirement and maintaining 16 azimuthal viewing directions, resulting in a maximum size of roughly 1 meter for the antenna. This corresponds to a minimum frequency of roughly 180 MHz. The maximum frequency is limited by the SURF sample rate which corresponds to roughly 1300 MHz. Therefore the antenna bandwidth of 180-1200 MHz was selected.

Figure 2.2: The Seavey aperture and center for each ring, viewed from top.

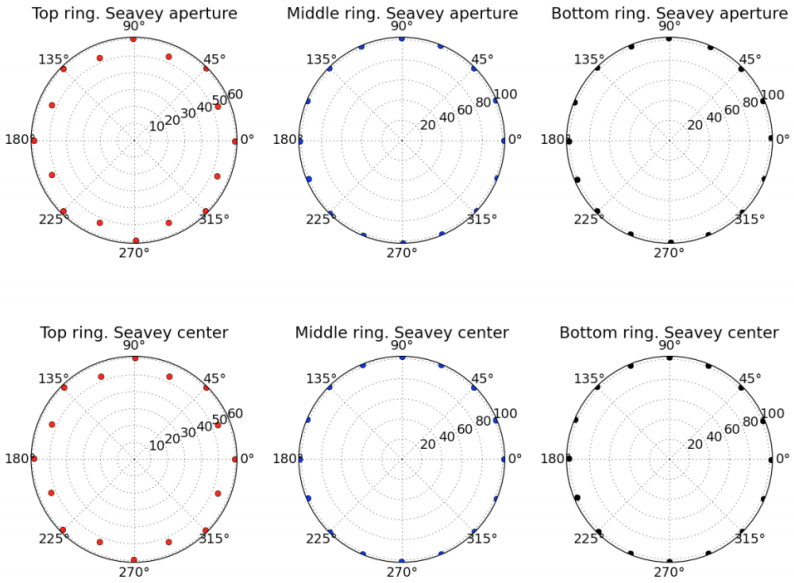

Figure 2.3: The ANITA-IV payload just before the launch near McMurdo station [18]. The major components are labeled in the graph. Photo from [18]

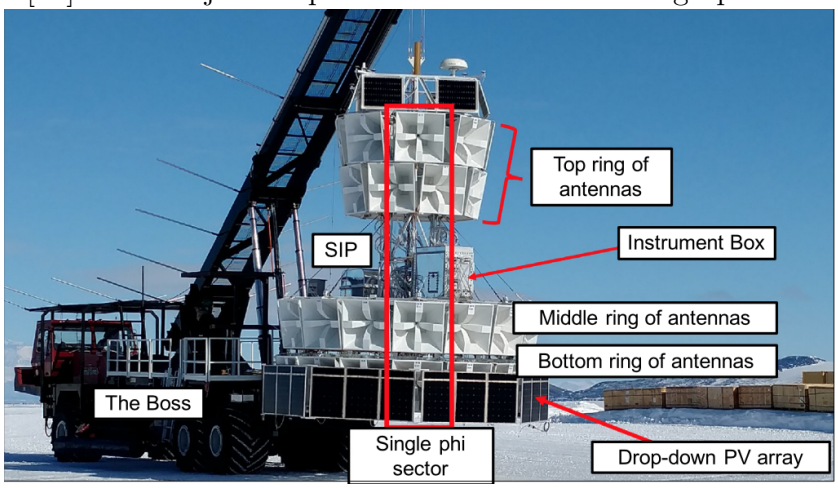

Figure 2.4: The top ring Seavey Antennas during the assembly in Palestine TX in 2016.

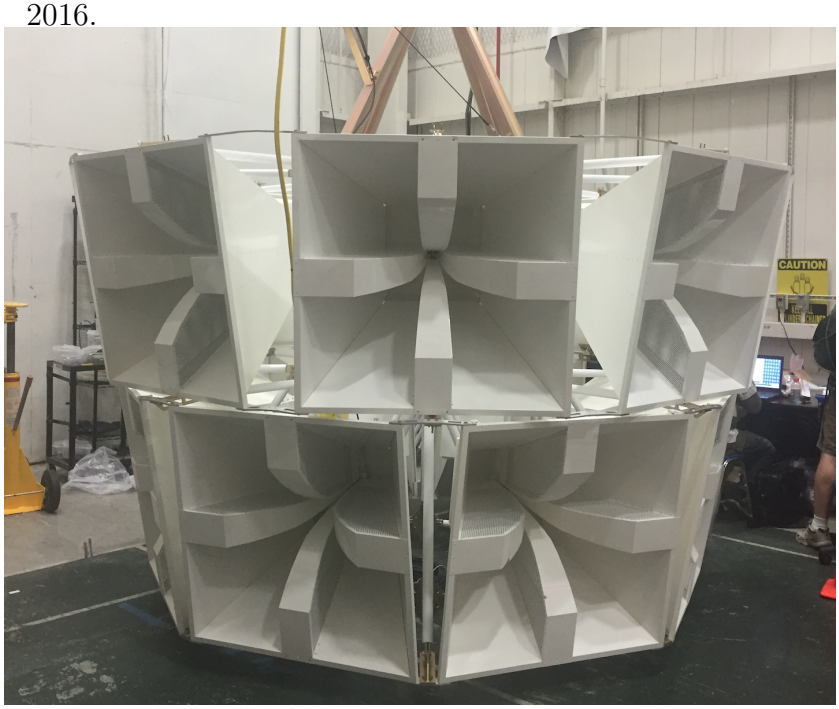

Figure 2.5: The power gain of a Seavey relative to a Seavey transmitter as a function of azimuth angle from bore-sight, representing the beam pattern of a Seavey antenna. Measured in Palestine TX in 2016.

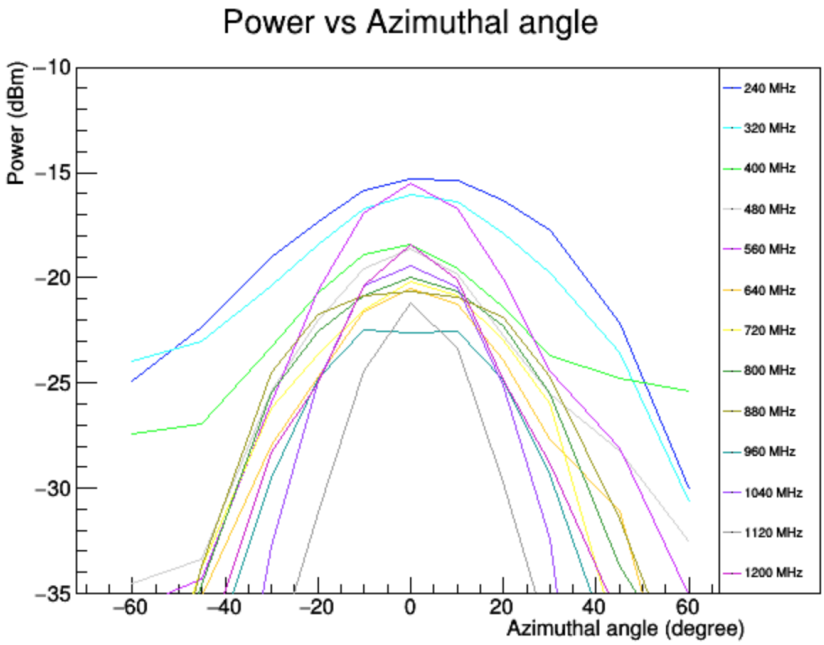

Figure 2.6: The power spectrum of the a Seavey. Different lines represent different off-bore-sight azimuth angles. Measured in Palestine 2016.

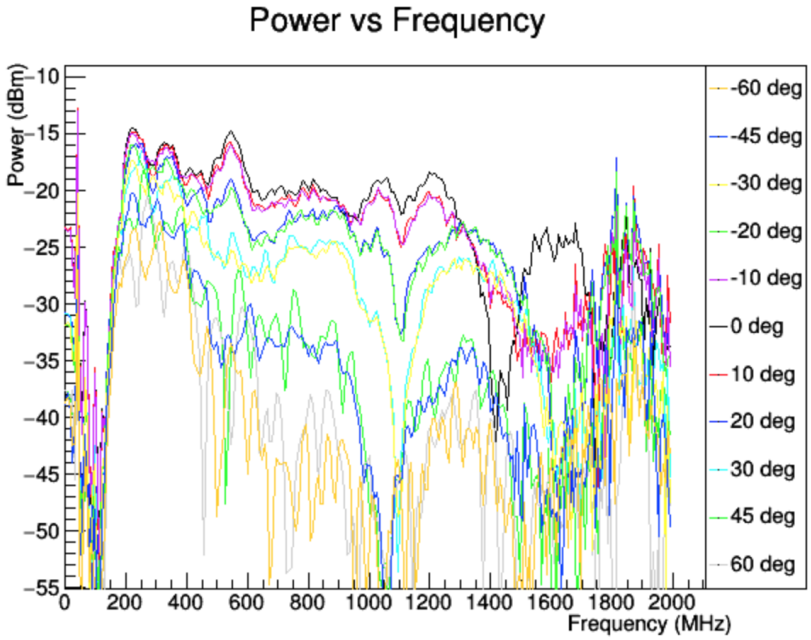

2.3 Signal Processing

Each antenna feeds for two polarizations, i.e. HPol and VPol, so we have a total of $48 \times 2 = 96$ RF channels. The RF signal processing chain is shown in Figure 2.7. The RF signal from each antenna first goes through Antenna-Mounted Pre-amplifier (AMPA), which starts with a 200 MHz–1200 MHz bandpass filter, followed by an approximately 35 dB Low Noise Amplifier (LNA) amplification. Then the RF signal goes through 12 m of an LMR240 coaxial cable to the Instrument Box. In the Instrument Box, the signal passes the Tunable Universal Filter Frontend (TUFF) boards. Then it goes through another 200 MHz-1200 MHz bandpass filters. The signal then passes through a "T" and is split into two difference sub-systems. A fraction of the signal is sent to a digitizer called the Sampling Unit for Radio Frequency (SURF) and other part of the signal is sent to a trigger system called the Trigger Unit for Radio Frequency (TURF). If an event satisfies the trigger condition, the data associated with the event is recorded and stored on flight Solid State Drives, and a small fraction of the events

Figure 2.7: The signal processing chain for ANITA-IV. From [18]

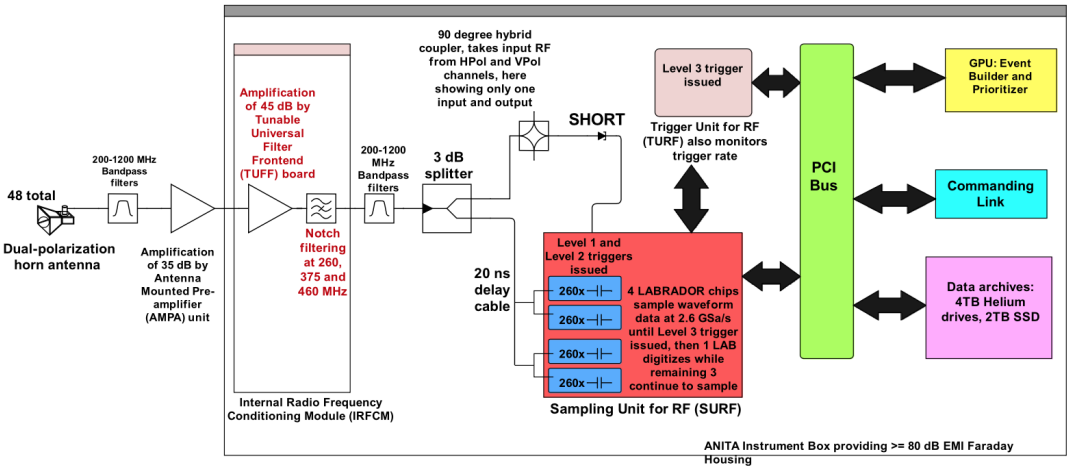

will be sent to ground.

2.3.1 Amplification

The AMPA, shown in Figure 2.8, is a custom built front-end bandpass filter (200 MHz-1200 MHz) and a 45 dB Low Noise Amplifie (LNA). Since the signal will have a secondary amplification, the bandpass filters ensure that any power outside the ANITA band is suppressed. The gain and noise spectrum for all 98 AMPA (2 spares) is shown in Figure 2.9 and Figure 2.10.

2.3.2 TUFF

During ANITA-III flight, it was realized the Continuous Waveform (CW) signals transmitted from communication satellites were continuously triggering events. This led to excessive phi-masking (over half of the antennas are masked) and low instrument livetime ratio (31.6%). More discussion about masking and livetime is in Section 2.3.5. To mitigate this narrow-band anthropogenic noise, a new sub-system, named the TUFF board, was designed for ANITA-IV as shown in Figure 2.11. There are 16 TUFF boards, and each TUFF board has 6 RF channels. The TUFF board not only provides

Figure 2.8: The Antenna-Mounted Pre-amplifier (AMPA) unit. [19]

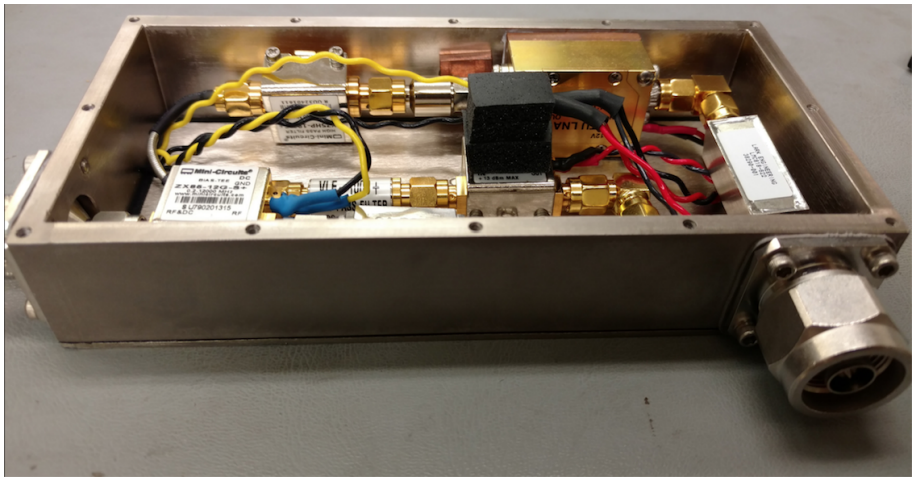

Figure 2.9: The plot Gain vs Frequency for the AMPA unit. [20]

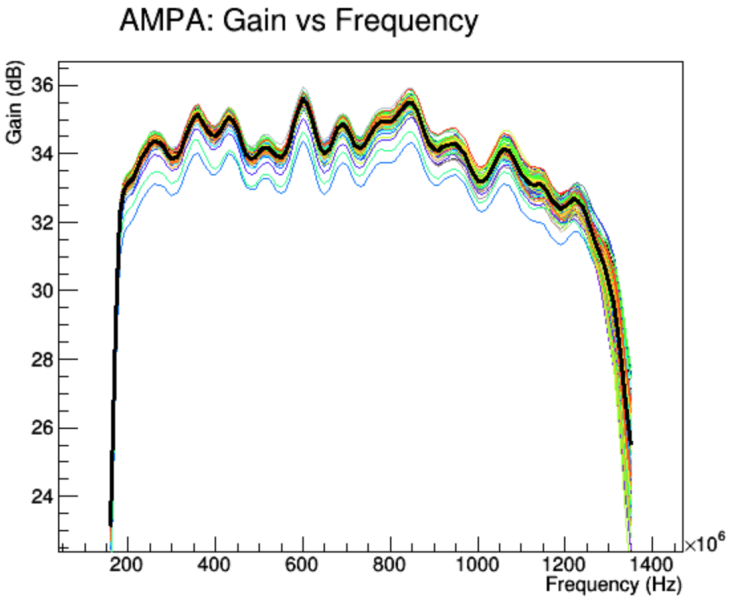

Figure 2.10: The plot of Noise Figure vs Frequency for the AMPA unit. Noise Figure is the Noise Factor in units of dB. Noise Factor is the ratio of input SNR to output SNR. [20]

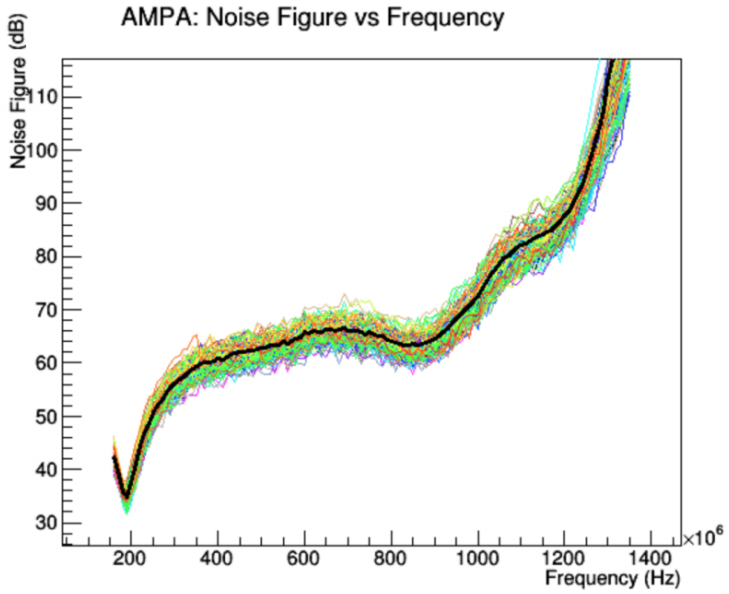

configurable notch filters for each channel, but also amplifies the signal by 45dB. In ANITA-IV, the notch reduces the CW triggers, and it contributed to a factor of 2.8 higher instrument livetime ratio (91.3%) compared to ANITA-III [18].

There are three notch filters in the TUFF board. The default frequencies are 260 MHz (notch 1), 375 MHz (notch 2) and 460 MHz (notch 3). The first two notches are designed to mitigate the CW from satellites. The third notch filter is designed to filter the CW from the McMurdo station and the South Pole. During the post flight analysis, it was determined the 460 MHz notch did not function properly with the sin-subtraction filter, which is waveform filter algorithm that removes dominate sinusoidal components in the waveform. This algorithm, developed by Cosmin Deaconu of University of Chicago, reduces the CW residual contamination in the waveforms [80]. So when notch 460 MHz is on, we turn off the sin-sub filter in data analysis. The period when notch 460 is on is shown in Figure 2.11.

Figure 2.11: A single TUFF board. The TUFF board performs an approximate 45 dB amplification, supplies power to the AMPA unit through a bias tee and provides configurable notch filters. [18]

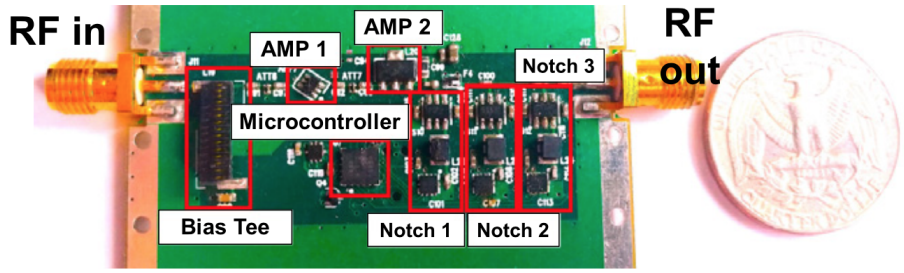

Figure 2.12: The number of triggered events per run vs run. The red line is when notch 460 is on (near the South Pole or McMurdo Station). The blue line includes all the events.

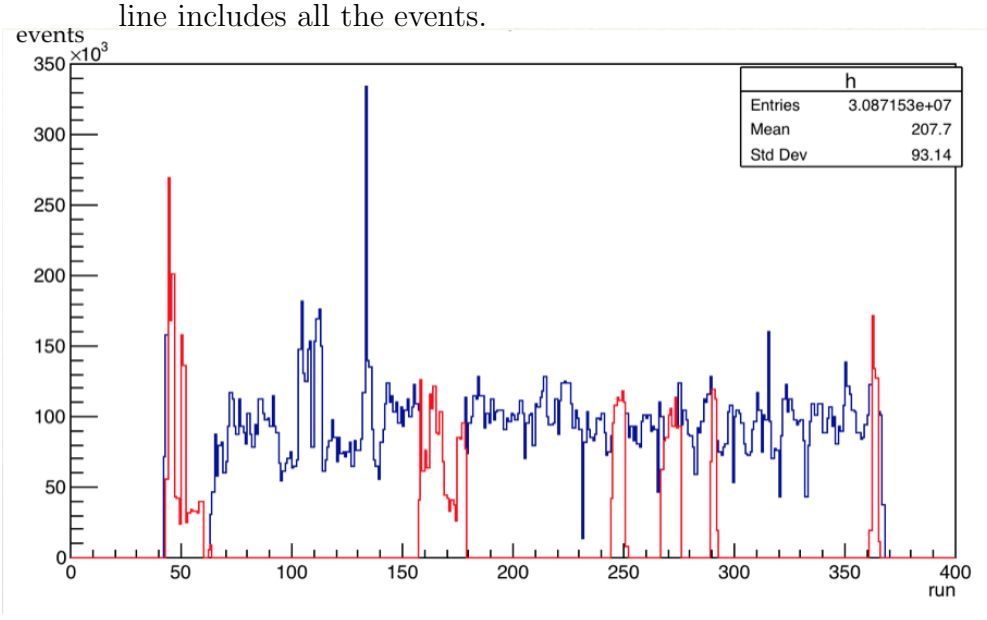

2.3.3 Trigger

Due to power and data storage limitation, the instrument uses a criteria, called a trigger, to quickly decide which events to keep that are considered interesting. In this section, the trigger system is described. The filtered and amplified HPol and VPol signals, as described in the previous section, are received by the 90° Hybrid Coupler which converts the signals to Left (LCP) and Right (RCP) Circular Polarization channels. The RCP and LCP signals are received by the SURF High Occupancy RF Trigger (SHORT), which contains a tunnel diode and an amplifier. Each SHORT can handle four channels. The output from SHORT is proportional to the square of the voltage in the recent 5ns and will be routed to the SURF trigger. The squared voltage is a measure of power, and it will be compared to a DAC threshold. If the output is larger than the threshold, it will send a signal to SURF for further trigger analysis. There are three triggers in ANITA-IV: Level 1, Level 2 and Level 3.

2.3.3.1 Level 1 trigger

The Level 1 trigger requires a single horn to meet the condition that both LCP power and RCP power pass a DAC threshold for 4ns. The CW signal from the satellite is usually left circular polarized, and our expected RF signal is linear polarized. Requiring LCP/RCP coincidence in the trigger mitigated the influence of communication satellite signals on live-time and trigger efficiency.

2.3.3.2 Level 2 trigger

The Level 2 trigger condition requires a minimum of two Level 1 triggers to occur in the same phi sector with overlapping time windows. Each Level 1 trigger opens a time window with a width that depends on the location of the antenna. The time width for an antenna located either on the top, mid and bottom rings are 4 ns, 12 ns and 16 ns respectively. The selection of these values were based on the geometry of the payload and the preferred arrival direction of an EM plane wave, which is in the inclined direction from the ice.

2.3.3.3 Level 3 trigger

The Level 3 trigger condition require two Level 2 triggers to occur on adjacent phi sectors within a 10 ns time window. If a Level 3 trigger is issued by the TURF board, then the SURF board begin to digitize and record the event as discussed in Section 2.3.4.

2.3.4 Digitization

The SURF board is also responsible for signal digitization. There are 12 SURF boards, and each SURF board has four custom build integrated circuits called LABRADOR (LAB) . Each LAB chip can handle 8 RF channels and one clock channel. For each channel, a Switched Capacitor A1rray (SCA) with 260 capacitors is used to record the voltage with 2.6 G samples/s. So at any time, the voltage snapshot in SCA is 260/2.6 G/s = 100 ns long. When Level 3 trigger occurs, this 100 ns voltage snapshot is on hold and sampled by the LAB chip. It will cause a 5-10 ms deadtime for the LAB. The four LAB chips in the same SURF board are working in a queue for the same 8 RF channels. If one LAB chip is occupied, the other LAB chips can be used. If all the LAB chips are occupied, the new triggered events will not be recorded and our instrument will undergo digitization deadtime where data cannot be recorded. This deadtime is more likely to occur when a strong CW anthropogenic source is detectable by the payload. To reduce the deadtime, the noisiest channels are masked. In ANITA-III, over half of the payload needed to be masked during most of the flight. This is the motivation of designing TUFF and LCP/RCP trigger in ANITA-IV to mitigate the CW triggers.

2.3.5 Instrument Deadtime

Instrument deadtime is the interval of time when the instrument is not available to record the event. The deadtime ratio is instrument deadtime divided by the total flight time. The livetime ratio is equal to 1 minus the deadtime ratio. Instrument deadtime is composed of two kinds of deadtime: 1) digitization deadtime 2) masking deadtime.

Digitization deadtime can occur when all the four LAB chips in the SURF board are busy recording prior events. The ability to record an event during deadtime is negated because of the limitation of ANITA's hardware .

Masking deadtime is equal to the fraction of masked phi sectors. The masking can occur when the voltage from a phi sector is constantly above the DAC threshold. Increase the DAC threshold would decrease the masking deadtime, but it will make the trigger less sensitive to signal. Masking is also a way to reduce the digitization deadtime but it does not lower the instrument deadtime.

As has been found in earlier ANITA flights, satellite CW is one of the major backgrounds during all ANITA flights. In ANITA-III, masking was the primary method to reduce satellite CW events, but it resulted in a large instrument deadtime, which leads to a lowering of our exposure to the signal. In ANITA-IV, the TUFF board and LCP + RCP trigger mitigate the chance of the CW triggering rate. As shown in Figure 2.13, the total instrument deadtime, which was 68.4% in ANITA-III, was reduced to 8.7% in ANITA-IV.

2.4 Housekeeping

There are also housekeeping sensors, such as a temperature sensor, sun sensors, accelerometers and magnetometers, installed on the payload. The temperature is used for a post-flight waveform calibration because the sampling rate in LAB chip is temperature dependent. The sun sensor, accelerometers, and magnetometers are navigation sub-systems to determine the position and altitude of payload as a back up to GPS.

2.5 GPS

The position and attitude of ANITA-IV payload are necessary for the data analysis. Three independent GPS systems are used in ANITA-IV. There are two sets of ADU5 GPS units, called ADU5A and ADU5B, and one G12 GPS unit. Each ADU5 has an array of four antennas and can independently give the longitude, latitude, altitude,

Figure 2.13: Top: the instrument deadtime in ANITA-III flight. Masking was the primary method to reduce digitization deadtime but still results in a large instrument deadtime. Bottom: the instrument deadtime in ANITA-IV flight. The use of LCP+RCP trigger and TUFF board makes payload less sensitive to satellite CW. Hence the instrument deadtime remains at a low level. [18]

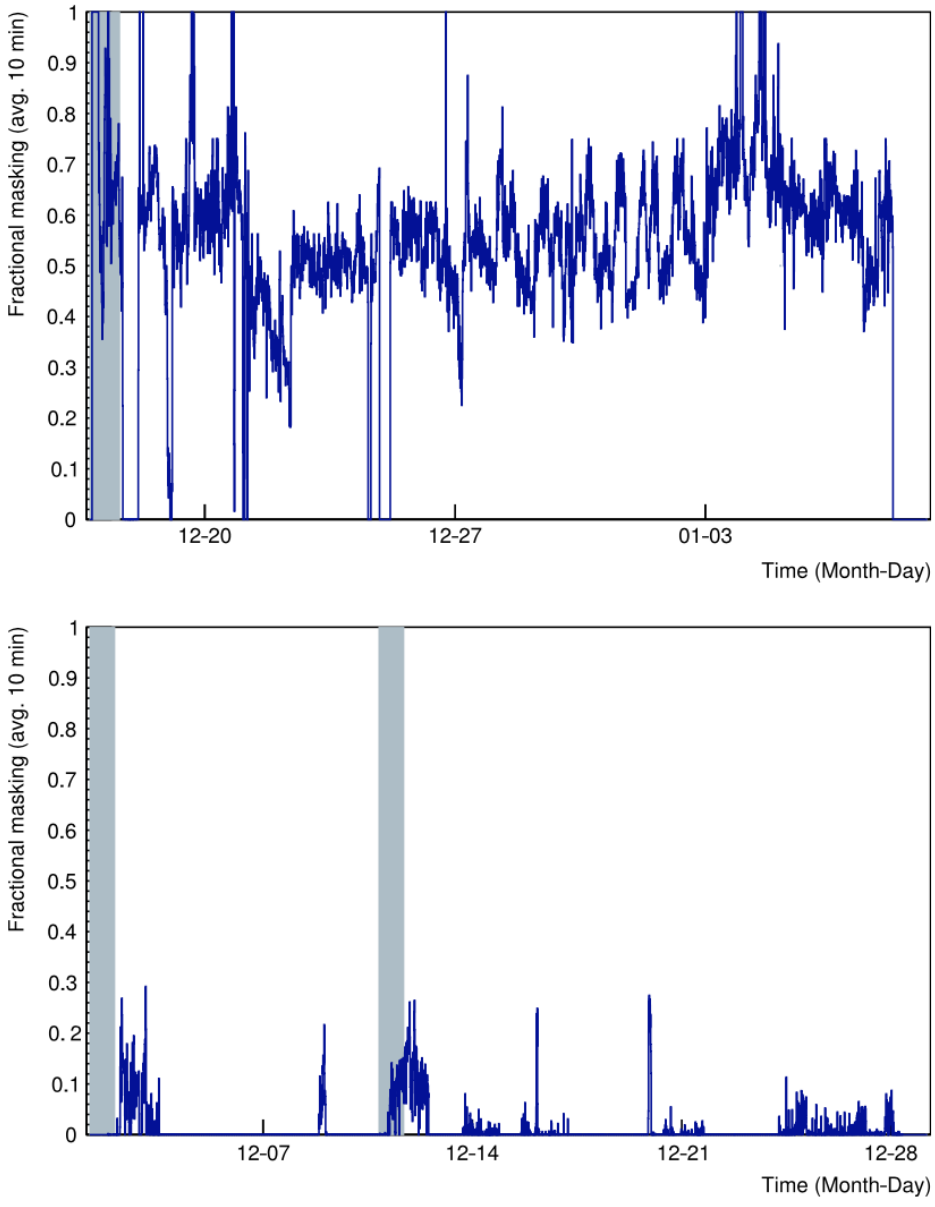

heading, pitch, and roll. The G12 GPS gives position and velocity information with a much higher rate than ADU5s.

2.6 SIP

The Columbia Scientific Balloon Facility (CSBF) provides a Support Instrument Package (SIP) for every LDB missions including ANITA. The ANITA SIP was mounted inside a Faraday cage to reduce electromagnetic interference. Three communication channels are available through the SIP which allows near real-time science data transmitted to the ground. The Line Of Sight (LOS) channel communicates directly with McMurdo station while the other two channels utilize satellite networks including Tracking and Data Relay Satellite System (TDRSS) and Iridium. The SIP also has its own GPS, temperature sensors, barometers, data storage and power system. The position of the SIP is shown in Figure 2.1 and Figure 2.3.

2.7 Event Prioritization

ANITA-IV recorded nearly 97 million events during the whole flight. However, due to the limited data rates (see Section 3.1), only 0.1% of the data can be sent to the ground through telemetry. Therefore we prefer to send more signal-like events in case of failing to recover the hard drive. An event prioritizer is designed such that an event with a smaller priority value (from 1 to 9) would be sent first. Since ANITA-III, a GPU has been incorporated in order to do a quick interferometric analysis on the fly.

The priority value is integers from 1 to 9. Priority 1-6 are the range for normal events. The events with larger map peak and Hilbert Peak tend to have a smaller priority value. (Hilbert Peak is the max voltage in CSW after a Hilbert Transformation) Priority 7 is assigned when the priority queue is too long. Priority 8 is assigned when a Strong CW event is recognized. Priority 9 represents a SURF saturation (a kind of Glitch event).

However, the prioritizer had some failure during the ANITA-IV flight. It ceased working at the end of run 59. About an hour of the flight data was lost. The prioritizer

also suffered from a severe memory leak: this is a design which will need to be fixed in the future ANITA experiments.

Chapter 3

GROUND MONITORING SYSTEM OF ANITA-IV

Two mirrored SSD hard drives named Helium-1 and Helium-2 onboard stored all the triggered events and housekeeping data, which were retrieved after the flight. However, it was still important for us to be able to view the waveform data and housekeeping information in real time during the flight. Nearly 0.1% of raw data was sent to a ground station during the flight through different communication channels (see Section 3.1). The raw data were transferred to server machines located at collaborating Universities and Institutions (Section 3.2). As described in Section 3.3, the raw data were parsed and inserted into PostgreSQL databases by the Ground Support Equipment (GSE) program. Then ANITA collaborators could view these events from a monitor website called WebANITA. I designed and developed a web-based data monitor, known as WebANITA (Section 3.5), to be the replacement of the three old ANITA GUI clients (AnitaViewer, TrigMon, and SlowMo), which had been used during the previous ANITA missions. Section 3.6 introduces another data monitor system (AWARE) developed at University College London (UCL).

3.1 Communication Channels To Ground

The SIP box supported by CSBF not only controls the balloon but also provide four channels to communicate to the ground. These channels are referred to as the Fast TDRSS, the Slow TDRSS, the Standard IRIDIUM and the LOS. The first two channels, the Fast TDRSS and the Slow TDRSS, use the TDRSS satellite network. The third one uses the IRIDIUM satellite network. In contrast to the first three channels, the fourth channel (LOS) does not rely on satellites: instead, it communicates directly with the LDB ground station when the payload is within the line-of-sight

Table 3.1: The averaged data downloading rate for different channels during the integration and testing in LDB.

Communication lines	Data Rate(kB/s)	Sender	Receiver
FAST-TDRSS	0.65	SIP	Palestine
SLOW-TDRSS	0.0089	SIP	Palestine
Standard IRIDIUM	0.014	SIP	Palestine
LOS	6.0	SIP	McMurdo Station
Openport IRIDIUM	1.16	OpenPort Antenna	Internet

range ($\sim$ 300 miles) of the McMurdo station. We had hoped to use an extra satellite channel (Openport IRIDIUM, see Figure 3.1) which used a separate array of antennas to communicate with the IRIDIUM satellites. Its bandwidth frequency is higher than IRIDIUM, and its transmission rate is larger than the standard IRIDIUM. This extra channel is supposed to support secure log-in to the instrument box on the payload during the flight. However, this channel became unstable a few hours after the launch. The reason could be the GPS unit in Openport antenna fails at high altitude so the Openport could not communicate with the satellite. Table 3.1 shows the averaged data rate during the integration the testing in LDB before the launch.

3.2 Data Flow on Ground

The data sent from the TDRSS and IRIDIUM satellites are first transferred to CSBF Palestine. Subsequently, the data are transferred to servers in McMurdo, University of Delaware (UDEL), Ohio State University (OSU) and the University of Hawaii (UH). Each of those servers runs the GSE software and maintains their own PostgreSQL databases. Each institution may have one or more dummy servers to reduce the risk of hardware failure. The data sent from LOS are transferred to the McMurdo server directly. Another path for the data is to be sent first to Washington University in St. Louis (WUSTL) and subsequently to be sent to UDEL, OSU and UH.

Figure 3.1: Openport IRIDIUM Antenna mounted on the top of the payload. The one on the top right is the Openport Antenna. Photo by John Clem.

Figure 3.2: The flow of raw data between all the servers (red boxes) in ANITA-IV. There are dummy servers in different institutions.

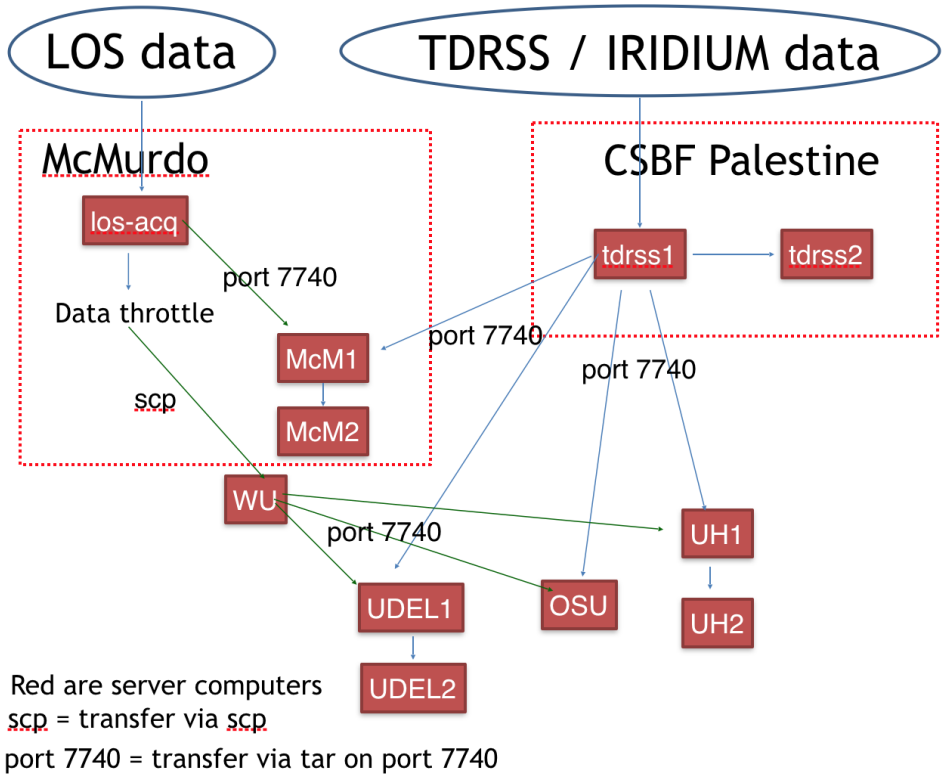

3.3 Data Flow in GSE

GSE is a set of Perl scripts and C++ library routines originally written by Predrag Miocinovic from the University of Hawaii in 2004. A computer running the CentOS operating system with GSE software and PostgreSQL database installed is called a GSE machine. In order to reduce the risk of hardware failure, each institution has its own mirror GSE servers running. University of Delaware group maintained the GSE software and database for ANITA-III and ANITA-IV. The main purposes of GSE are receiving the ANITA data stream, fanning it out as necessary, unpacking and generating PostgreSQL databases. Figure 3.3 shows how data flows in a GSE machine. When receiving payload data from TDRSS and IRIDIUM satellites, ANITA would send raw data files as the binary packets with a predefined Little Data Description Language (LDDL) format to our GSE machine on port 7740. In the GSE, several Perl scripts are continuously running as daemons (computer programs that run as background processes). For example, *receive.pl* listens on port 7740 to store the raw data and fan the data out to another GSE machines if necessary. *Process.pl* monitors the new raw data and creates new links to them. *Clearlink.pl* moves excess links to a buffer folder when new data files burst in and puts old links back to new links when no new data come in. *Linkfeed.pl* monitors the new links and feeds them into a predefined pipe, a unidirectional data channel that can be used for inter-process communication. Finally the C++ library, *unpackd.c*, parses the raw data file and inserts it into the PostgreSQL database.

3.4 PostgreSQL Database

The PostgreSQL database is an open source Linux database software, which was used to store payload flight data sent to ground by telemetry. The telemetry data was sent down as packets which are minimized in size but difficult to read and retrieve. Parsing raw data packet and inserting data into database allow direct access to realtime flight data, such as the waveform and housekeeping status of ANITA, with standardize

Figure 3.3: The data flow in GSE. The GSE daemon scripts and parse library are in red. *Receive.pl* listens on port 7740 to store the raw data. *Process.pl* monitors the new raw data and creates links to them. *Clearlink.pl* works like a buffer which moves excess links to "old" folder when too much data arrives at the same time. *Linkfeed.pl* monitors the new links and feeds them into a predefined pipe, a unidirectional data channel that can be used for inter-process communication. Finally *unpackd.c* defines the class to parse the raw data file and inserts it to the PostgreSQL database.

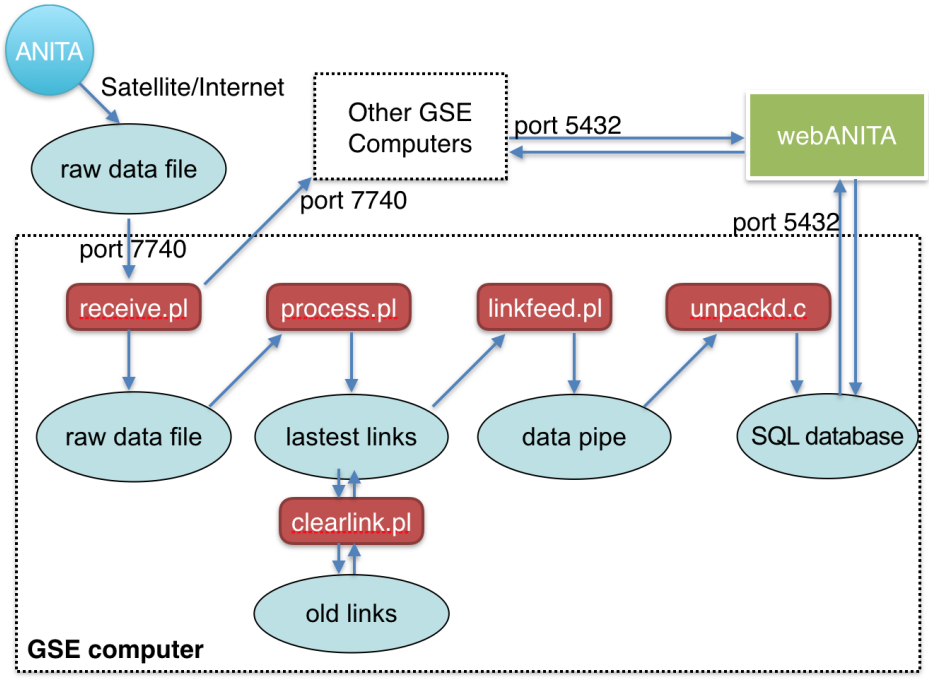

Table 3.2: The tables in a PostgreSQL database.

Table	Purpose
hk_cal	Raw housekeeping data
hk	Calibrated housekeeping data
sshk_cal	Raw sun sensor housekeeping data
sshk	Calibrated sun sensor housekeeping data
hk_surf	SURF housekeeping data
turf	TURF rates
rtlsdr	RTLSDR pow spectrum table
tuff_status	TUFF status table
mon	Disk space and queue monitor table
adu5_pat	ADU5 GPS position table
adu5_vtg	ADU5 GPS velocity table
adu5_sat	ADU5 GPS satellite info table
g12_pos	G12 GPS position and velocity table
g12_sat	G12 GPS satellite info table
cmd	Command echo table
wakeup	Wakeup packet table
file	Configuration file table
slow	Slow rate packets
hd	Header table
wv	Raw waveform table

format. Table 3.2 lists the tables in a PostgreSQL database. For the complete contents in the database, please see ANITA database layout.

However, after the raw data are parsed and inserted into the database, the size of the space used would be increased by a factor of ten. The size of a database can easily reach several GBs in a few hours. When the database gets too large, the process of querying the database becomes slow. To avoid this, the database will be automatically rotated every six hours, i.e., the current database is closed and a new database is created (and becomes the current one) every 6 hours. The naming of the database is defined as $anita\_mmddx$, where mm is the month, dd is the day, and x is the number of databases in this day (four databases per day, labeled in order of increasing time as a, b, c and d). This automation routine is also a part of the GSE software.

Figure 3.4: The ANITA Viewer page of webANITA. It shows the basic header information and the waveforms in 108 channels. Clicking on the waveform will open a zoomed-in waveform.

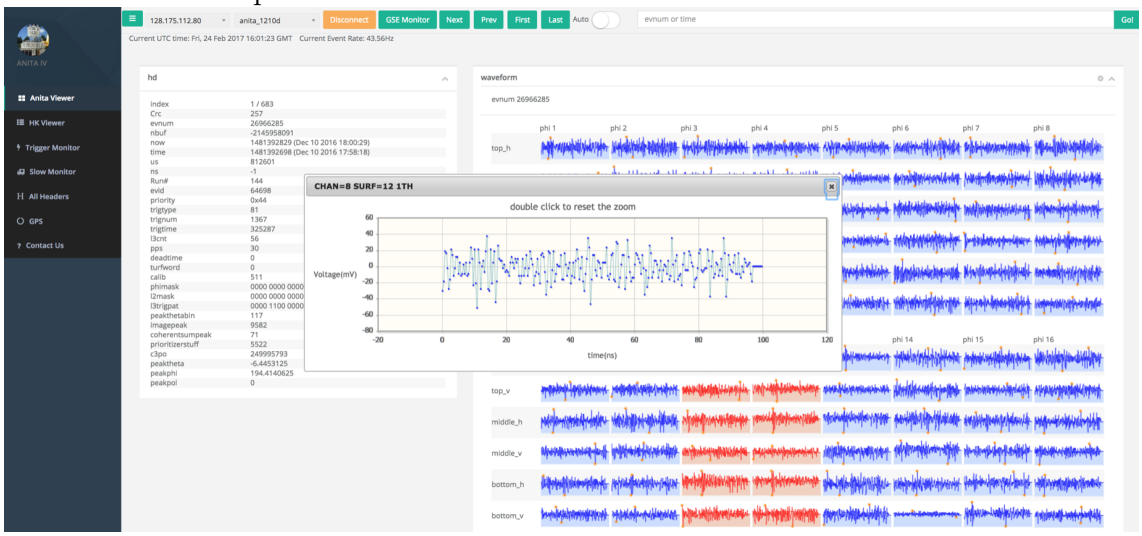

3.5 WebANITA

This section focus on the features of WebANITA, which we designed from scratch in the University of Delaware. The source code of WebANITA is in WebANITA GitHub. Please follow the Readme file for installation.

WebANITA is a website which is designed to monitor the real-time waveform and housekeeping data that the payload sends to the ground. It makes a connection to the PostgreSQL databases and displays waveforms and charts to the user. The principal reason for designing this website was to replace the old C++ GUI software: ANITA Viewer, TriggMon Viewer, and Slower Viewer. That old GUI software depends on the WxWidget library and on an old CentOS environment: these became difficult to maintain and upgrade after their initial development over the course of more than 14 years. The old software is also difficult to use across different OS platforms.

WebANITA benefits from the Python Flask framework as backend technology and Bootstrap and HTML5 as frontend technology. It is an improvement for both developer and user. For the developer, 1) the amount of code is significantly reduced; 2) the structure of the code is better designed and is clear because Flask has defined

Figure 3.5: The HK Viewer page of webANITA. It shows many important housekeeping information on the payload, such as voltage, current, temperature, sun sensors, disk space and GPS information. Clicking on each item will open a value vs time plot.

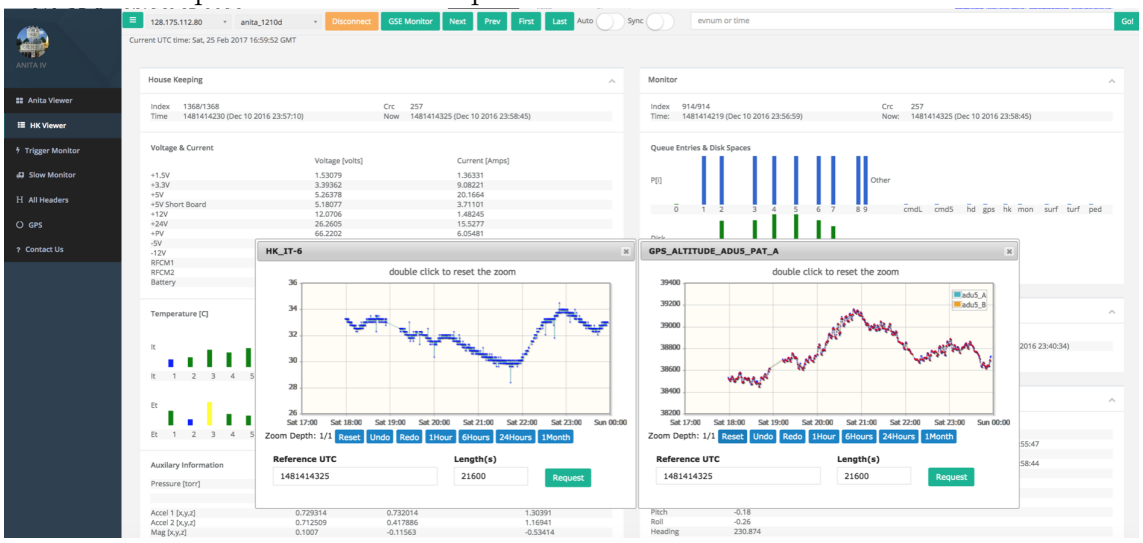

a good structure and modulized many functions: as a result, it is easier to maintain and add new features; 3) using Bootstrap and HTML5 brings more freedom to the GUI design. The chart plotting can use many existing JQuery tools, and we do not need to re-invent them; 4) It is easier to display data across several databases. The user experience is improved in many respects. 1) the website can be opened in Linux, Windows, and MacOS; 2) the GUI is more user-friendly and looks nicer. Views of WebANITA are shown in the Figure 3.4 and 3.5. 3) The website is hosted on the cloud (Heroku), which is more robust and has more freedom to scale up.

SQLAlchemy is a python lib used in the Flask framework. It can connect to a database and creates an object with a one-to-one mapping to the table in the database. It avoids the need of writing the query and parsing the results. Manipulating objects in Python has become more straight-forward.

Figure 3.6: The data flow from payload to WebANITA and AWARE. The data sent from the payload is called raw data, which are binary format packets. The raw packet's data need to be unpacked and then used for two tasks: 1) to fill the PostgreSQL database and 2) to be translated into ROOT data format[21]. WebANITA connects to the PostgreSQL database directly, and it is a real-time monitor. AWARE use JSON format data. This process needs conversion from raw packets to ROOT format, and then from ROOT to JSON format, which usually takes a few hours.

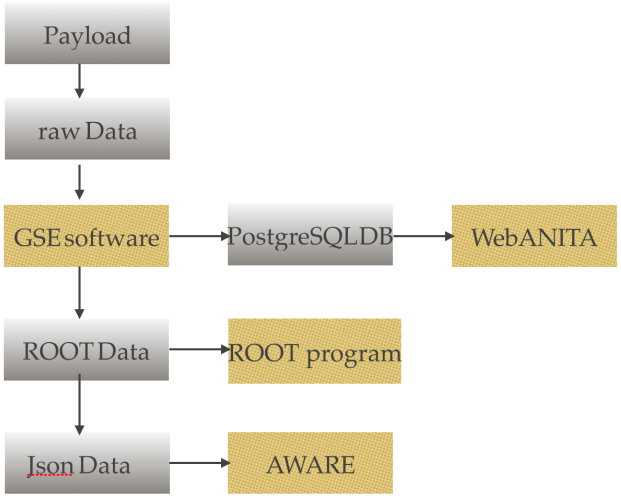

Figure 3.7: The waveform page of AWARE.

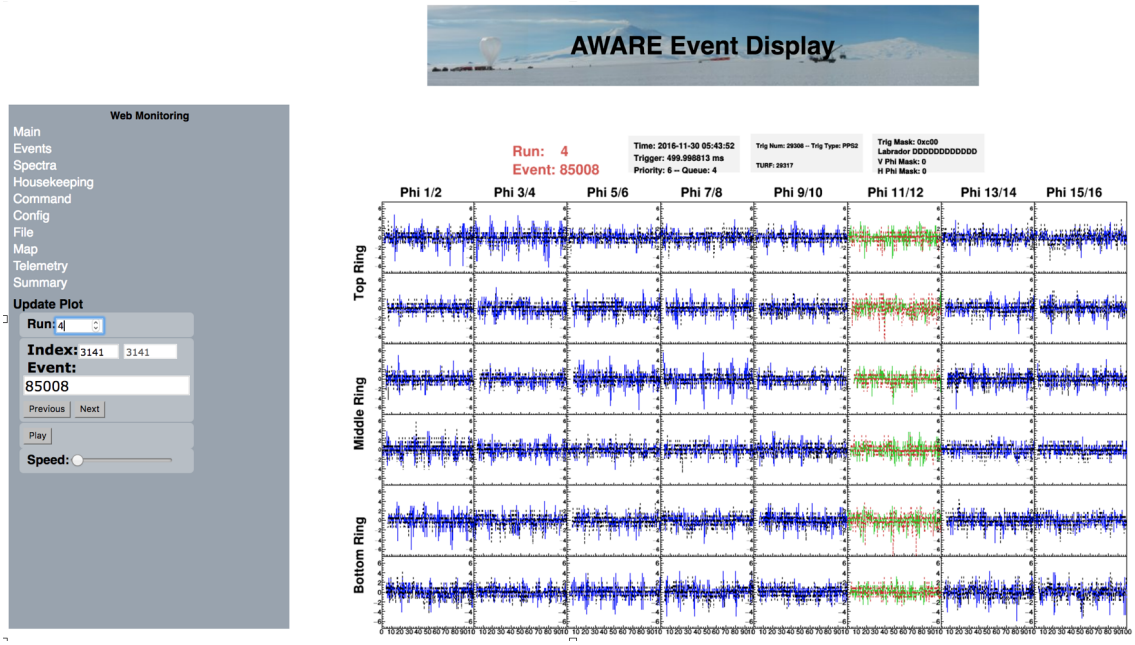

3.6 AWARE

AWARE is a website, written by Ryan Nichol at UCL, which can also be used for monitor the data. It reads data from a JSON format file as in Figure 3.6. The JSON files are also converted in UCL servers. AWARE has some features which are similar to those in WebANITA, but AWARE is designed to focus on different aspects of the data analysis. A view of the event display of AWARE is shown in Figure 3.7.a

Chapter 4

THE ANITA-IV FLIGHT

The ANITA-IV instrument was launched in December 2016 and flew around the Antarctica landmass for approximately 28 days (see Section 4.1). The flight began at McMurdo where anthropogenic background saturated the trigger. In the next four days, the payload flew through the East Antarctica which has very deep ice and few anthropogenic stations (perfect for a neutrino search). In the next six days, it continued to fly around West Antarctica where the ice depths are somewhat shallower with a greater population of anthropogenic sources, including ANITA calibration ground stations that are critical to the mission. During the following five days, ANITA-IV flew through East Antarctica again in a similar path as the first four days. The following eight days the payload slowed down in West Antarctica and drifted toward the South Pole. The last five days of flight were spent near South Pole station and landed near by.

During the flight, the payload was exposed to different calibration pulser sources. A ground base calibration pulser was operated from the West Antarctic Ice Sheet divide (WAIS station) while two small balloon-based payloads HiCal-2a and HiCal-2b provided a high altitude pulser source. See more discussion in Sections 4.2 and 4.3.

4.1 ANITA-IV flight summary

ANITA-IV payload was launched at 8:00 am December 2nd, 2016 (UTC) and after 27 days and 21 hours, it was terminated at 5:00 am December 30th, 2016. The launch took place from Willy Airfield near McMurdo station (Figure 4.1). The payload landed at $88.22516^{\circ}S, 98.88420^{\circ}E$ at 6:04 am December 30th, 2016. Figure 4.2 shows how the payload landed in Antarctica.

Figure 4.1: ANITA-IV was launched from Antarctica's Ross Ice Shelf near McMurdo Station. Photo credit: NASA.

Figure 4.2: After the flight mission, ANITA-IV landed at $88.22516°S, 98.88420°E$. The instrument was recovered on November 2017. Photo credit: Christian Miki.

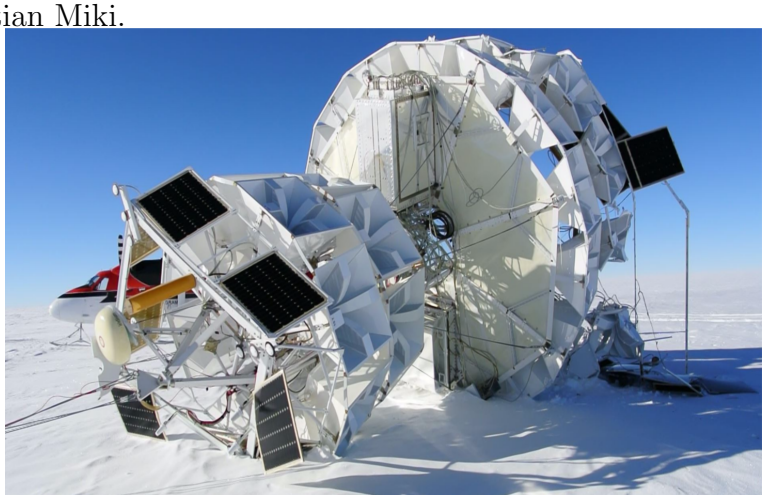

During the whole flight, the averaged event trigger rate was 41Hz. The event rate as a function to time is shown in Figure 4.3. While only 0.1% of the triggered events and telemetry data were sent to ground through the IRIDIUM and TDRSS satellites, all of the raw data up to 3 TB were stored on the payload SSD hard drives (Helium 1 and Helium 2): these hard drives were recovered after the landing. During the flight, we obtained a total of 366 runs of data, from run 2 to run 367. Each run contains two hours' flight data. Since the data during the launch time suffered from extreme anthropogenic noise, the data analysis to be presented here only selects data from run 41 to run 367. Run 41 refers to the time when ANITA-IV had reached a stable altitude.

For unknown reasons, perhaps due to some kind of deadlock, the prioritizer did not end gracefully at the end of Run 59, instead, it was in a hung state. In the following one hour, no event data were written into the disk or telemetry until prioritizer was killed by command as shown in Figure 4.3, where the event rate dropped to zero at run 59.

The ANITA-IV flight path is shown in 4.4. During the flight, it passed close to two pulser stations, the WAIS station, and the LDB station: both stations were used for purposes of calibration. The LDB pulser is at the McMurdo station where there are additional background noises. The WAIS pulser was the best calibration signal to which we had access during the ANITA-IV flight.

4.2 ANITA-IV WAIS pulser station

In the first round of the ANITA-IV flight path around the South Pole, the payload passed very close to the WAIS pulser station. The closest distance to WAIS was about 68km. The period of WAIS signal detectability started during run 122 and ended at run 154. We recorded a total of 215135 WAIS events.

A tripod mounted Seavey antenna located near the WAIS station transmitted both VPol and HPol pulses toward the ANITA payload when in range (see Figure 4.5). VPol and HPol feeds were connected to independent pulsers synchronize to a GPS time,

Figure 4.3: The averaged event rate (in units of Hz) for the time period during the flight which we analyzed (from run 41 to run 367). Each run is a two hours period.

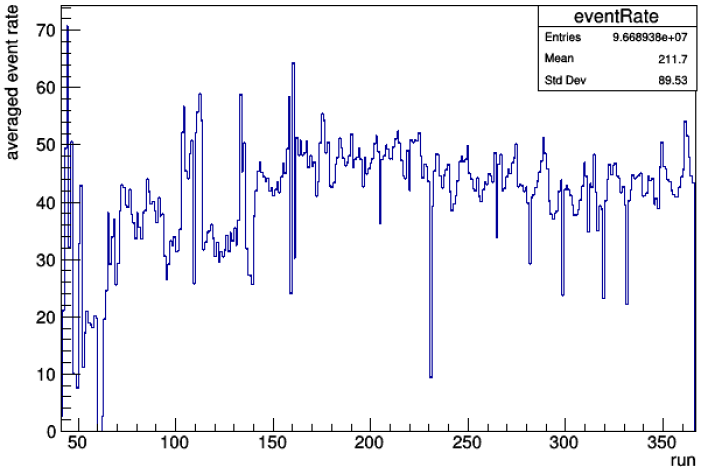

Figure 4.4: ANITA-IV flight path. Start from the red line. The triangles are WAIS, Siple Dome and LDB site from left to right. From AWARE by Ryan Nichol [22].

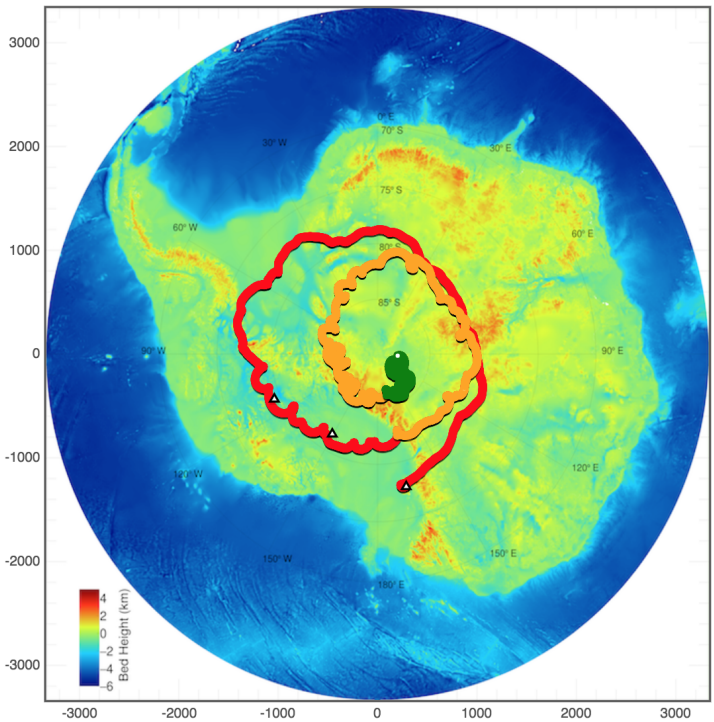

however the VPol pulser was delayed 10 ms as a means to distinguish Vpol and HPol pulsers by arrival time differences. The arrival time at the payload can be calculated using the pulser GPS time and time of flight for light to propagate from the pulser to the payload location. The time difference between the GPS time of the transmitted pulse and the payload trigger time is directly related to the distance between the payload and WAIS pulser pulser. From Figure 4.6 we can see that the expected trigger time plotted as a red line during the flight. Because the WAIS transmitter Seavey antenna sends the signal at a fixed time in a second, the trigger time in a second is directly related to the distance from WAIS to the payload. Above the red line, the blank area is due to the deadtime of SURF, which was discussed in Section 2.3.4. As we can see in Figure 4.7, if we subtract the time of flight from the triggerTimeNs, we can see that the HPol and VPol pulsers are separated by $10\mu s$.

When the payload was within range, the amplification and direction of the WAIS transmitter was adjusted every hour in order to maintain quality pulses. During the period when Runs 129-132 were recorded the transmitter was rotated by 45 deg about it's central axis, resulting in mixed polarization pulses at the payload, which events are known as the 45° WAIS data.

4.3 High-Altitude Calibration (HiCal)-2

HiCal-2 are companion balloon-based pulsers that flew with ANITA-IV [24]. They use high voltage discharge pulsers to transmit RF impulsive signals. The signals are HPol dominated (HPol power: VPol power $\approx 10:1$) to mimic the cosmic ray EAS radiation. Each pulse can transmit directly to the ANITA payload or reflect off the ice. The direct and the reflected events from HiCal-2 will help us understand how the roughness of the Antarctic ice affects our signal reflection. The HiCal-2 pressure vessel and electronics are shown in Figure 4.8.

There were two HiCal-2 flights named HiCal-2a and HiCal-2b. Ten days after the ANITA-IV launch, the ANITA payload circled back close to the LDB station and we got a chance to launch the HiCal-2 payload. HiCal-2b was launched from LDB

Figure 4.5: A tripod-mounted Seavey antenna at WAIS was used to send VPol and HPol pulses to ANITA payload [23].

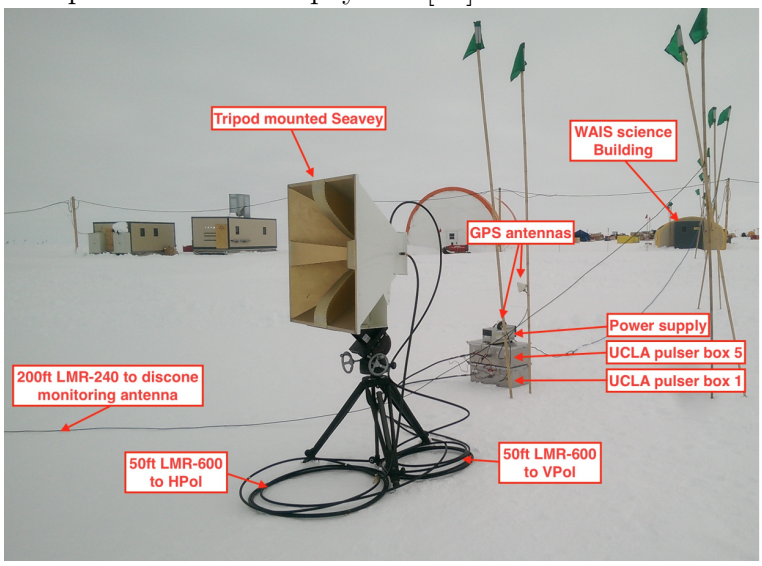

Figure 4.6: The triggerTimeNs versus realTime for all RF events between run 120 and run 160. The red line is the theoretical trigger time derived from the distance from WAIS. As we can see, it is quite consistent with the measured WAIS events. [23].

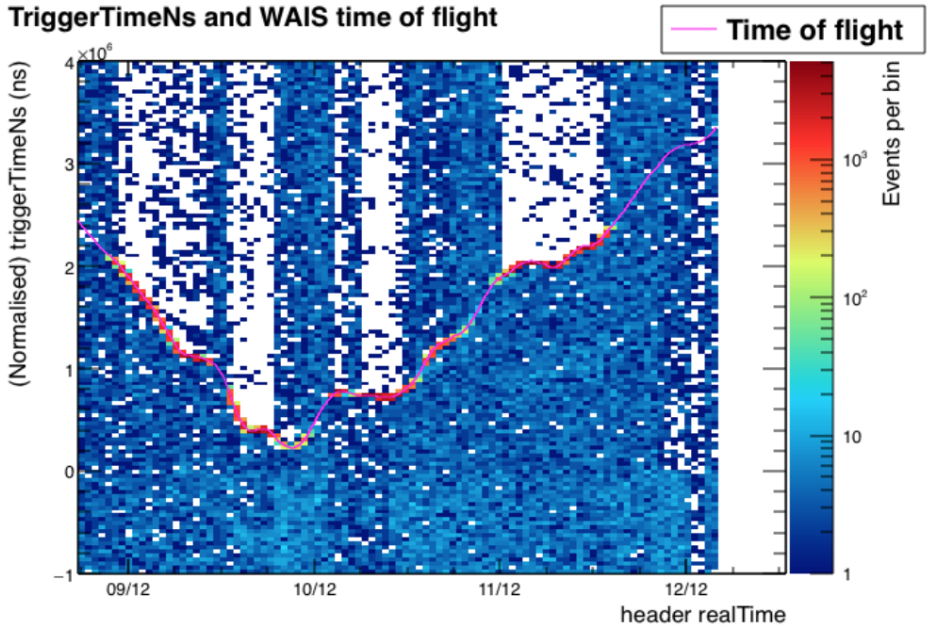

Figure 4.7: The triggerTimeNs-timeOfFlight versus realTime for all RF events between run 120 and run 160. [23].

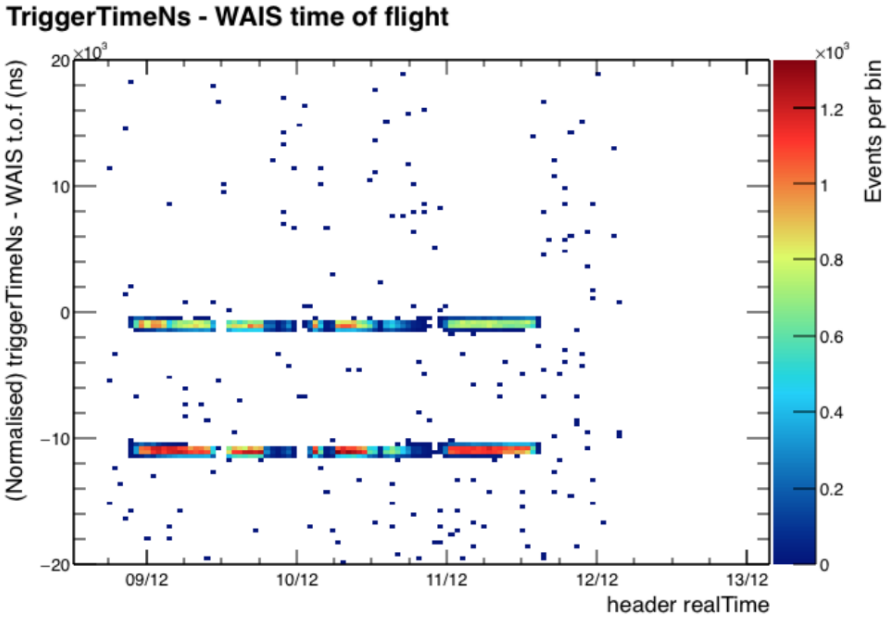

station on Dec 11, 2016. HiCal-2a was launched on Dec 12, 2016. Figure 4.9 shows the paths of the HiCal-2's flight. ANITA-IV recorded over 112642 Hical-2a events and 69082 Hical-2b events, including both direct and reflected events. The closest distance from HiCal-2 to ANITA was about 100 km, and the farthest distance was approximately 800km because of the Earth's curvature.

The polarity analysis of HiCal-2 is still on-going. Preliminary results show that the HiCal-2 event's coherently summed waveform has too much "ringing" after the impulse. This issue may be related to phase center correction or system response. In the current polarity analysis, 5% of the direct-reflected event pairs are contrary to our expectation [81]. However, evidence from HiCal-1 in ANITA-III indicated nothing abnormal about the polarity. Hence HiCal-2 needs further investigation.

The HiCal-2 events need to be completely removed from the event dataset because they will contaminate our signal region, especially in the cosmic ray search. A 6σ azimuth cut, $notHiCal$, can reduce the expected HiCal-2 events to 3.5×10^{-4}) events

Figure 4.8: The HiCal-2 pulser hangtest Palestine 2016 [24]. The top box contains the NASA electronics, GPS and system boards. The lower pipe contains the HV discharge system, antenna and pressure vessel.

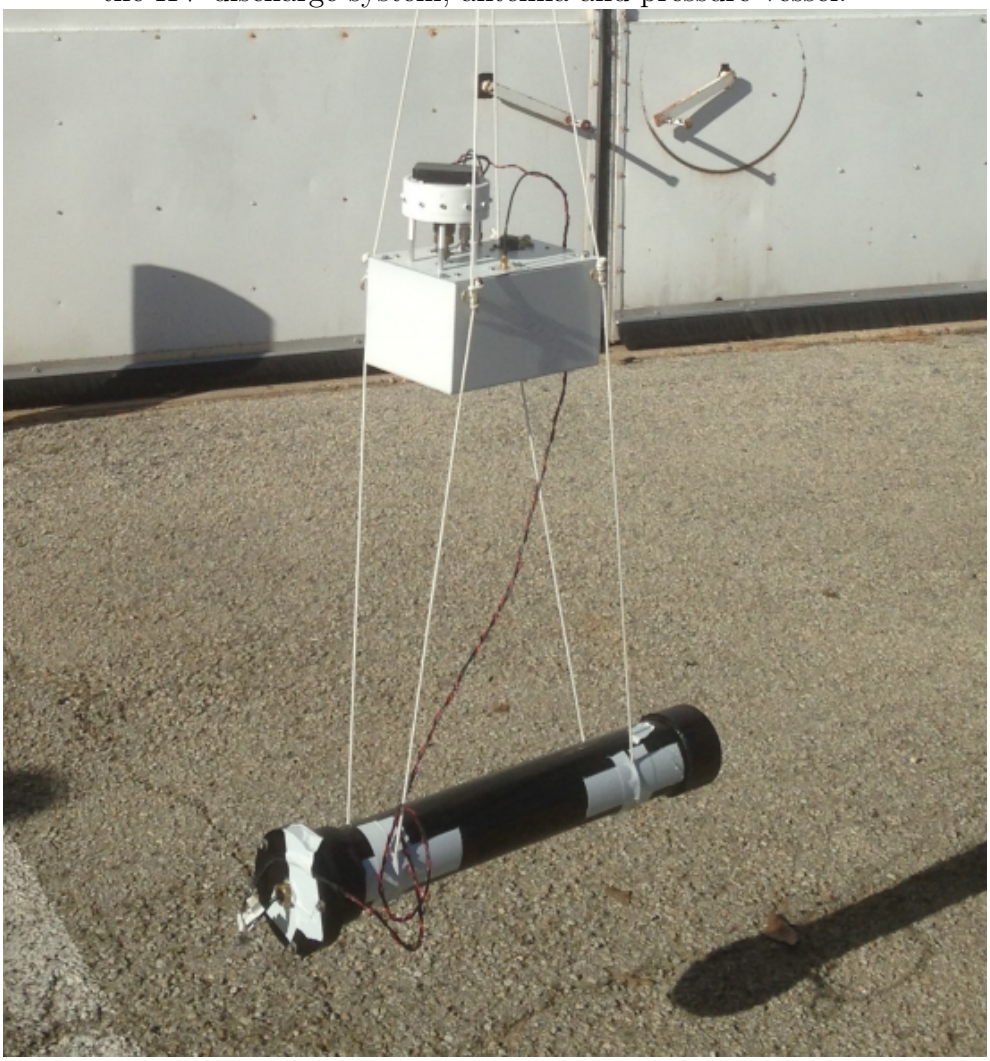

Figure 4.9: The two HiCal-2 flight path in Antarctica. [24]

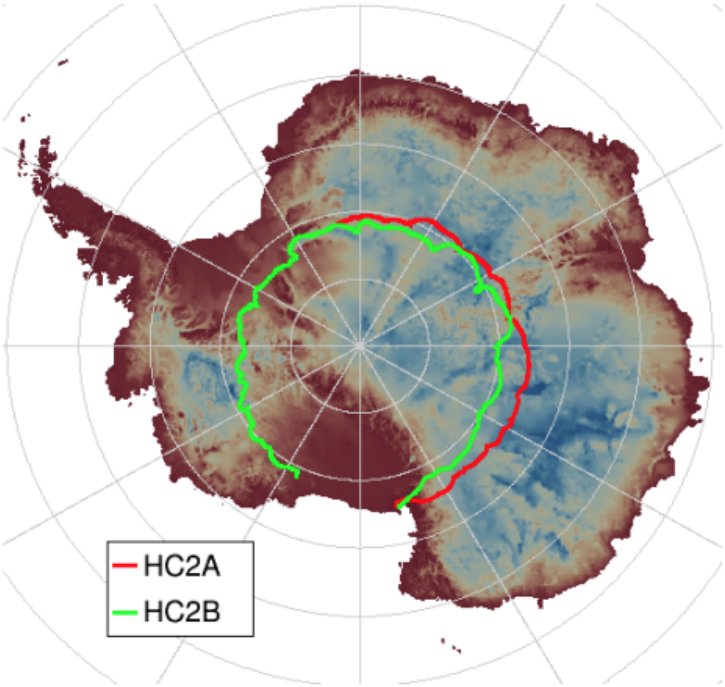

during the flight, where σ is a function of SNR as described in Section 6.5.1. More details about the $notHical$ cut will be given in Section 6.2.

Chapter 5

EVENT RECONSTRUCTION AND CALIBRATION

The purpose of event reconstruction is to extract many useful features (Section 5.1) from the raw event data and store them in the summary file, including the possible incoming direction of the RF signals from the reconstruction peaks in the interferometric map. Building the interferometric map in Section 5.2 is the critical step in event reconstruction and it needs precise antenna phase center positions, which can be estimated using the measurements in Section 2.1. Due to manufacturing errors and installation errors, the antenna phase centers still need to be calibrated in sophisticated ways. In Section 5.3, we describe how the phase center is calibrated by photogrammetric methods. In Section 5.4, we describe how the phase center is calibrated by means of the WAIS calibration pulser.

5.1 Event Reconstruction

The reconstruction of all the 97 million recorded events is performed using hundreds of CPU cores at the Asterix Cluster in the University of Delaware. After the events' reconstruction, we extract the useful information from the event and store it as an instance of AnitaEventSummary Class in a ROOT format. The reason that we need to perform event reconstruction is as follows. 1) the 3 TB raw data uses too much disk space. 2) reconstruction for millions of events is a time-expensive process. We reconstruct the raw data once for all and this can speed up the analysis process significantly. The output data are stored in the summary file, which contains basic event information such as event number, trigger time, payload attitude, etc. There is also direction information for some pointing sources such as the Sun, the WAIS station and the LDB station. Some quality cut flags such as BLAST cut and glitch cut are

stored in the flags. Moreover, we make the interferometric maps (described in Section 5.2) separately for filtered (or unfiltered) events and deconvolved (or coherent) events. In the interferometric map, we can search for the peak in each polarization. There are up to five peaks and two polarizations stored as a 2×5 array. The peak in θ and ϕ represents the possible incoming direction of the plane wave. Each antenna within 45° of the peak direction, usually 15 antennas, should have similar waveforms assuming a plane wave. Those 15 antennas' waveforms are summed together with a corresponding time delay at the peak direction, known as the coherently (or deconvolved) summed waveform, in order to achieve a better Signal to Noise Ratio (SNR): the summing of waveforms leads to a reduction in the background noise because of the cancellation of random signals. Depending on whether the waveform is deconvolved or not, we obtain the deconvolved summed waveform (DSW) or the coherently summed waveform (CSW). Neither the interferometric maps nor CSW nor DSW are stored in the summary file due to disk space limitation. Instead, we store features such as SNR, bandwidth, map peak value, Hilbert Peak, Stokes parameters, polarization, power, impulsivity measure, etc.

5.2 Interferometric Map

As mentioned in Section 2.1, the ANITA-IV payload has 48 Seaveys and 96 channels to receive RF signals continuously. When an RF event triggers the payload, each channel will record a 100 ns waveform from the digitizer. The next step is to combine the information from all channels and search for the direction of the impulsive signal. Since we use the interference pattern between different channels to generate an interferometric map, the method is called the interferometric method. The interferometric map is in payload coordinates with axes θ and ϕ. The peak on the map represents the direction of the plane wave. This process of finding the incoming direction θ and ϕ of the signal using the interferometric method is called event reconstruction.

At the first step, the 16 Seavey antennas face 16 azimuth distinct directions. As we can see in Figure 2.5, the antenna has a beam pattern which varies with the

azimuth angle, and its power drops quickly when the plane wave's incident direction differs from the bore-sight by more than 45°. For each event, all 48 antennas are used to build the interferometric map. However, for each possible direction (θ and ϕ) only the five nearest ϕ sectors should be used. Each phi sector has three antennas (top, mid and bottom), so fifteen antennas can contribute to a direction in the interferometric map. Each pair of antennas has cross-correlation value which depends on the time delay between them. For 15 antennas, there are a total of $15 \times 14/2 = 105$ independent pairs. Since we only use the pairs that are less than or equal to two phi sectors apart, the number of pairs used in the reconstruction is 78 in total.

In the second step, for each pair of antennas, we calculate the cross-correlation function between them. In order to speed up this process, the waveform is evenly sampled and then transformed into the frequency domain using (Fast Fourier Transformation) FFT. The correlation function is the convolution between the two waveforms when a number of time delays are introduced between them. The convolution h of two function f and g is defined as follow:

$$h(z) = \int f(x)g(z-x)\,\mathrm{d}x.$$

Moreover, the convolution is equivalent to multiplication in the frequency domain. So we can calculate the cross-correlation quickly in the frequency domain: this speeds up the time complexity of the calculation from $O(n^2)$ to $O(nlog(n))$.

The third step is to fill the interferometric map. The interferometric map is a 2D histogram with the elevation angle θ and azimuth angle ϕ as the axes. For a pair of antennas, given the exact position of the phase centers, for any direction (θ, ϕ) in the interferometric map, we can easily calculate the expected relative time delay ΔT_{ij} between this pair of antennas using the geometry function:

$$\Delta T_{ij} = \sin\theta(z_i - z_j) - \cos\theta\cos(\phi - \phi_i)r_i + \cos\theta\cos(\phi - \phi_j)r_j \tag{5.1}$$

Since we have already calculated the correlation function between a pair of antennas' waveforms, when we insert the value of ΔT_{ij}, we will be able to determine

Figure 5.1: The interferometric map (or interference pattern) between selected antennas for WAIS event 23407064 VPol. The top 3 graphs are the interference pattern between various pairs of antennas. The bottom left is the interference pattern using 3 antennas. The middle panel in the bottom row is the interference pattern using 5 antennas. The bottom right is the interference pattern using all 48 antennas.

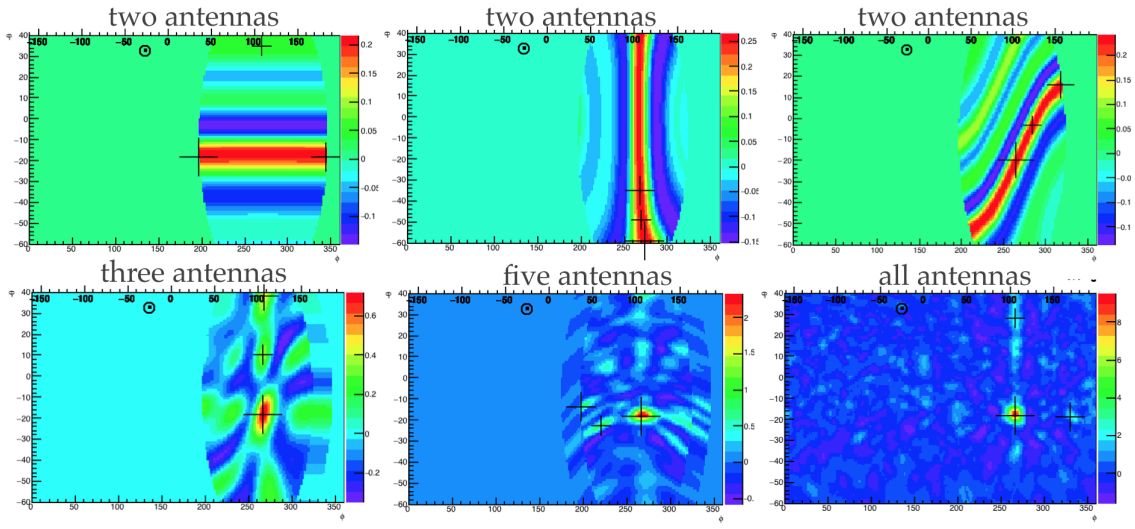

the correlation value. This correlation value for the current pair of waveforms can then be plotted at the corresponding coordinates (θ, ϕ) in the interferometric map. We can fill up the interferometric map for a pair of antennas by repeating this process. For other pairs of antennas, we just added their correlation value to the existing interferometric map. After we combined all the pairs of antennas, we get the whole interferometric map. If the triggered event is a plane wave, one peak direction will have a very large correlation value because each pair of the antennas have a large correlation value in the incoming direction and they add together. Figure 5.1 is an example that illustrates how the interferometric map of an impulsive RF source can be built up by adding additional antennas.

5.3 Antenna Photogrammetry Position

An initial estimation of the antenna phase center positions is obtained by analyzing photographs of the payload. A series of ANITA-IV photographs were taken

Figure 5.2: Left:Payload photograph during hang-test in Antarctica. The Seavey corners are marked for create the 3D model. Right: the 3D model in PhotoModeler Scanner software.

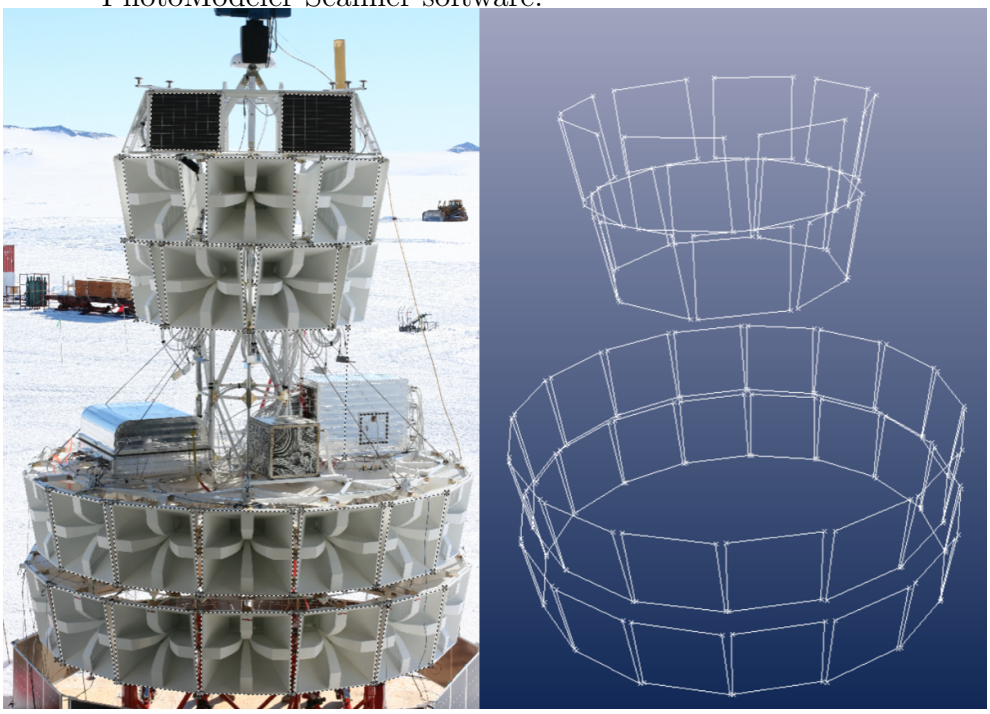

during the payload rollout at LDB on November 26, 2016. By marking the corners of each antenna, the ANITA-IV photogrammetry model was created[82] by analyzing the corner information using a PhotoModeler Scanner software. Figure 5.2 left shows one of the photos taken in Antarctica. The right shows the 3D model built from the photos. The 3D model records the positions of the four corners of each horn. Then an aperture plane, which is the face of an antenna, is fitted to the four points so that we know the normal direction of each horn. The center position of the aperture plane is calculated to fit a circle to the four points. The phase center positions are estimated to lie 20 cm behind the center positions of the aperture plane and in the opposite direction of the normal. The deviations between the mean values and the photogrammetry measurements of relative radius and Z are shown in Figure 5.3 and Figure 5.4. The top ring is separated into two rings. Figure 5.5 shows the deviations in azimuth relative to the phi sector number multiplied by 22.5°.

Figure 5.3: Antennas' photogrammetry radius vs phi sector. Each plot is relative to the sub-ring mean radius.

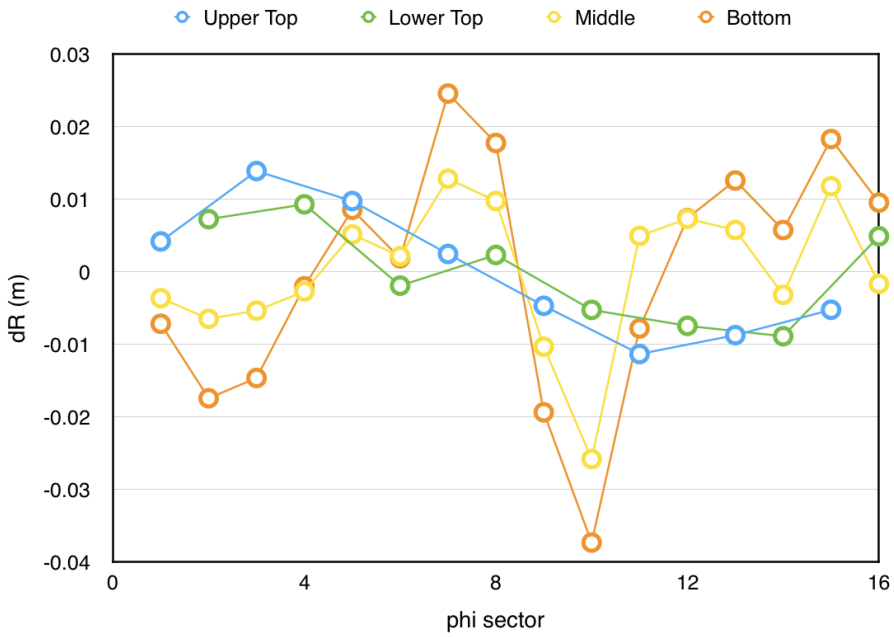

Figure 5.4: Antennas' photogrammetry Z vs phi sector. Each plot is relative to the sub-ring mean Z value.

Figure 5.5: Antennas' photogrammetry azimuth vs phi sector. The azimuth is relative to the expected the azimuth phi sector * 22.5°.

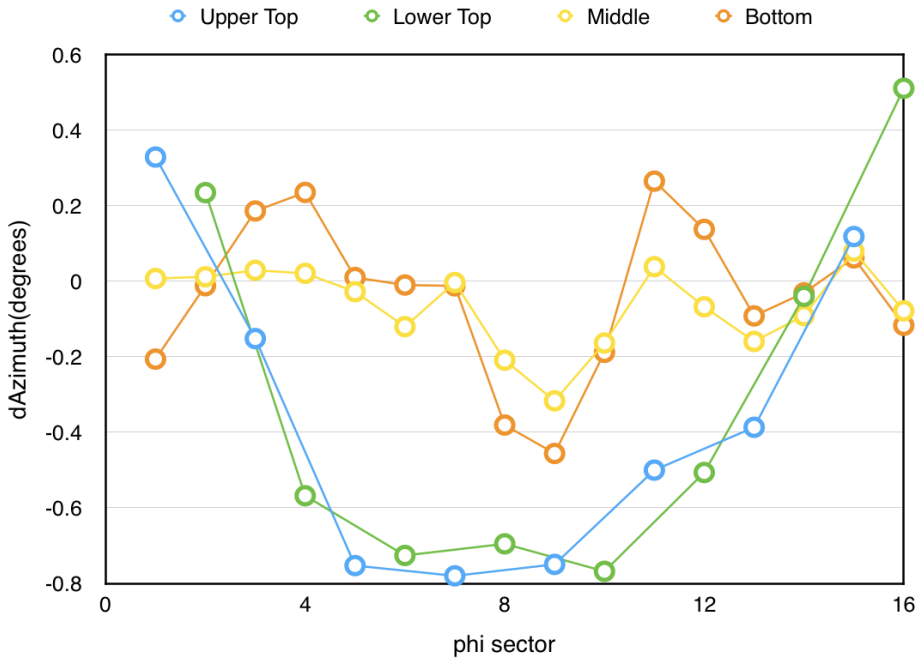

5.4 WAIS Pointing Resolution With Photogrammetry Model

As discussed in Chapter 4, ANITA-IV payload passed near the WAIS pulser station and recorded about 0.17 million calibration events. Those events can be reconstructed using the interferometric method discussed in Chapter 5.1. The event reconstruction gives the most possible direction,$(\theta_{measured}, \phi_{measured})$, of the impulsive signal. Meanwhile the GPS records the location of payload for each event, so it is straightforward to get the expected signal direction $(\theta_{expected}, \phi_{expected})$. The difference between the expected and measured direction for all the WAIS events is shown in Figure 5.6 and Figure 5.7. The standard deviation in the plot is the measure of the angular resolution. For horizontal polarization in Figure 5.6, the resolution is 0.58° for $\delta\phi$ and 0.21° for $\delta\theta$. For vertical polarization in Figure 5.7, the resolution is 0.57° for $\delta\phi$ and 0.24° for $\delta\theta$. The resolution in $\delta\theta$ is better than the resolution in $\delta\phi$ for both polarizations, because the payload antennas are further separated in elevation than azimuth and the resolution is inversely proportional to the distance between antennas.

Figure 5.6: Horizontal polarization $\delta\theta$ vs $\delta\phi$ histogram with respect to the WAIS pointing direction

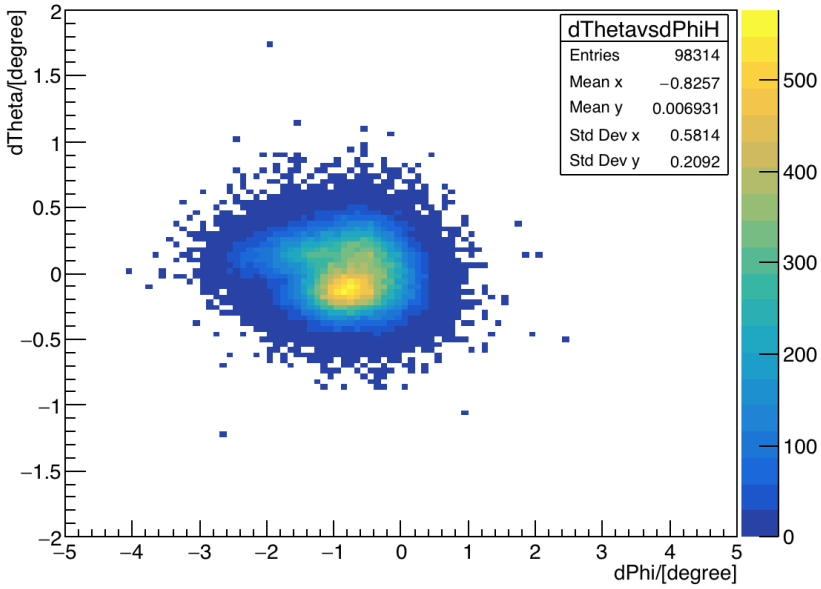

Figure 5.7: Vertical polarization $\delta\theta$ vs $\delta\phi$ histogram with respect to the WAIS pointing direction

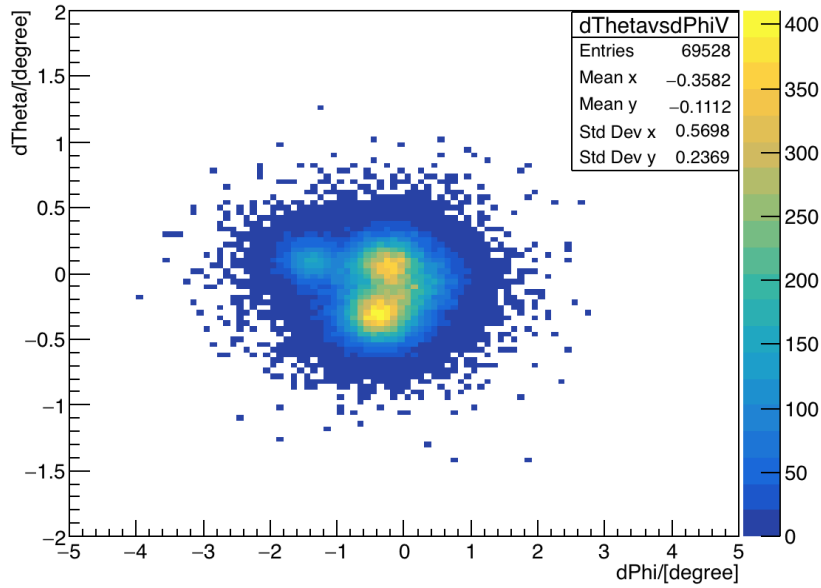

Figure 5.8: $\delta\theta$ vs ϕ plot of all WAIS events containing both H and V polarization. At least to the first order we can see a sinusoidal pattern, which indicates a tilt of payload. In order to fit a function form to the data, this 2D histogram can be further sliced and averaged in $\delta\theta$, which will be shown in Figure 5.9.

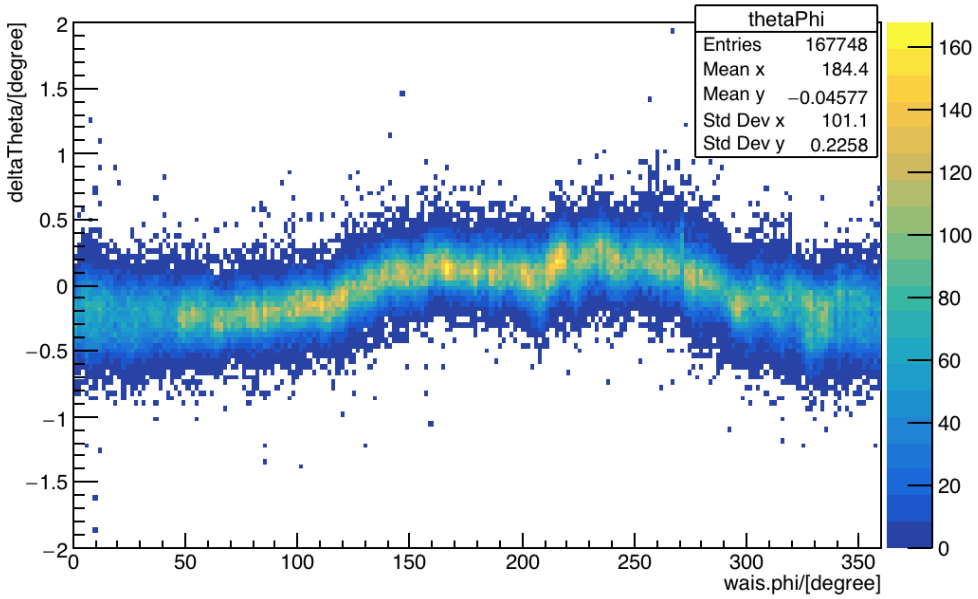

Figure 5.9: The sinusoid fit of averaged $\delta\theta$ vs ϕ. As we can see, there is a $-0.23°$ tilt at $31.56°$ azimuth.

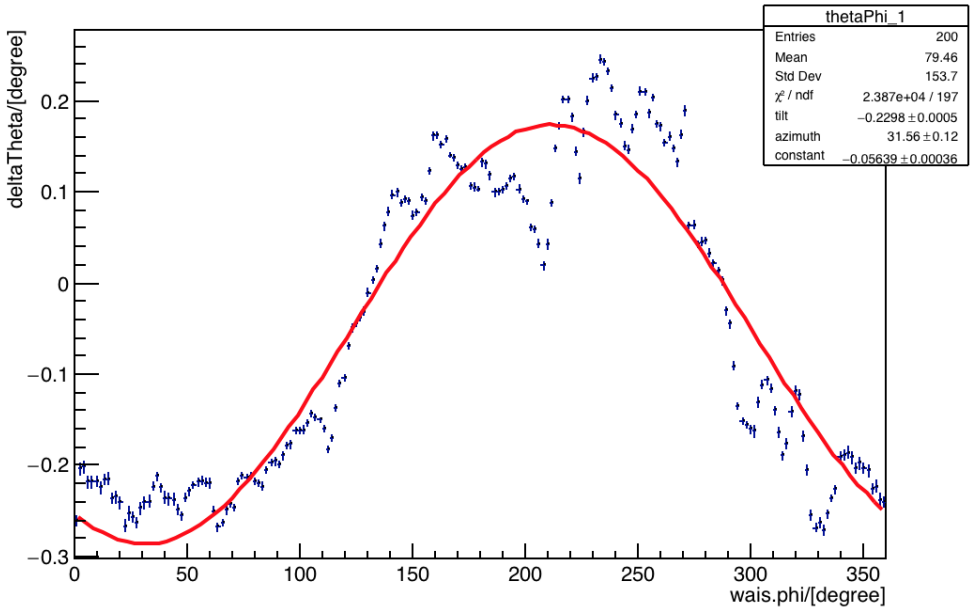

5.5 Payload Tilt Calibration

Even if the photogrammetry model is accurate, the payload's center of mass may not be in line with the central axis of the payload. As a consequence, there could be a tilt due to the effects of gravity. This tilt should be very consistent as the payload rotates. Using the WAIS pulse as a calibration method, we can determine the payload tilt.

Figure 5.8 shows how $\delta\theta$ varies when the WAIS signals come from different ϕ direction. $\delta\theta$ is the θ difference between reconstructed θ and the expected θ from the WAIS signal. The relation is not flat along the zero-line value of the y-axis, but a sinusoid function, which is caused by the tilt of payload. The amplitude of the tilt is relatively small, so we can fit a sinusoid function in Figure 5.9. The parameters in the sinusoid-fitting function are the tilt angle and azimuth, which tells the direction of the tilt, and a constant, just for correcting some systematic errors. As we can see from Figure 5.9, there is a $-0.23°$ tilt occurred at $31.56°$ in azimuth direction. We also looked into different runs, and this tilt is consistent. The tilt angle in azimuth

direction can be decomposed into two perpendicular tilts: pitch and roll. Using some geometry approximation, we have the following equations:

$$cos(pitch)cos(roll) = cos(tilt) \tag{5.2}$$

$$tan(azimuth) = \frac{sin(roll)}{sin(pitch)} \tag{5.3}$$

Considering pitch, roll and tilt are very small angles, we have the approximation that:

$$pitch = -\frac{tilt}{\sqrt{(1 + tan^2(azimuth))}}$$

$$roll = tan(azimuth) \times pitch$$

Inserting the above values of tilt and azimuth, we obtain $pitch = -0.196°$ and $roll = -0.120°$. After setting these pitch and roll offsets, the resolution in $\delta\theta$ improved from 0.22° to 0.16° as shown in Figure 5.10.

However, even though the tilt does exist in our payload, it can be absorbed into the phase center calibrations in Section 5.6, because the phase center calibration has hundreds of free variables to be tuned. Whether or not the tilt calibration is applied, it has little effect on the final event reconstruction. We finally decided not to use the tilt calibration and leave it to the phase center calibration: this will be discussed in Section 5.6.

5.6 Phase Center Calibration

The phase center of an antenna is the apparent center for its wave-front from far-field. Since it is related to the frequency component, signal direction, polarization and distance, the phase center is rather an approximation rather than an exact point. The phase center positions from photogrammetry are just the first approximation. We use the WAIS pulses to further calibrate the phase centers position to a higher precision. As we discussed, the reconstruction process is used to fill up the cross-correlation values in the interferometric map and there are two major steps. The first step is to compute the cross-correlation values as a function of expected ΔT_{ij} for all pairs of antennas, which is the time difference between a pair of antennas. The second step is to get the

Figure 5.10: $\delta\theta$ vs ϕ after applying the pitch and roll offsets. The $\delta\theta$ resolution improves.

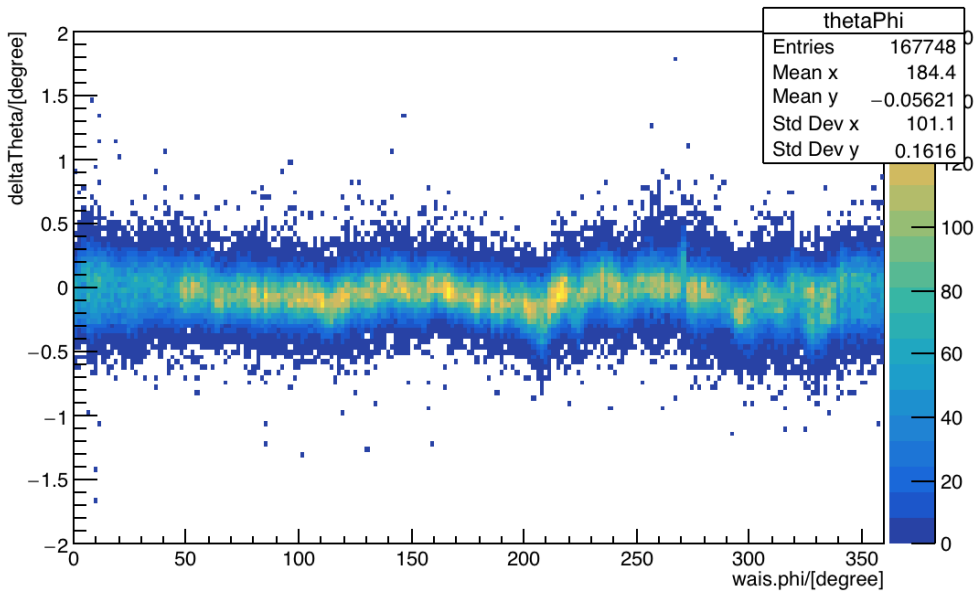

ΔT_{ij} between any pair of antennas and add the corresponding cross-correlation values into the interferometric map. The expected ΔT_{ij} can be quickly calculated as:

$$\Delta T_{ij} = (sin\theta(z_i - z_j) - cos\theta cos(\phi - \phi_i) r_i + cos\theta cos(\phi - \phi_j) r_j)/c + Cable_i - Cable_j \quad (5.4)$$

,where θ and ϕ refer to the direction of the incoming signal. z_i, r_i and ϕ_i refer to the phase center positions for antenna i. z_j, r_j and ϕ_j refer to the phase center positions for antenna j, where j should be not equal to i. $Cable_i$ and $Cable_j$ are the cable delays for antenna i and j in units of ns. The first three terms on the left-hand side of Equation 5.4 calculates the geometry distance between antenna i and j projected onto the signal direction and then divide by the speed of light. The last two terms in Equation 5.4 represents the difference of the time delay in the cables connecting to antenna i and j. By slightly adjusting the phase center variables, i.e. $dR_i, dZ_i, d\phi_i$, and $dCable_i$, the expected time delay ΔT_{ij} would change.

Under perfect conditions, with no noise, plane wave signal and the exact same antennas, the nearest antennas should have the same waveform only with some time delay. By searching for the peak in the cross-correlation values as a function of $\Delta T_{i,j}$, we

can get the most likely time delay $maxCorTimes_{ij}$. This $maxCorTimes_{ij}$ can be equal to ΔT_{ij} in an ideal case. Hence by varying the phase center positions $dR_i, dZ_i, d\phi_i$ and cable delays $dCable_i$, we can get different δtt_{ij} which defined in the following equation:

$$\delta tt_{ij} = \Delta T_{ij} - maxCorTimes_{ij} \tag{5.5}$$

The best calibration are $dR_i, dZ_i, d\phi_i$ and $dCable_i$ which minimize δtt_{ij}. The horizontal and vertical feeds are not at the same positions in the same antenna, so their phase centers can be different and should be calibrated by using the two polarizations of the WAIS events separately. For each polarization, the phase center calibration has $48 \times 4 = 192$ variables. It becomes challenging to find the best calibration since there are too many variables. Also, there is a degeneracy between variables: for example, the variables of cable delays can absorb some degree of freedom in r and z. So the minimization operation is done separately in a few steps. During each step, we fix some variables and tune other variables. The order of minimization steps would affect the final phase center calibrations, and in the end, the best calibration procedure was the one developed by Linda Cremonesi in ANITA-III data analysis [4].

The phase center calibration procedure in ANITA-IV is as follows. The first step is to set $dR_i, dZ_i, d\phi_i$ to zero and letting $dCable_i$ vary. By minimizing δtt_{ij}, a set of $dCable_i$ is found. In the second minimization step, we set $dZ_i, d\phi_i, dCable_i$ fixed and letting dR_i vary. The third minimization step is to set $dR_i, dZ_i, dCable_i$ fixed and letting $d\phi_i$ vary. The last step is to set $dR_i, d\phi_i, dCable_i$ fixed and letting dZ_i vary. Figures 5.11, 5.12, 5.13 and 5.14 are the final calibrations for all antennas after this calibration method has been applied. Thus we can add these phase center changes to the photogrammetry model and add the extra cable delays to measure cable delays. As you can see in Figures 5.15 and 5.16 the standard deviation improves in both θ and ϕ.

Figure 5.11: The extra cable delays vs antenna number from phase center calibration

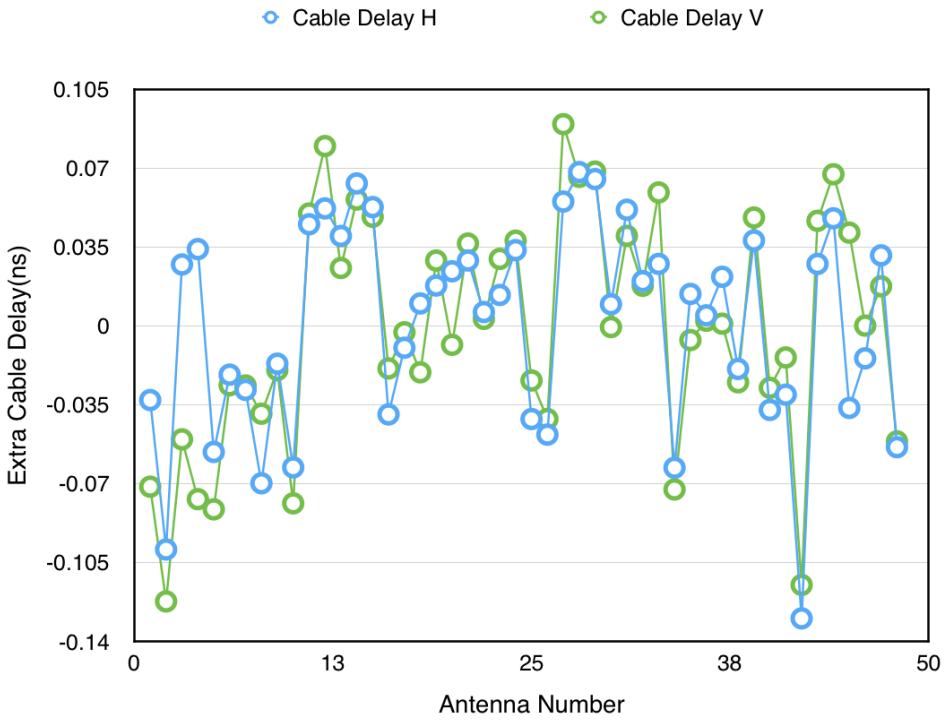

Figure 5.12: Delta radius vs antenna number from phase center calibration. Since the radius for H and V differ by as large as 15cm, the plots are separated for the two polarizations.

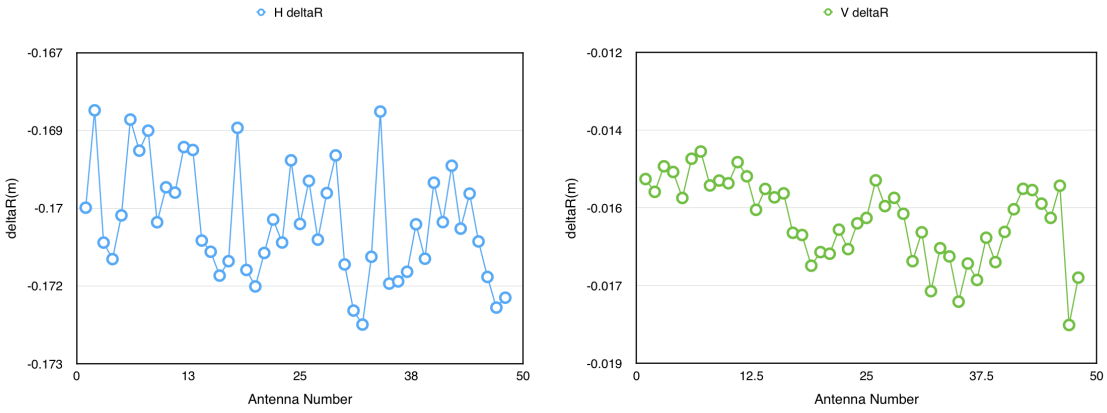

Figure 5.13: Delta ϕ vs antenna number from phase center calibration

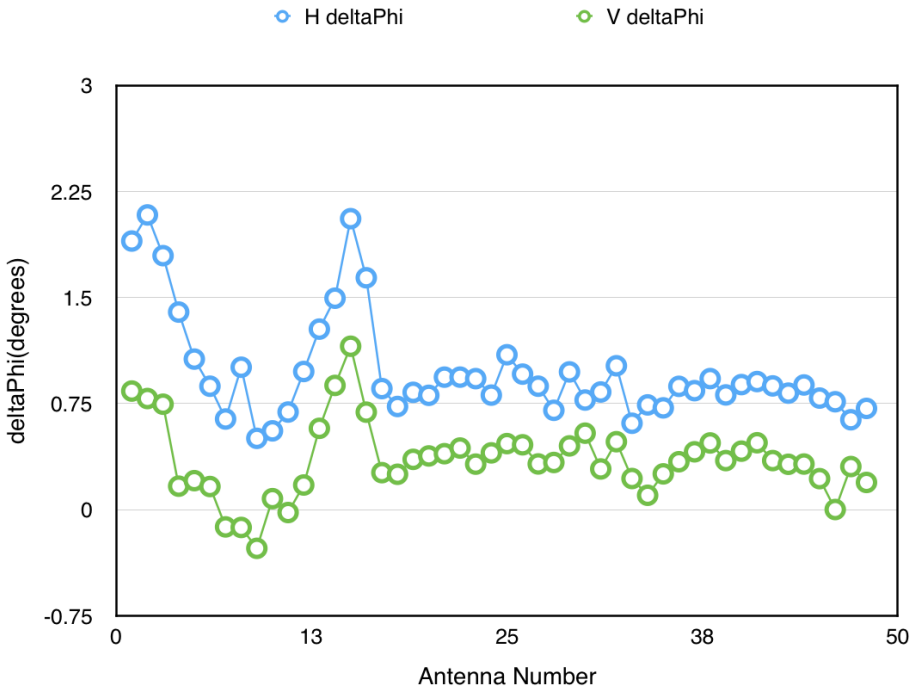

Figure 5.14: Delta Z vs antenna number from phase center calibration

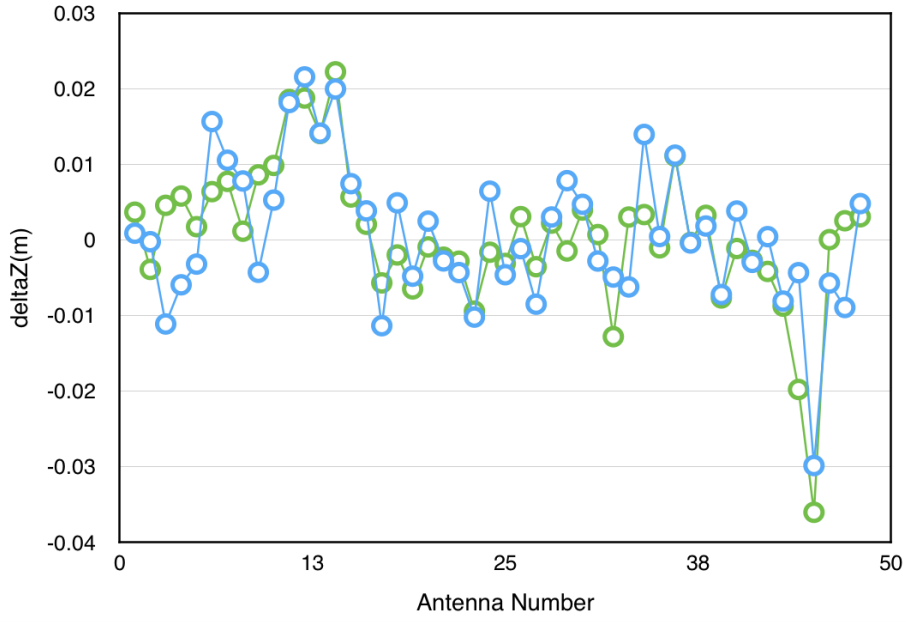

Figure 5.15: Horizontal polarization $\delta\theta$ vs $\delta\phi$ histogram respect to WAIS pointing hypothesis

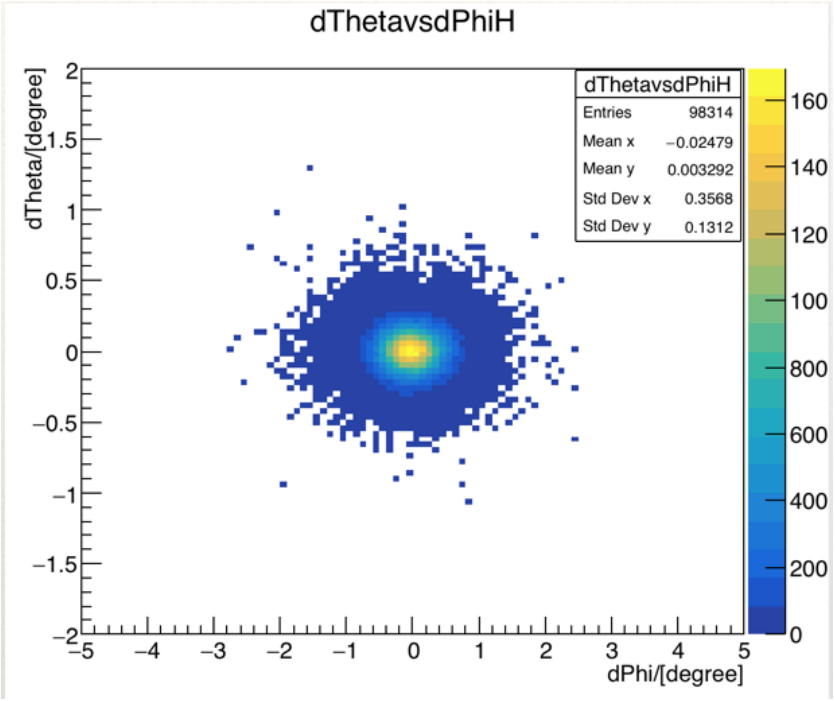

5.7 Off-Axis Delay

The phase center position of a Seavey antenna is not a physical position but just an apparent center for wave-front in long wavelength. So when the beam comes from a different direction, this apparent center would also change, which will cause an extra off-axis time delay. The off-axis time delay depends on the off-axis angle and is just a second order correction to the phase center calibration. The real physics behind this could be related to the shape of the Seavey antenna and the frequency components of the RF. Since this off-axis delay is so small (it is around 0.1 ns), a simple symmetric function in Equation 5.6 could be a good fit to accommodate this off-axis delay. In Equation 5.6, ϕ is the azimuth angle off the bore-sight of the Seavey in units of degree. c_2 and c_4 are the parameters that could be figured out from fitting the data. Though the elevation angle $d\theta$ can also affect the off-axis delay, considering that all the antenna cant the same -10° in elevation, the $d\theta$ off-axis delays for a pair of antennas should

Figure 5.16: Vertical polarization $\delta\theta$ vs $\delta\phi$ histogram respect to WAIS pointing hypothesis

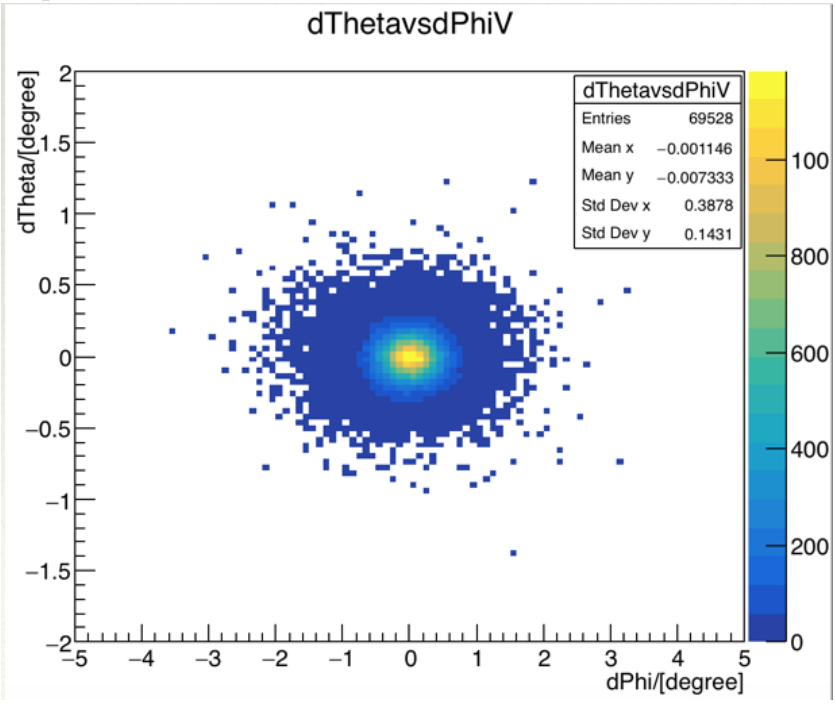

cancel out in the first order. As a result, the $d\theta$ off-axis delay can be neglected and only the $d\phi$ off-axis delay should be considered.

$$f(\phi) = c_2\phi^2 + c_4\phi^4 \tag{5.6}$$

For any one of the WAIS events, five phi sectors, i.e., 15 antennas, near the triggered phi sector would be used to calibrate the phase center. The total number of pairs satisfying this condition is 78. Among these 78 pairs, the antennas belong to only three classes: the same phi sector, one phi sector apart or two phi sectors apart. For the same phi sector, two antennas are just facing the same direction so the off-axis delay would cancel out: this case is of no interest to us. For one phi sector apart pair, the $\Delta\Delta t$ vs the $\delta\phi$ is shown in Figure 5.17. $\Delta\Delta t$ is defined as $\delta t_{measured} - \delta t_{expected}$. $\delta\phi$ is the expected WAIS ϕ relative to the middle ϕ position between the antenna pair. The black line in the middle of the histogram is the average

Figure 5.17: $\Delta\Delta t$ vs $\delta\phi$ for all 1 phi sector apart pairs. This contains both H pol and V pol since their pattern is quite similar. The fit parameters are $c_2 = -4.30 \times 10^{-6}$ and $c_4 = 1.30 \times 10^{-8}$. The units in the palette are the number of antenna pairs per bin of the 2D histogram.

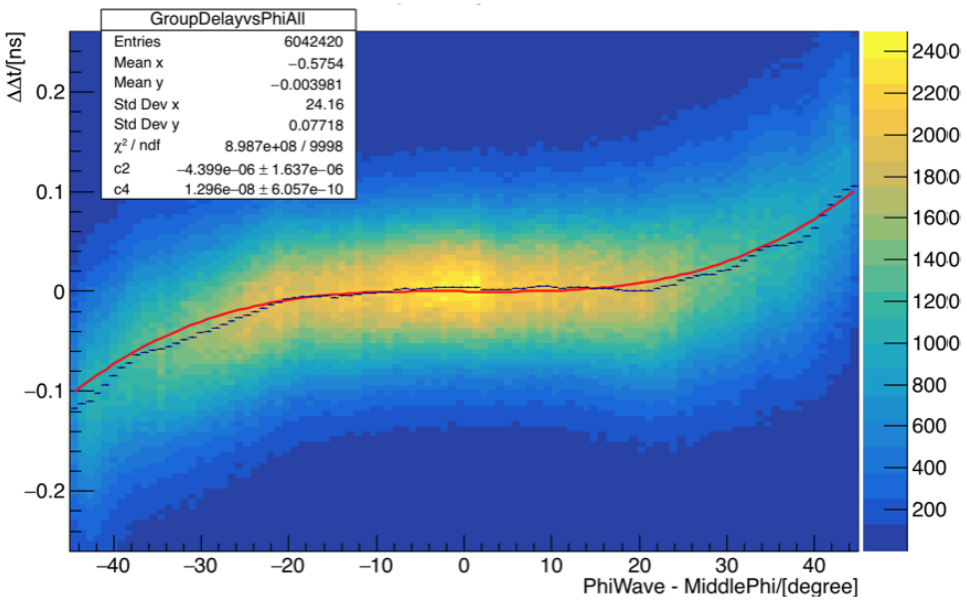

for each Y-axis slices, and it is anti-symmetric, and a simple math function can fit it well. First, for each antenna, we calculate its only off-axis delay. Then the relative off-axis delays between antenna pairs are the difference between them. The fitting function is $\Delta\Delta t = f(\phi + 11.25°) - f(\phi - 11.25°)$, where the fitting coefficients in f (see Equation 5.6) are $c_2 = -4.30 \times 10^{-6}$ and $c_4 = 1.30 \times 10^{-8}$.

For the 2 phi sectors apart pairs, similar histograms are shown in Figure 5.18. Now the fitting function becomes $\Delta\Delta t = f(\phi + 22.5°) - f(\phi - 22.5°)$. And the fitting coefficients are $c_2 = -5.6 \times 10^{-6}$ and $c_4 = 1.25 \times 10^{-8}$: these values are consistent with the values which we obtained from the data in Figure 5.17. So the final fit to use is obtained by taking the average of the two cases. The final off-axis fit function is $f(\phi) = -4.91 \times 10^{-6}\phi^2 + 1.29 \times 10^{-8}\phi^4$.

Figure 5.18: $\Delta\Delta t$ vs $\delta\phi$ for all 2 phi sectors apart pairs. This contains both H pol and V pol since their pattern is quite similar. The fit parameters are $c_2 = -5.6 \times 10^{-6}$ and $c_4 = 1.25 \times 10^{-8}$. The units in the palette are the number of antenna pairs per bin of the 2D histogram.

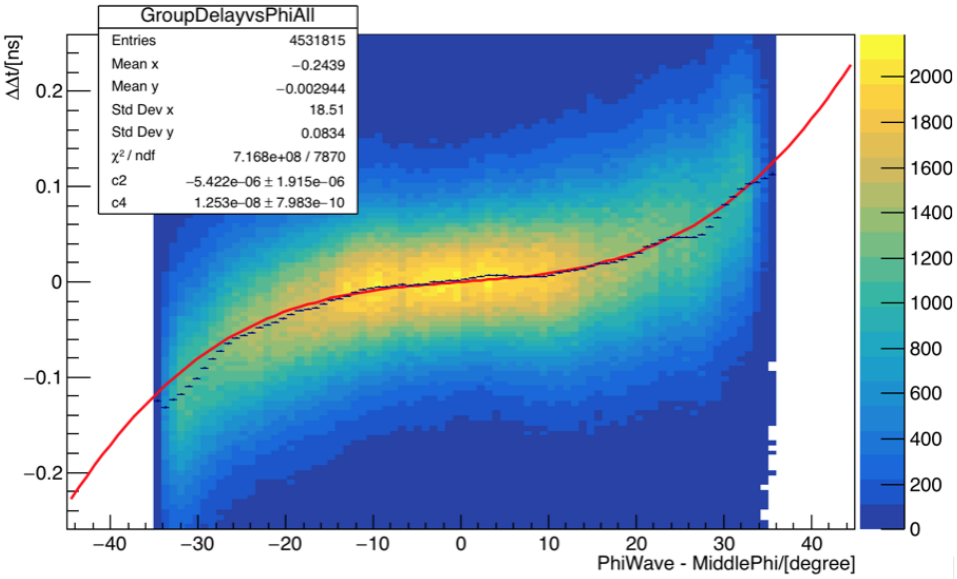

Chapter 6

ANALYSIS OF THE ANITA-IV DATA

After the Event Reconstruction and all the calibrations, this Chapter focuses on the data analysis that looks for the UHE neutrino candidate events. Searching for cosmic ray events is not the major task in my analysis but the technique is similar so it is included. The first step is to use quality cuts and thermal cuts to find the good impulsive RF events. Then those events should be projected to ice and clustered. The singlets isolated from any know base is defined as the signal region in my analysis. HPol and VPol events in the signal region are CR and neutrino candidates respectively. However, the signal region is blinded until all the cut parameters are chosen and fixed. The unblinding of the signal region will be discussed in Chapter 7.

6.1 Datasets

There are three datasets in my analysis: 1) The WAIS samples, 2) the thermal samples, 3) the Monte Carlo (MC) samples. The first two datasets are from real flight data. The third dataset is from IceMC simulation. The first and third datasets are regarded as the impulsive signal events. The second dataset contains most of the flight events where we search for the UHE cosmic rays and neutrinos among millions of background events. Depending on the product of its impulsivity and map peak value in the corresponding polarization, each event can be classified as an either HPol or VPol event.

6.1.1 WAIS samples

The WAIS samples only include the WAIS calibration pulses from run 120 to run 153. 215135 WAIS events are identified by using the timing and GPS distance

(UCorrelator::isWAISVPol and UCorrelator::isWAISHPol). Those WAIS samples are impulsive RF events and can served as a dataset of anthropogenic impulsive signal events. More details about WAIS have already been discussed in Section 4.2. After a simple timing selection, the WAIS sample still needs to be further cleaned by quality cuts (Section 6.2) and $goodPointingWais$ cut. $goodPointingWais$ cut requires $\delta\theta < 2^\circ$ and $\delta\phi < 5^\circ$, where $\delta\theta$ and $\delta\phi$ are from Figures 5.15 and 5.16.

6.1.2 Thermal samples

After the WAIS samples are removed from all the flight events, the rest of the data is the so-called thermal samples because most of the events are just thermal noise events. There are 77886924 events in the thermal sample. Some of them have low reconstruction quality, so the first step is applying quality cuts in Section 6.2. The thermal samples are dominated by the thermal background events but also include all the impulsive events. The thermal cut to remove the thermal background events will be discussed in Section 6.4. After the thermal cut, the remaining are impulsive events which are mainly composed of anthropogenic backgrounds. The clustering analysis in Section 6.5 will discuss how to remove anthropogenic backgrounds in a further step.

6.1.3 MC samples

The third dataset, the MC samples, contains simulated neutrino events generated by the Monte Carlo simulation software called IceMC. Two million weighted neutrinos are generated using models including the UHE neutrino flux, Antarctica Ice map and ANITA Instruments. These data are mainly used as neutrino signal events and are useful for determining the thermal cut and doing efficiency analysis. The MC samples will be cleaned by quality cuts and $goodPointingMC$ cut, which requires $\delta_\theta < 2^\circ$ and $\delta_\phi < 5^\circ$.

6.2 Events Quality Cuts

The quality cut is a set of cuts to remove anomalous events that not reconstruct well or saturate the digitizer. The events removed by quality cut are not thermal

background, anthropogenic background nor signal. It is defined as an intersection of several individual cuts:

$$qualityCut = isReal \;\&\&\; notGlitch \;\&\&\; notBadReconstruction \;\&\&\; notBlast \;\&\&\; triggered \;\&\&\; notMasked \;\&\&\; notStrongCW \;\&\&\; notHical$$

An event needs to have *qualityCut* to be true to pass to the next stage of analysis. Each individual cut is discussed in the following sections.

6.2.1 *isReal* cut

The Cut *isReal* requires the trigger type to be (Radio Frequency) RF and the reconstructed θ should be between $-60°$ and $50°$. The reason is that, apart from the RF trigger, there are software triggered events at a fixed time in each second. Restricting the trigger type to RF will let us get rid of all the software triggers. The choice of θ range has two reasons: 1) Our candidate events such as UHE cosmic ray or UHE neutrinos RF are likely coming from between $\theta = -30°$ and $\theta = 0°$. 2) Our payload antennas cant $10°$ below horizontal and are hence not sensitive to elevation far from the antenna bore-sights. So events that are not RF triggered events or reconstructed too far from the expected elevation angle will be removed by this cut. The standalone cut efficiency is 92.9% for the thermal samples, 99.9995% for the WAIS samples and 100% for the MC samples.

6.2.2 *notGlitch* cut

The glitch events are events whose waveforms have extremely large voltage up to $1000mV$. The causes of the glitch events are likely to be hardware and chip anomaly. In Figure 6.1, all the sample ADC values vs. the RMS values from all events in run 292 are plotted. There are three kinds of glitches. The type 1 glitch only occurs at SURF 10 chip B. It is due to the bit corruption and can be fixed by subtracting 512 during the waveform calibration phase. For type 2 and type 3 glitches, we flag them and remove them later in the quality cuts. If an event's waveform's ADC value is larger

Figure 6.1: The sample ADC values vs. the RMS values from all waveforms in run 292. There are three kinds of glitches. The type 1 glitch only occurs at SURF 10 chip B. It is due to the bit corruption and can be fixed by subtracting 512 during the waveform calibration phase. For type 2 and type 3 glitches, we can flag them by a simple ADC value threshold cut, 470 , and remove them in quality cuts.

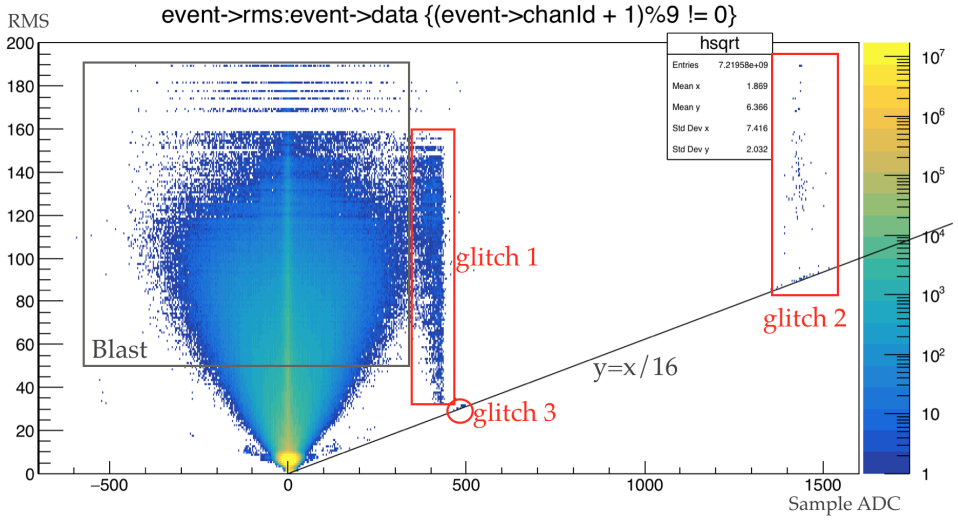

than 470 (nearly 1000 mV after calibration) then it will be regarded as a glitch event. The standalone cut efficiency is 99.94% for the thermal samples, 99.95% for the WAIS samples and 99.95% for the MC samples.

6.2.3 *notBadReconstruction* cut

From the event reconstruction, the peak $(\theta_{rough}, \phi_{rough})$ in a rough map and the peak (θ, ϕ) in a zoomed map may not be the same. If the rough map peak $(\theta_{rough}, \phi_{rough})$ is far from the "true" direction, then the zoomed peak (θ, ϕ) is likely to be on the edge of zoomed map, as shown in Figure 6.2. The peak differences are defined as $(\theta_{rough} - \theta, \phi_{rough} - \phi)$. If the zoomed peak does not match the rough peak such that

$$\begin{aligned} |\theta_{rough} - \theta| &> 3^\circ \\ |\phi_{rough} - \phi| &> 6^\circ \end{aligned} \tag{6.1}$$

then we should not trust the zoomed peak (θ, ϕ) as the true direction. The events that satisfy Equation 6.1 would be removed by *notBadReconstruction* cut. The standalone

Figure 6.2: The distribution of $\phi_{rough} - \phi$ and $\theta_{rough} - \theta$ from the reconstruction. The spikes near $+/-9^{\circ}$ are the possible bad reconstructed events.

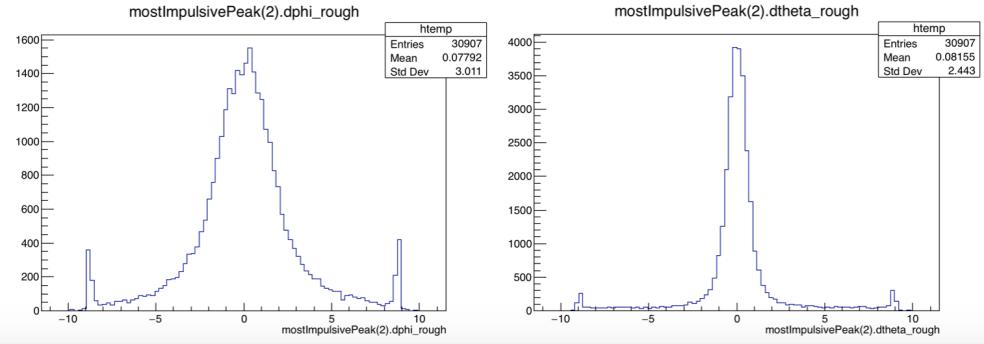

cut efficiency is 82.21% for the thermal samples, 99.53% for the WAIS samples and 98.20% for the MC samples.

6.2.4 *notBlast* cut

The BLAST events are strong impulsive events that do not show a plane wave correlation between antennas. Each ANITA flights contain these events and the true reason to cause these is still unknown. The averaged event rate for BLAST is 0.58 Hz in ANITA-IV flight. A 3D position reconstruction of BLAST events indicates they are likely to originate locally in the payload. The current explanation is that BLAST events are from local sparks or other electromagnetic surges in the payload. Figure 6.6 and Figure 6.7 shows a waveform and reconstruction of a BLAST event 67834366 as an example.

Since BLAST events are relatively strong and impulsive, they should be removed before applying the thermal cuts. In order to remove the BLAST events, a multi-parameter cut was developed, incorporating the number of channels with RMS $>$ 100 mV to be larger than 30 and the power ratio between the bottom and top ring is not too large or small. This is shown in Figure 6.3. The standalone cut efficiency is 98.55% for the thermal samples, 99.98% for the WAIS samples and 99.99% for the MC samples.

Figure 6.3: The BLAST event cut.

```
flags->isPayloadBlast =
  summary->countChannelAboveThreshold(100)>30 ||
  flags->maxBottomToTopRatio[0] <0.9 || flags->maxBottomToTopRatio[0] >2.6 ||
  flags->maxBottomToTopRatio[1] <0.9 || flags->maxBottomToTopRatio[1] >2.6 ||
  flags->meanPower[3]/flags->meanPower[1] <0.2 || flags->meanPower[3]/flags->meanPower[1] >1.7;
```

Figure 6.4: The distribution of hwAngle for the thermal samples.

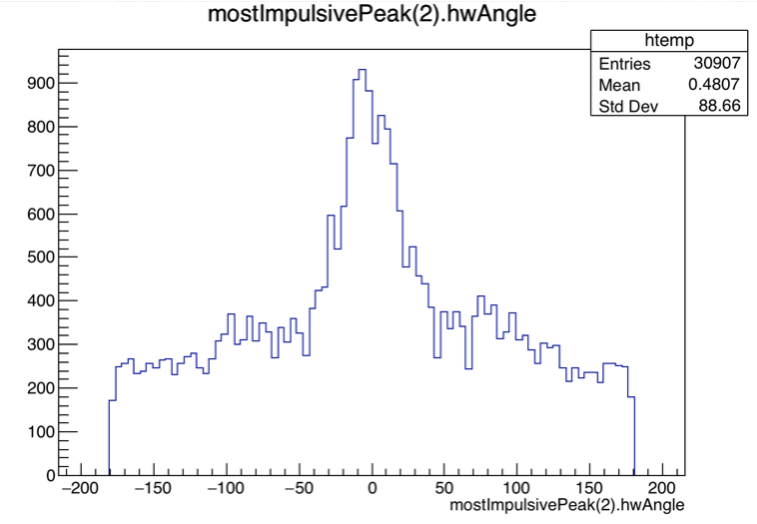

6.2.5 *triggered* cut

The ANITA-IV data stream also records the triggered phi sectors for all RF triggered events. If the difference between the reconstructed phi sector and the trigger phi sector (labelled as hwAngle in summary file) is too large, it means the reconstruction does not match the triggered direction. Those events are removed. Figure 6.4 and Figure 6.5 shows the distribution of hwAngle for thermal samples and WAIS samples. We restrict $|$ hwAngle $| < 60°$ as our *triggered* cut. The standalone cut efficiency is 43.21% for the thermal samples, 99.99% for the WAIS samples and 99.99% for the MC samples.

Figure 6.5: The distribution of hwAngle for the WAIS samples.

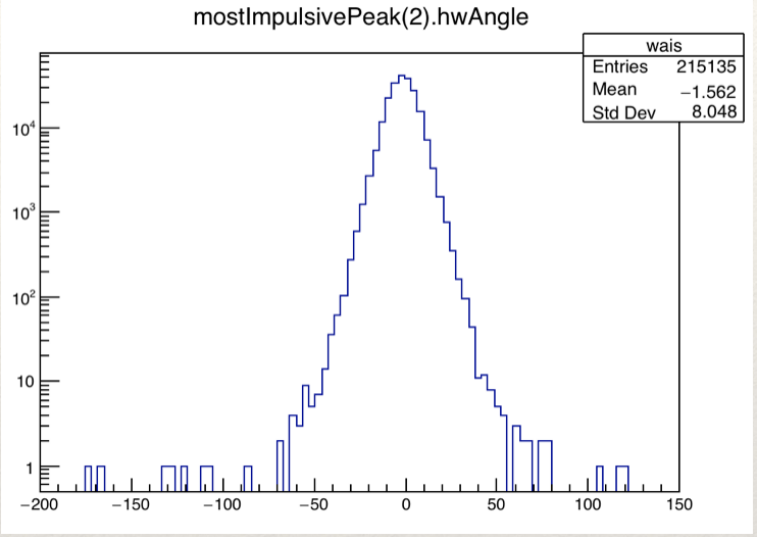

Figure 6.6: The waveform of a BLAST event 67834366.

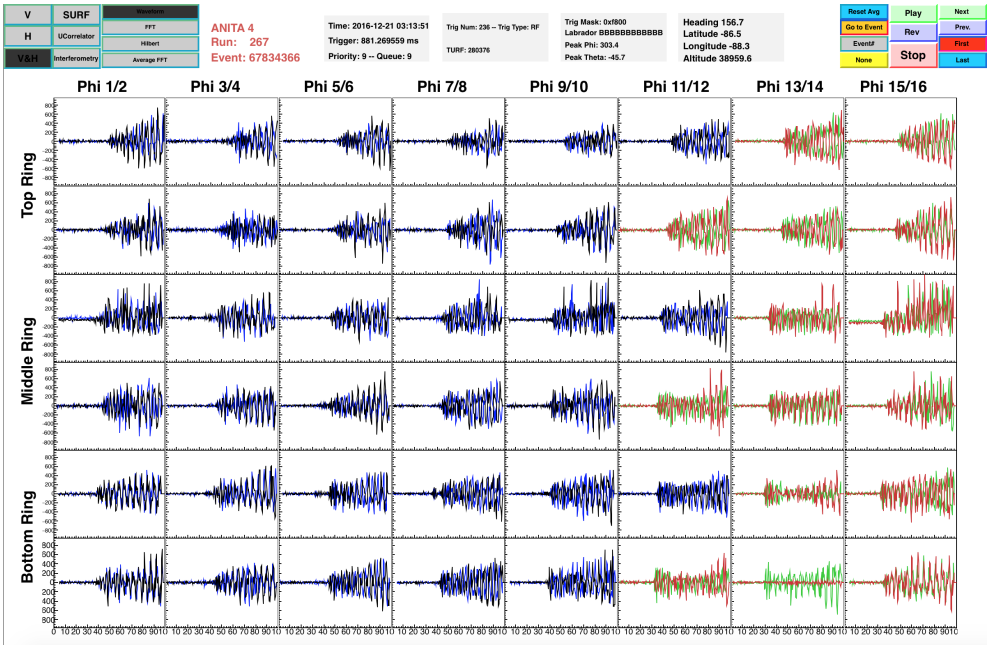

Figure 6.7: The reconstruction of a BLAST event 67834366 after filtering.

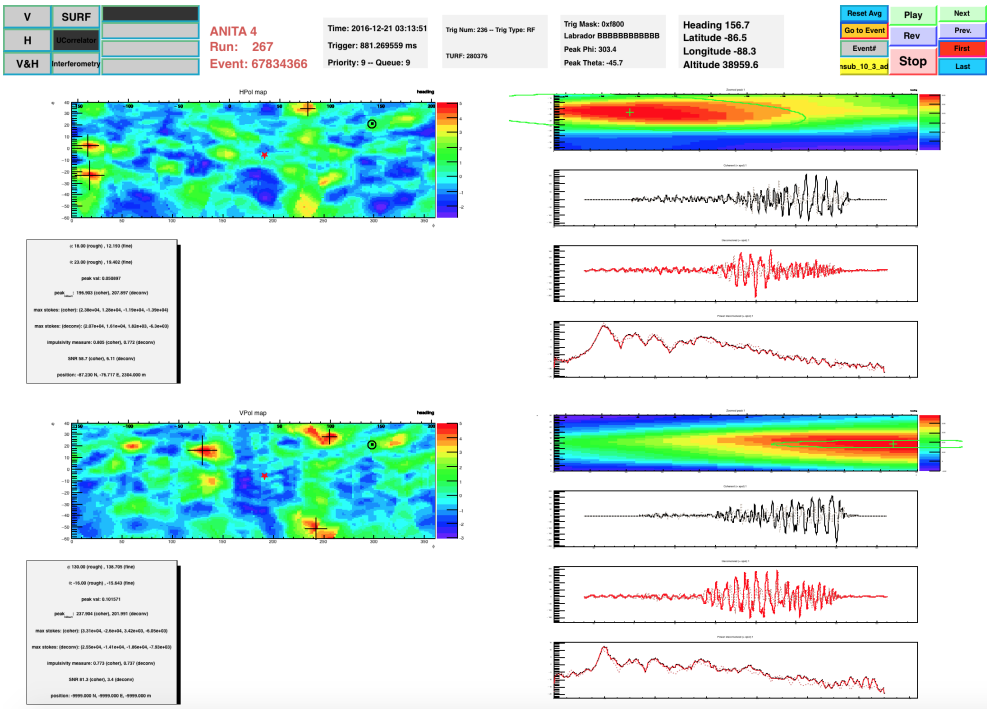

6.2.6 *notMasked* cut

If a phi sector is continuously triggered, it is likely that the phi sector is facing some strong CW sources. As we discussed in Section 2.3.4, in order to lower the digitization deadtime, the masking can be applied to the phi sectors that are continuously busy. The masked fraction during ANITA-IV is shown in the bottom plot of Figure 2.13. If the reconstructed direction's phi sector is the same as the masked phi sector, then the reconstruction cannot be trusted. 98.5% of the thermal samples remain after *notMasked* cut. The standalone cut efficiency is 98.45% for the thermal samples, 99.97% for the WAIS samples and 96.30% for the MC samples.

6.2.7 *notStrongCW* cut

Before the filtering, a CW event usually has a large coherent SNR compared to deconvolved SNRs. A cut on the ratio of SNR would remove most of these CW events. As in Figure 6.8, *notStrongCW* is a cut on the SNR ratio of CSW and DSW to be less than 5.5. Though most of CW power will be removed by the sine-subtraction filter, it is good if we can remove these because they are not neutrinos or CR we are looking for.

6.2.8 *notHical* cut

As discussed in Section 4.3 , two HiCal-2 flights were active during the ANITA-IV flight. Each HiCal-2 had its own GPS, and we recorded the period when the transmitters were turned on. For any event, if the Hical is on and it is within $min(5^\circ, 6\times \sigma_\phi(SNR))$ degrees in the peak phi direction, the event will be removed. The model for ϕ resolution as a function of *snr* will be discussed in Section 6.5.1. The expected number of HiCal events surviving from this cut is 3.5×10^{-4} event by assuming a normal distribution with $\sigma_\phi(SNR)$. The efficiency for thermal events is 97.3%. The efficiency for IceMC events is 99.97%. So *notHical* cut cleans up the HiCal-2 events and maintains a high analysis efficiency.

Figure 6.8: The *coherent_snr/deconvolved_snr* distribution of 1% of the thermal samples.

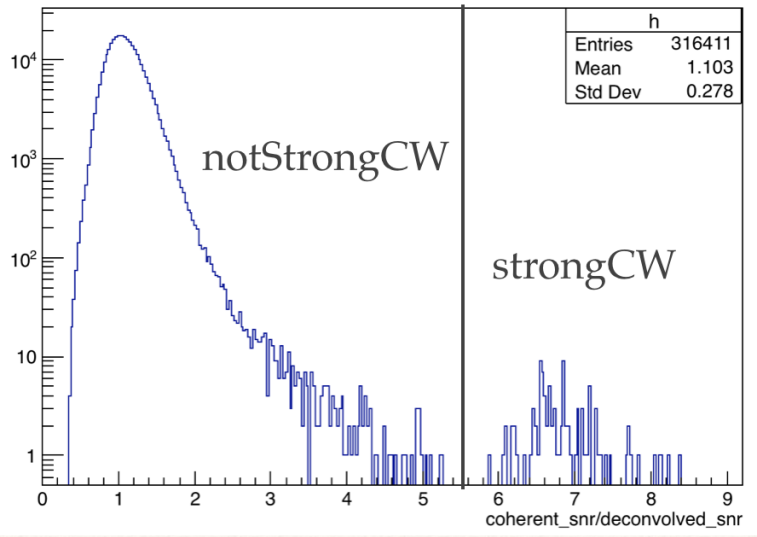

6.3 Quality Cuts Efficiency

Figure 6.1 displays the efficiencies of all three kinds of datasets passing each quality cut. The efficiency is the percentage of events remaining after applying each quality cut. There are two ways of arranging those cuts. "Passing if only" means applying each quality cut separately. "Passing in sequence" means applying those quality cuts in sequence from the first row to the last row. The final efficiency in these "Passing in sequence" column is the overall efficiency. From Figure 6.1, 31.9 percent of the thermal events, 97.5 percent of the WAIS sample and 91.9 percent of IceMC sample remain after applying all the quality cuts.

6.4 Thermal Cuts

After the quality cuts, there are 30871530 events remaining in the thermal sample. Most of them are just thermal noises and a small portion of them are impulsive events. The main components of the thermal noise are due to several different sources: 1) the blackbody radiation from the ice and sky; 2) the radiation from the sun and its reflection from the ice; 3)the Continuous Wave (CW) radiation from satellites. These

Table 6.1: The efficiencies for each step of quality cuts applying to three kinds of datasets. There are two ways of arranging those cuts. "Passing if only" means applying each quality cuts separately. "Passing in sequence" means applying those quality cuts in sequence from the first row to the last row. The final efficiency in these "Passing in sequence" column is the overall efficiency. For the thermal samples, the quality cut efficiency is 31.9%. For the WAIS samples, the quality cut efficiency is 97.5%. For the MC samples, the quality cut efficiency is 91.9%.

QualityCuts	10% data pass in sequence	10% data pass if only	Wais passes in sequence	Wais pass if only	minBias Kotera max MC pass in sequence	minBias Kotera max MC pass if only
no cut	8927918(100%)	8927918(100%)	215135(100%)	215135(100%)	2466.31(100%)	2466.31(100%)
isReal	8294960(92.9104%)	8294960(92.9104%)	215134(99.9995%)	215134(99.9995%)	2466.31(100%)	2466.31(100%)
notGlitch	8289950(92.8542%)	8922451(99.9388%)	215024(99.9484%)	215025(99.9489%)	2465.2(99.9548%)	2465.2(99.9548%)
notBadReconstruction	6835923(76.5679%)	7339458(82.2079%)	214003(99.4738%)	214114(99.5254%)	2420.67(98.1494%)	2421.79(98.1946%)
notBlast	6755126(75.6629%)	8798588(98.5514%)	213982(99.4641%)	215097(99.9823%)	2420.43(98.1395%)	2466.02(99.9879%)
triggered	2969414(33.2599%)	3858504(43.2184%)	213957(99.4524%)	215107(99.987%)	2360.79(95.7214%)	2405.16(97.5206%)
notMasked	2914905(32.6493%)	8790043(98.4557%)	213887(99.4199%)	215065(99.9675%)	2272.57(92.1442%)	2374.96(96.2957%)
notStrongCW	2913989(32.6391%)	8912772(99.8304%)	213887(99.4199%)	215135(100%)	2272.57(92.1442%)	2466.31(100%)
notHical	2843995(31.8551%)	8706396(97.5188%)	213887(99.4199%)	215135(100%)	2269.02(92.0005%)	2462.5(99.8453%)
goodPointingWais	NA	NA	213832(99.3943%)	215058(99.9642%)	NA	NA
goodPointingMC	NA	NA	NA	NA	2266.09(91.8815%)	2461.72(99.8137%)

impulsive events are mostly from anthropogenic sources and they constitute the background for our signal events, which are UHEN events or cosmic ray events. So a feature called *impulsivity* is developed to measure how impulsive the waveform is. *impulsivity* quantitatively describes how the power is distributed along the deconvolved summed waveform. If most power is around the Hilbert Peak in the coherently summed waveform, then the *impulsivity* is close to 1. If the power is essentially uniformly distributed along the coherently summed waveform, its *impulsivity* is near 0. The distributions of *impulsivity* for the thermal samples, the WAIS samples, and the MC samples are shown in Figure 6.9. As we can see, the above horizon events do not have any impulsive events, because the ionosphere can disperse all impulsive RF signals from the Sun. The distribution of the above horizontal events can be fitted as a model of thermal background events distribution. The plot uses a log scale. With a large enough *impulsivity* cut, the expected thermal background from below horizontal would be reasonably low. In Section 6.6.3, we show that a thermal cut of impulsivity > 0.752 would leave a 0.1 thermal background for events directed from below horizontal.

The event density map of thermal events on the Antarctica ice is shown in Figure 6.10. Brighter colors refer to a higher event density on the corresponding location. The light blue color on the map is consistent with the ANTIA-IV flight path.

It is useful and interesting to see the distribution of all the events from several different perspectives. For example, Figure 6.11, Figure 6.12 and Figure 6.13 display the reconstructed peak (θ, ϕ) in different coordinates. For each of them, on the left, there are all the events which pass the quality cuts. On the right, there are events passing quality cuts and impulsivity cut (or thermal cut). The red color on the left plots presents the CW events from the satellites. From the left plot to the right plot, impulsivity cut removes the thermal noise from the Sun or CW events from the satellites. Figure 6.11 shows distribution of reconstruction direction for all events in the payload coordinate. If we subtract the payload heading from ϕ then we get the plot in the local Earth coordinate in Figure 6.12, where the satellite events (red color) are near horizon and centered in the north direction. The traces of bases on the ground, such

Figure 6.9: The distribution of impulsivity for the above-horizontal thermal samples, the below-horizontal thermal samples, IceMC samples, and WAIS samples. No impulsive events are from above horizontal due to the ionosphere.

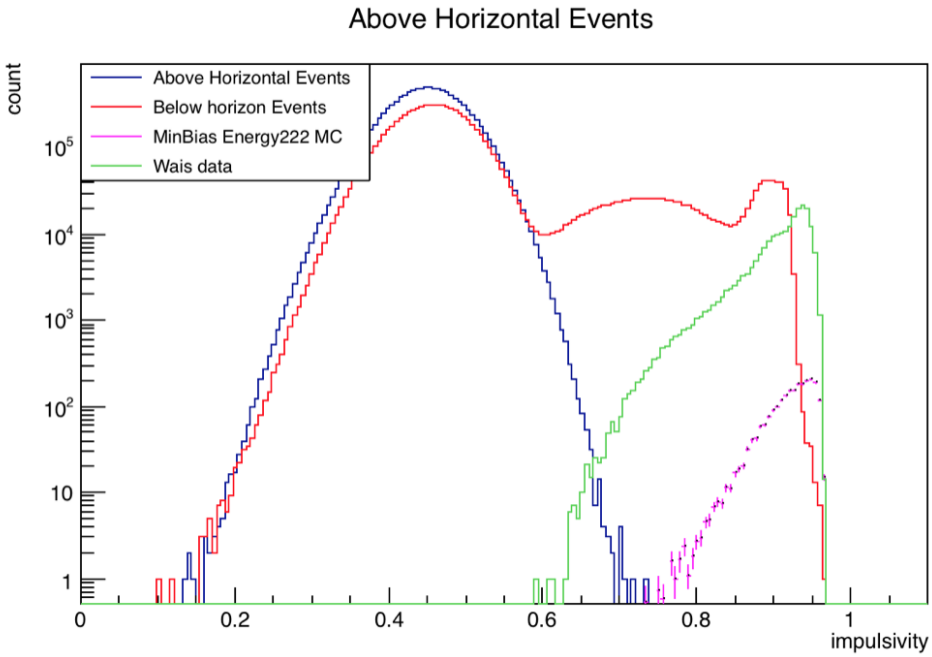

as the WAIS and the South Pole, can also be viewed from the figure. If we subtract the payload heading and longitude from ϕ, then we get Figure 6.13 in the fixed Earth coordinate, where we can see five geostationary (or geosynchronous) satellites are in fixed azimuth direction from Earth. A satellite stripe plot is shown in Figure 6.14 that how the number of satellites can be viewed from ANITA changed when ANITA flew around Antarctica.

6.5 Event Projection on Antarctica Ice

After the thermal cuts at impulsivity > 0.752, only 0.86% (or 745955) the most impulsive events remain, where most of the events are from anthropogenic bases. In order to discriminate the anthropogenic sources from the possible neutrino or CR candidates, those impulsive events should be projected to Antarctica and clustered by distance. Since our payload has good sensitivity to the impulsive signals, the anthropogenic events tend to cluster together. The signal events, such as CR and UHE neutrino events, are randomly distributed and are likely to be isolated events. The events not clustering with any other events are called singlets, and they are the possible signal candidates with a certain background (which will be estimated in Section 6.6.3).

Given the GPS information, we know exactly the heading, longitude, latitude and altitude of the payload. From the peak of the interferometric map, the direction θ, ϕ would intersect the ice surface. Atmospheric refraction is considered in this ray tracing process. We use the high-resolution Antarctica telemetry data called Radarsat Antarctic Mapping Project Digital Elevation Model(Rampdem) as the Antarctica surface model. All events below horizon can intersect at a position on the ice surface. Since the peak θ, ϕ from the interferometric map has pointing uncertainties, it is also intuitive to show the uncertainties on the Antarctica surface. The relation between event pointing resolution σ_θ, σ_ϕ and SNR, known as the pointing resolution model, will be discussed in the next section 6.5.1. As a consequence, each event projected on

Figure 6.10: The 10% thermal events projected on the Antarctica Ice. In order to have a better contrast in the distribution, a log scale is in use in the color palette. The bright spots follow the payload flight path. One contribution of thermal events is the satellite. In this plot, you can see parallel stripes caused by satellite events. The color palette on top left denotes for the events density in arbitrary units. The color palette on the bottom left denotes for the ice thickness.

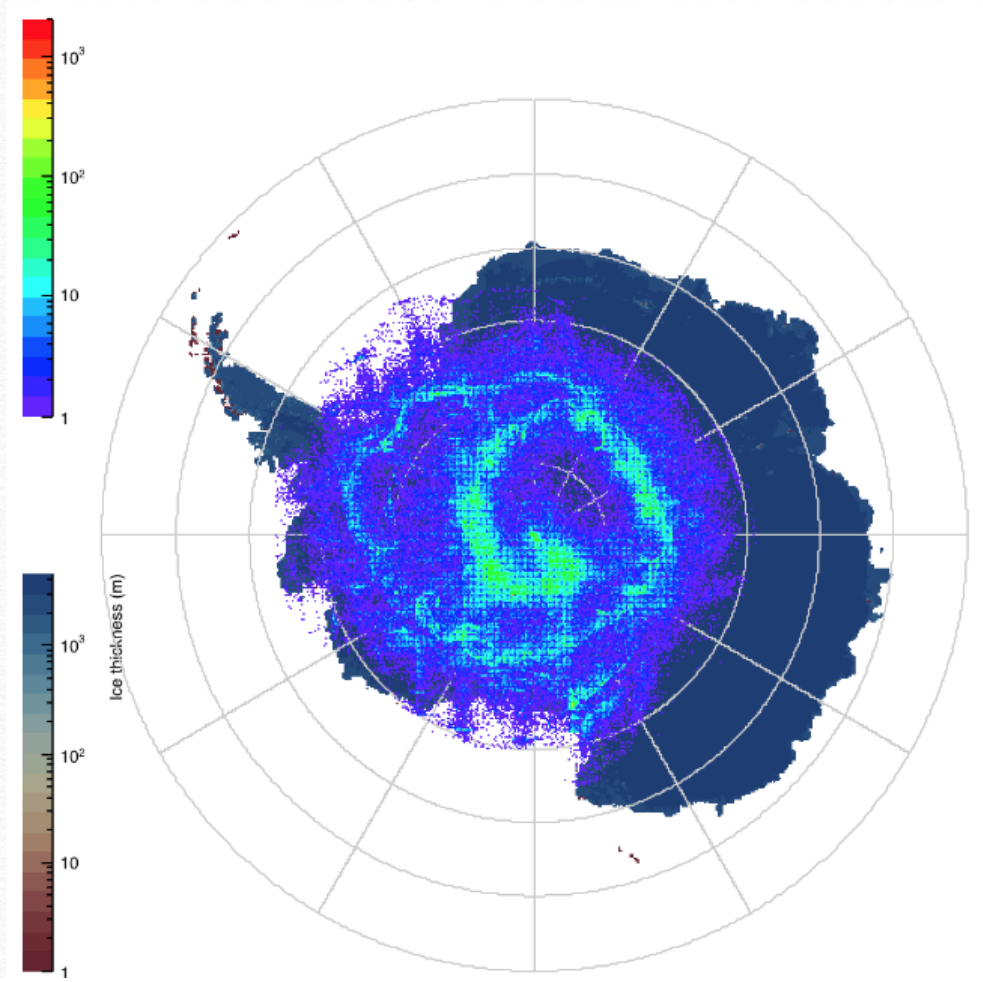

Figure 6.11: The 2D histogram of reconstructed events direction (θ, ϕ) in a payload coordinate. The left plot is all the thermal events passing quality cuts. The right plot is only the impulsive events passing the quality cuts and the thermal cut.

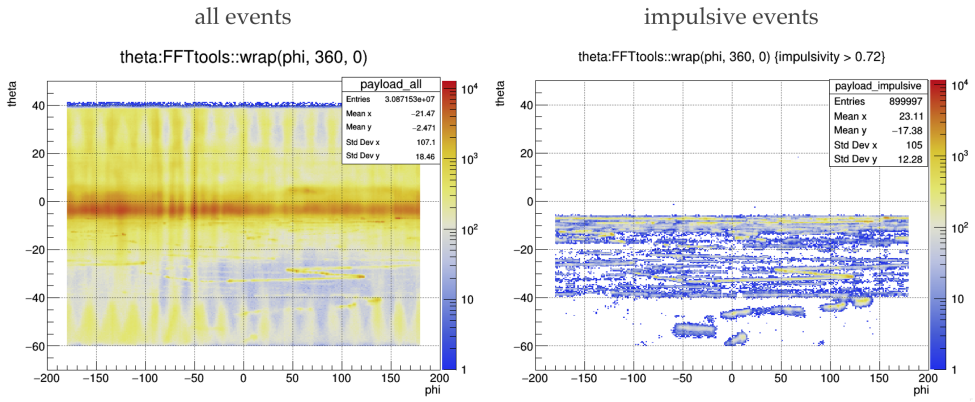

Figure 6.12: The 2D histogram of reconstructed events direction $(\theta, \phi - heading)$ in the local Earth coordinate. The left plot is all the thermal events passing quality cuts. The right plot is only the impulsive events passing the quality cuts and the thermal cut.

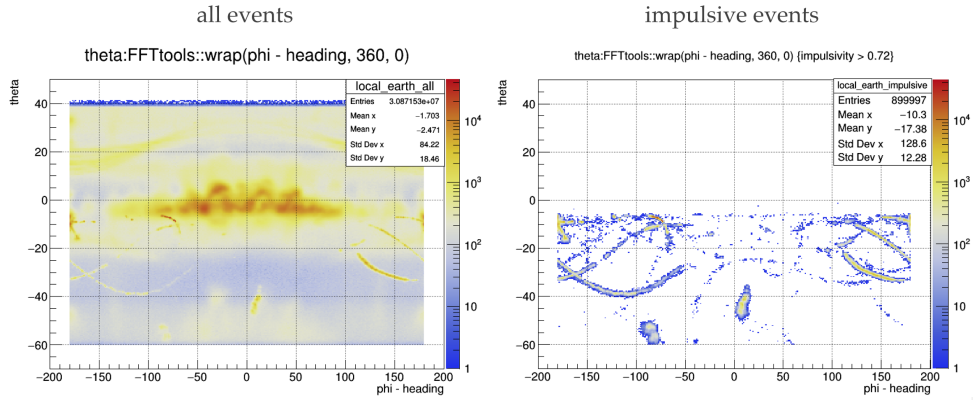

Figure 6.13: The 2D histogram of reconstructed events direction $(\theta, \phi - heading - longitude)$ in fixed Earth coordinate. The left plot is all the thermal events passing quality cuts. The right plot is only the impulsive events passing the quality cuts and the thermal cut.

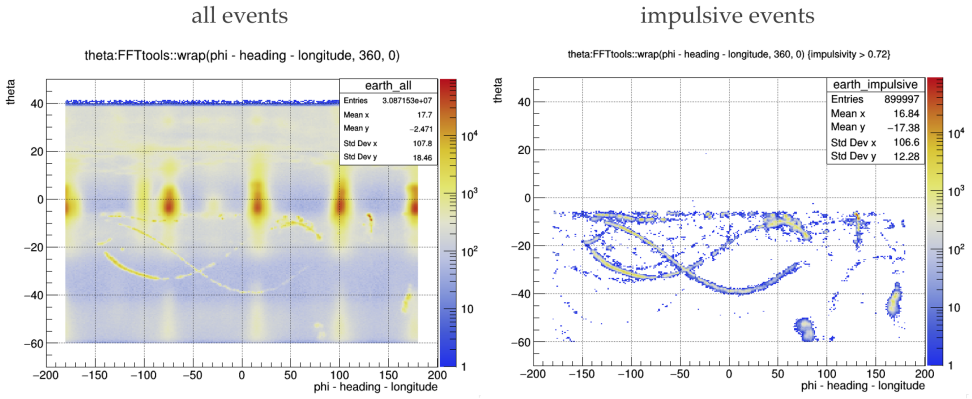

Figure 6.14: Plot of $(\phi - heading - longitude, day)$. The horizontal stripe is from the geosynchronous or geostationary satellite in the Y-axis is in the fixed Earth coordinate. The left plot is all the thermal events passing quality cuts. The horizontal yellow stripe denotes for the events directed from the satellites. The nearly vertical lines in the left plot are the events from the Sun. The right plot is only the impulsive events passing the quality cuts and the thermal cut. The lines in the plot are the traces from anthropogenic bases such as the WAIS and the South Pole station.

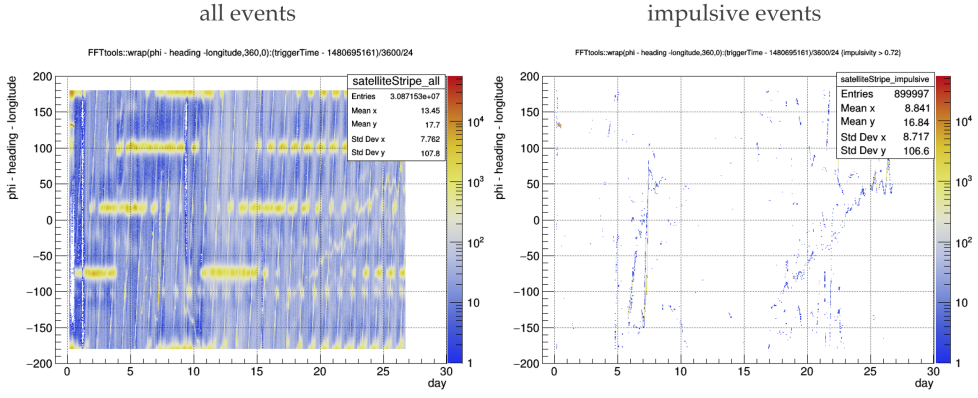

Figure 6.15: The 2D histogram of $d\phi$ vs SNR for all WAIS events except 45° runs. $d\phi$ is the angle difference between WAIS true ϕ and reconstructed ϕ.

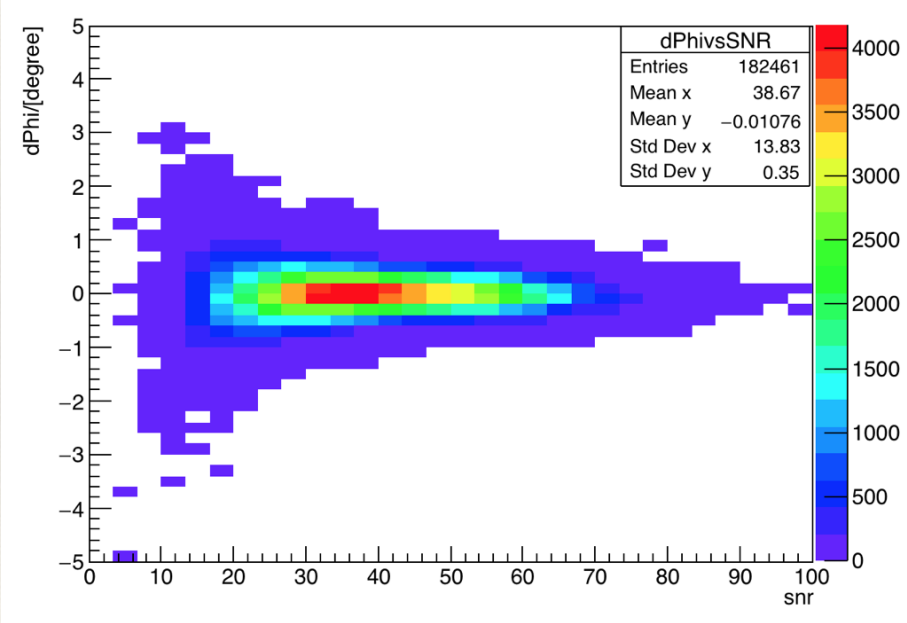

the surface will be indicated by not only the peak direction but also the contour of resolution.

6.5.1 Pointing Resolution Model

The pointing resolution is relevant to the SNR of the signal's CSW. The WAIS calibration events are used to determine a pointing resolution model. Here 45° WAIS runs are not included because its pointing is not well understood yet. In Figure 6.15 and 6.16, as SNR increases, the angular difference between WAIS's true direction and reconstructed direction, $d\phi$ and $d\theta$, tends to have a tighter distribution (smaller σ_θ and σ_ϕ). In each SNR slice, the angular distribution is considered to be a Gaussian distribution with resolution σ_ϕ in Figure 6.17 and resolution σ_ϕ in Figure 6.18. An ad-hoc functional form can be written to describe the relationship between the ordinate $y(=\sigma)$ and the abscissa $x(=SNR)$ in Figures 6.17 and 6.18 as follows: $y = c_1 x^{-c_2} + c_3$. This function is also generalized to give an estimated σ_θ and σ_ϕ for all impulsive events if we know the SNR of its DSW.

Figure 6.16: The 2D histogram of $d\theta$ vs SNR for all WAIS events except 45° runs. $d\theta$ is the angle difference between WAIS's true θ and reconstructed θ.

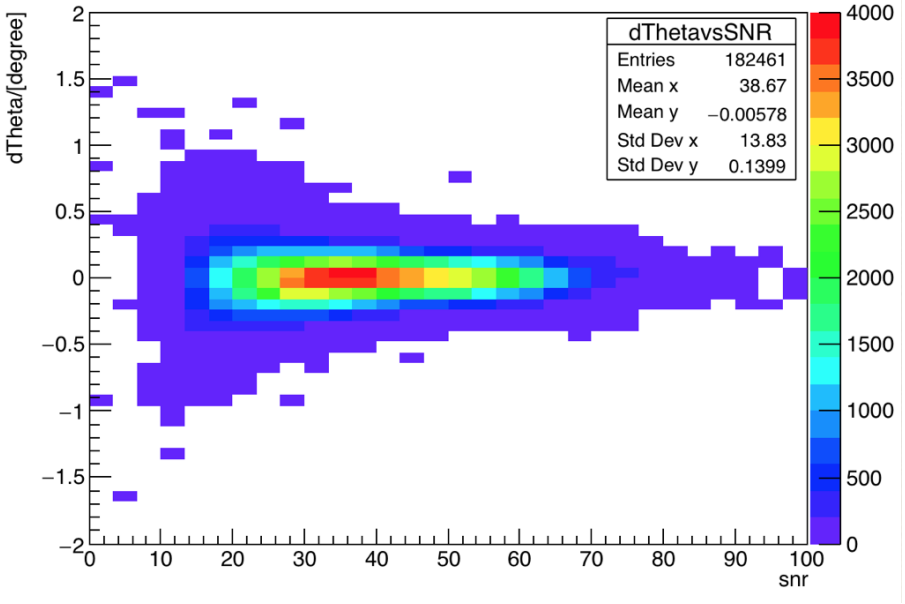

Figure 6.17: Fit σ_ϕ as a function of SNR. The fitting function is $y = c_1 x^{-c_2} + c_3$. The error bar on the vertex is a measure of how $d\phi$ different from a Gaussian distribution in a certain SNR range.

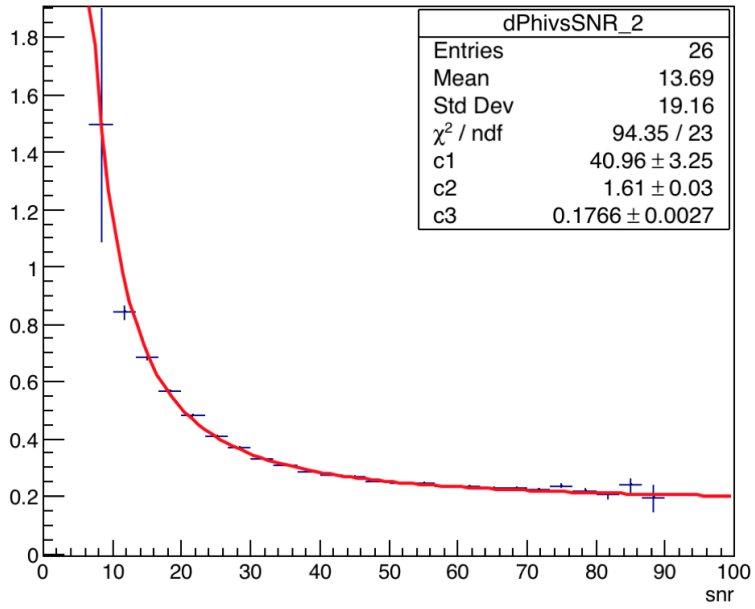

Figure 6.18: Fit σ_θ as a function of SNR. The fitting function is $y = c_1/x^{c_2} + c_3$. The error bar on the vertex is a measure of how $d\theta$ different from a Gaussian distribution in a certain SNR range.

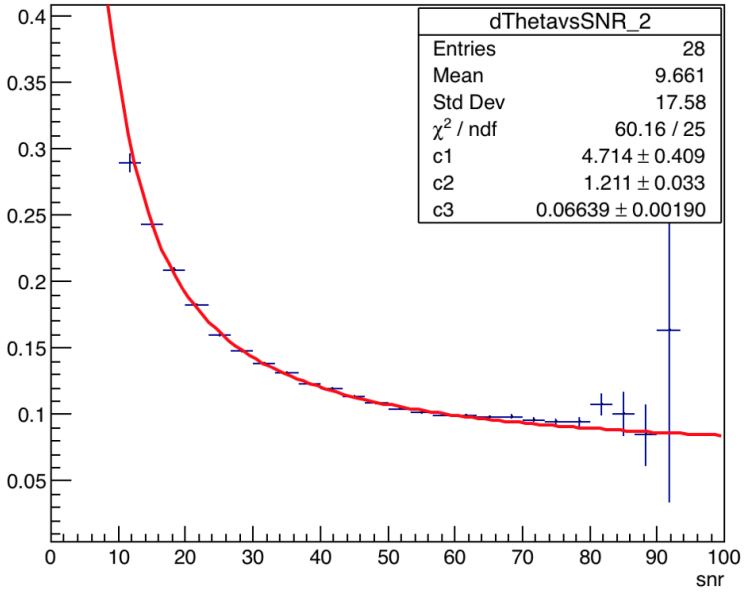

6.5.2 Probability Map

Each event that passes the quality cuts and theta cuts will be projected onto the Antarctica ice, given the reconstructed direction (θ, ϕ) and GPS information on the ANITA payload. However, the pointing resolution, which is determined by SNR, should differ from event to event. Also even if the pointing resolutions are all the same, when θ is near the horizon, a tiny angular change in θ would result in a large distance change in the projection. As we can see in Figure 6.19, when the payload is close to horizon, the projected contour can be very long along the direction from the ANITA payload to the event vertex. To solve this problem, it is better to treat the event projection not just as a single vertex on the ground but a Gaussian distribution centered at (θ, ϕ) with a $\lambda\sigma$ contour. The Gaussian distribution around the event's reconstruction peak direction should be also projected to the Antarctica ice. λ is a number larger than 0 and can be tuned to have the best experimental sensitivity.

The Gaussian distribution is a continuous probability density. To project it

Figure 6.19: The illustration of how the event distance to ANITA would affect the projected contour on the ground. For example, ANITA-IV recorded two events, A and B, where the green dots are reconstruction positions and the dark blue area is the 3σ contour. Those two events originate at different flight time from the same base, i.e. the blue dot at the intersection. For event B, when the payload is close to horizon, the projected contour can be very long along the direction from the ANITA payload to the event vertex and be relatively narrow in the perpendicular direction. The contour can also be above the horizon and cause a cut off the horizon as shown in the leftmost edge of the projected event B.

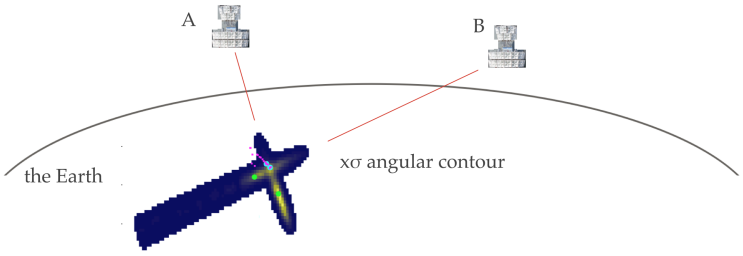

onto the ground, the whole of the Antarctica landmass should be segmented into bins. Within each bin, integrating the probability density leads to a Probability Sum (PS). All the bin's PS will sum close to 1 if this event's projected area is all below the horizon. It will not be precisely equal to 1 because the integration of the probability in each bin only has a finite number of samples. So the PS will be normalized to 1 after the projection. If the event is above the horizon or very close to the horizon so that part of its probability is above the horizon, then this event's PS will sum up to less than 1. Since we trust that the impulsive events cannot come from the sky due to the existence of the ionosphere, the PS will also be normalized to 1.

As in Figures 6.20 and 6.21, the Antarctica map is segmented into 1500×1500 bins for the range of [−3000 km, 3000 km] in East and [-3000 km, 3000 km] in North of a Stereographic map near the South Pole. So each bin has a size of 4 km×4 km.

The contour of the event projection is the union of two contours with different metrics. The first metric is the $\lambda\sigma$ contour from a 2D Gaussian Distribution. The second metric is the distance metric, which is just the distance between two events,

i.e. drawing a circle around the event with radius d. σ is determined by the event SNR so there are two cluster parameters, λ and d, which will be determined in a later section. As in Figure 6.20, two events with $\lambda = 2.5\sigma$ contour is projected to the ground. Moreover, they happen to overlap at the same base stations.

The probability map is a great way to show multiple pieces of information at the same time. For example, in Figure 6.21, the green dots are the events' reconstruction position. The dark blue area is the probability density within the $\lambda = 2.0\sigma$ contour. The payload path, bases, traverses, and planes are also shown on the map using different colors. With all this information, it is straightforward to cluster the events together and figure out whether the cluster is associated with any bases.

6.6 Event Clustering

6.6.1 Clustering Algorithm

Most of the events after the impulsivity cut are anthropogenic events and they tend to cluster together close to certain location. On the other hand, signal events due to UHE neutrinos or UHECR are more likely to occur at random places: such events would appear as isolated singlet events with no association to any known bases. A simple Breadth First Search algorithm can go through the bins in the map and find all the clusters. First, start with an unvisited bin with non-zero PS value, and then look for its neighbor bins. If all the neighbor bins are either visited or 0 then it forms a cluster. Otherwise, repeat this step for all the unvisited non-zero neighbor bins. All the visited bins with non-zero PS value form a cluster. The events with positions located in those bins belong to the same cluster. Second, repeatedly find the next unvisited bin with non-zero PS value to identify other clusters. The major part of the time complexity is projecting the events to the ice, because each event has its own probability distribution and doing the integration in each bin is likely to be time-consuming. However, its computation time is linear $O(n)$, where n is the number of events. As to the clustering, the time complexity is just $O(1)$, since the probability map has been built, the clustering algorithm only needs to iterate through the bins

Figure 6.20: Two events (green dots are the reconstruction positions) that happens to overlap at the same stations (the bright blue dots) from different payload directions. The region in dark blue and yellow is the $\lambda = 2.5\sigma$ contour of a Gaussian distribution. The purple dots are paths for the known traverses and airplanes. The red dots are the payload path. Each bin's size is 4 km $\times$ 4km. The coordinate is from a Stereographic map centered at the South Pole with meters as units

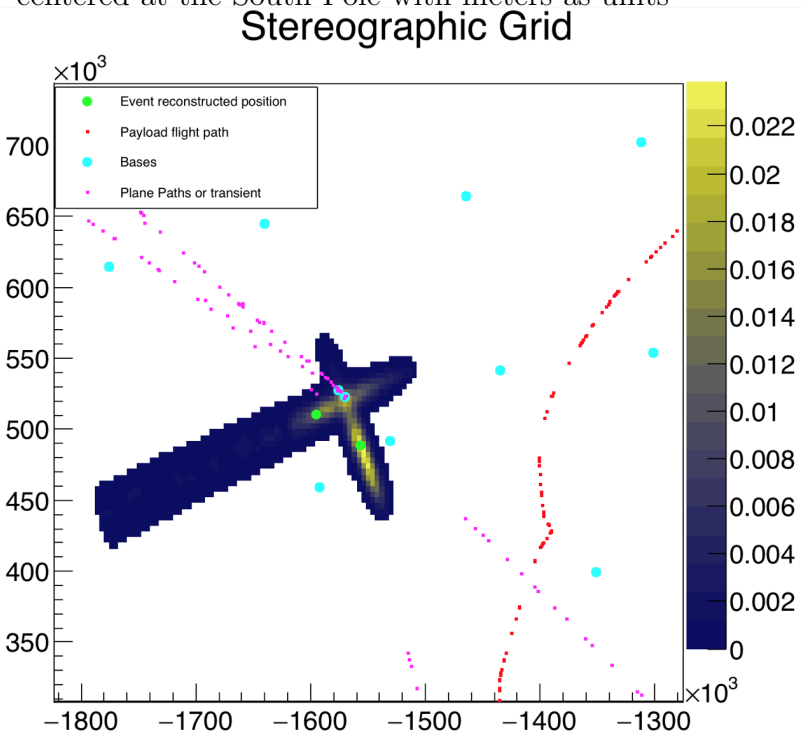

Figure 6.21: 10% events projected to Antarctica. The region in dark blue and yellow is the $\lambda = 2.5\sigma$ contour of the events' Gaussian distribution. The green dots are events reconstruction positions. The bright blue dots are the known bases. The purple dots are the traverses and planes. The red dots are the payload path. Each bin's size is 4 km $\times$ 4km. The coordinate is from a Stereographic map centered at the South Pole with meters as units. The color palette on top left denotes for the events density in arbitrary units. The color palette on the bottom left denotes for the ice thickness.

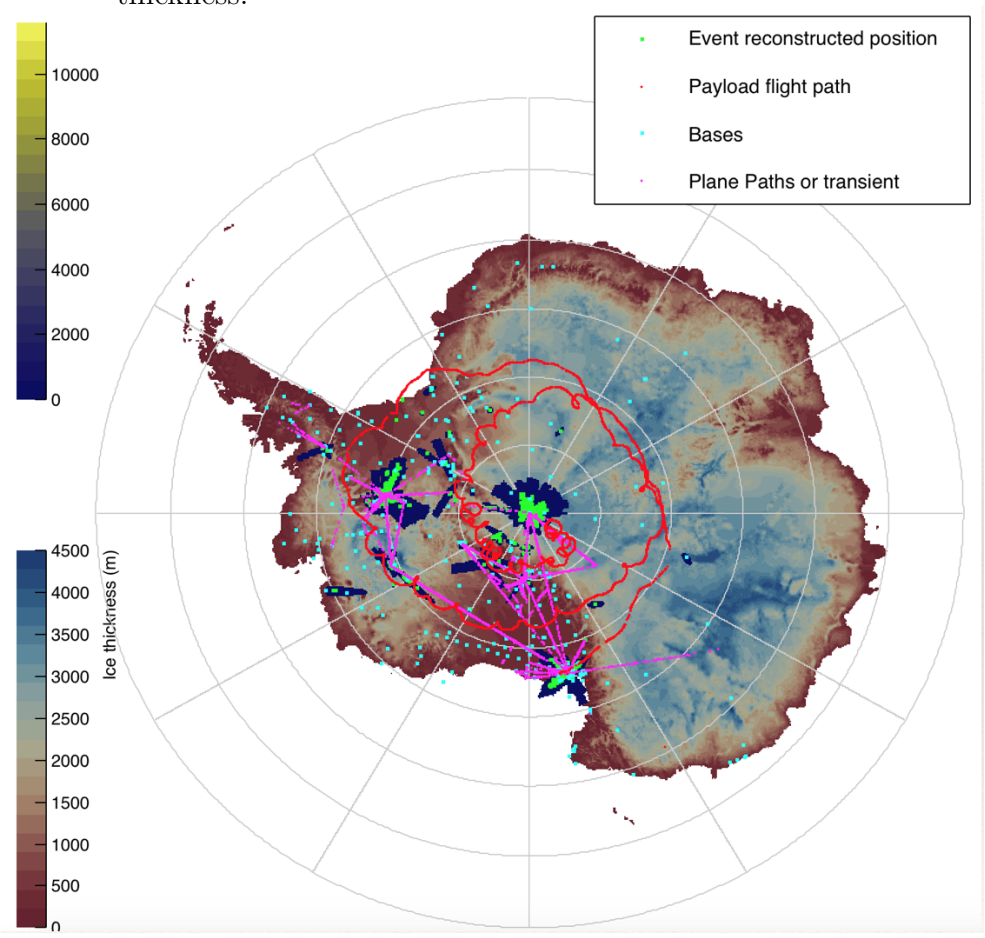

Figure 6.22: The clustering efficiency

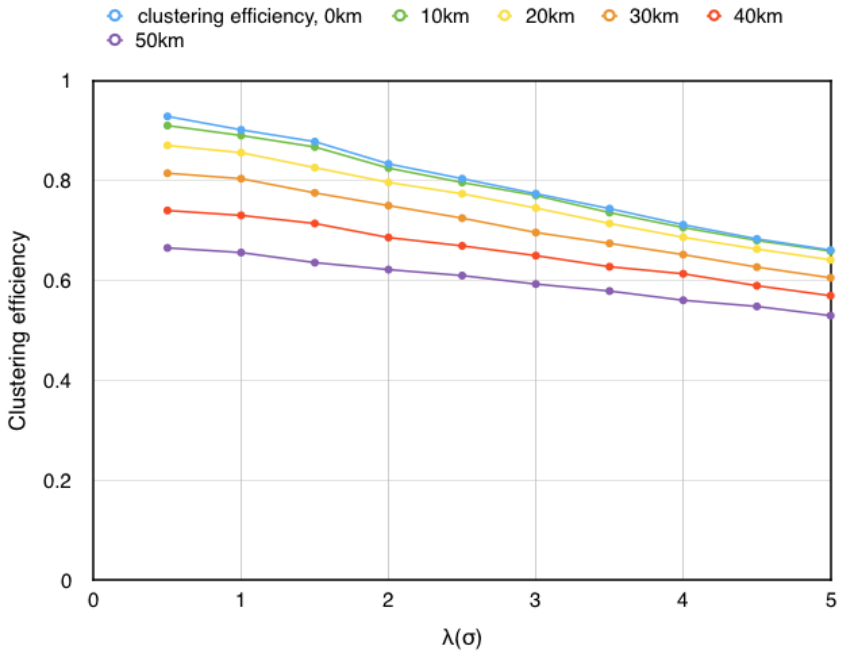

once to form all the clusters no matter how many events are projected. So the overall time complexity for projection and clustering is $O(n)$ comparing to $O(n^2)$, which is the traditional way of clustering events by pairs.

6.6.2 Clustering Efficiency

The clustering efficiency is the ratio of simulated MC neutrino events that can be found isolated from the bases and other anthropogenic clusters. The MC neutrinos are Monte Carlo simulated neutrino events generated by IceMC. Here we first project all events to the map, then remove the singlets from the map because they tend to be more like signal instead of an anthropogenic background. Finally, we project the MC neutrino events to the same event map one at a time and record the ratio of MC neutrino events that do not overlap with the event map to the total number of MC neutrino events. This ratio is the clustering efficiency of neutrino events. Figure 6.22 shows how the clustering efficiency changes with d and λ.

6.6.3 Background Estimate

The background events are the events that are not true signals but observed in our final signal region. It has two components: the thermal event background and the anthropogenic background. The anthropogenic background is the dominant background in the whole analysis. The clustering parameters, such as λ and d, determine the anthropogenic background estimation. The estimation of the backgrounds and their uncertainties is crucially important to our analysis. Though different clustering cuts can give different background estimations, it is not always better to lower the background because a very low background with very low signal efficiency is not acceptable. In other words, there is a trade-off between the signal efficiency and the background estimation. We want to ensure our ability to discover true signals but also want to ensure a low background. Considering this trade-off, we choose to minimize the neutrino flux limit to decide where we set the clustering cuts (more discussion in 6.6.4).

The thermal background is the number of thermal events which can pass our thermal cut. Usually, the thermal events are just noise and have very low *impulsivity*. However, since we have nearly two million thermal events, the statistical fluctuations can make some thermal noise events pass our cut and leak into our signal region.

To have an estimation of thermal background, we fit an exponential function to the thermal events' efficiency plot in Figure 6.23. Since the plot is on a log scale, the exponential fit is just a straight line. The exponential fit on the right-hand part of the tail of the efficiency plot in Figure 6.23 can be extrapolated beyond the cutoff near 0.74. To acquire a thermal background of 0.1, we find the corresponding λ value in the fitted exponential function, which is 0.752. In order to get the background uncertainty, the logarithm of the ratio between the original line and the fitted line is plotted as a histogram in Figure 6.24. The RMS value, 0.133, is the 1σ error in a logarithm scale. Then the upper bound is $0.1 \times 10^{0.133} = 0.136$ and the lower bound is $0.1 \times 10^{-0.133} = 0.07$. So the thermal background with 68% confidence interval is $0.1^{+0.04}_{-0.03}$.

Figure 6.23: The thermal efficiency vs. *impulsivity* cut and the exponential fit. To achieve a relative small background, we choose the thermal background to be 0.1. With extrapolation of the the exponential fit to tail, the corresponding the *impulsivity* cut is 0.752.

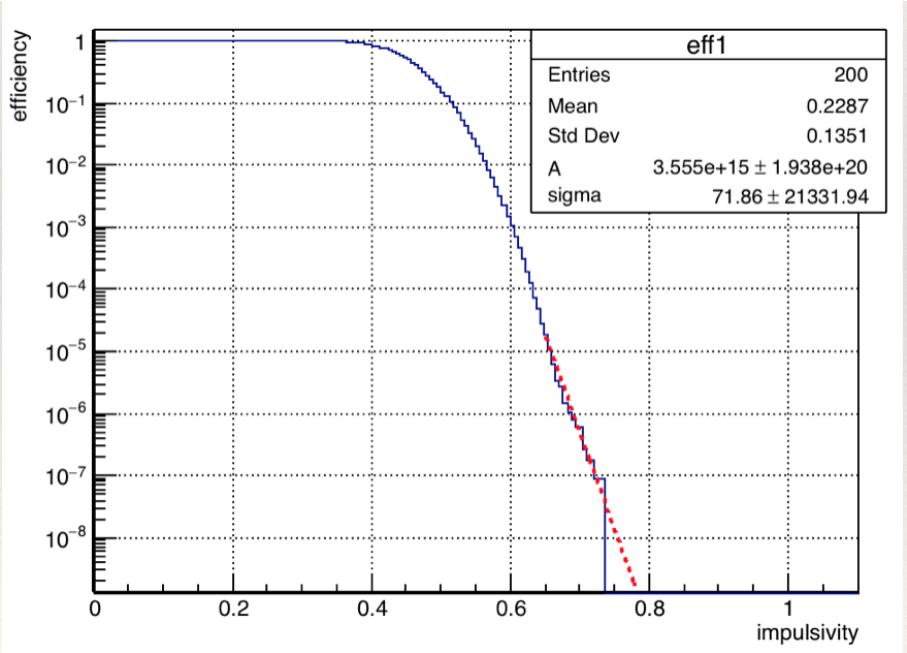

Figure 6.24: The error of the exponential fit. Since the order of magnitude of efficiency changes a lot, here a log scale of the error is shown.

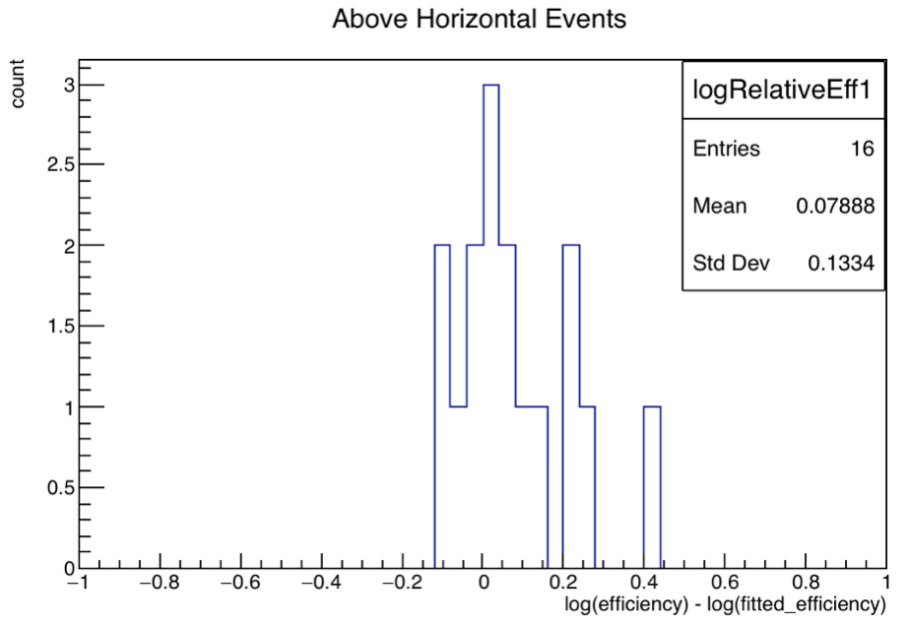

The second part of the background estimation is the anthropogenic background. In Antarctica, although the signals from human activity are quite limited to the known bases, there are still anthropogenic signals from some unknown bases. If multiple anthropogenic events come from the same place, then they can be clustered together and are regarded as an unknown base. If an anthropogenic event comes from an unknown base and does not cluster with other events, it is not possible to discriminate it from a real signal event and it will be treated as a background. As was mentioned above, neutrino or cosmic ray events tend to be singlets and since we do not expect hundreds of signals, the self-clustering of signals from UHE neutrino or UHECR events can be neglect. The anthropogenic background is estimated using an "ABCD" method as has been done in the data analysis of previous ANITA flights [83][4]. As shown in Table 6.2, the assumption is the distribution of ClusterSize for the event near the base is the same as the ClusterSize distribution of events not near any known base. The anthropogenic background estimated is 0.57. The background uncertainty is estimated by assuming the distribution of A (number of smaller clusters not from known base), B (number of smaller clusters from known base) and D (number of singlets from known base) are all Poisson distribution with λ equal to the measured value. Since $bg = A \times \frac{D}{B}$ we can get the distribution of background from the three Poisson distributions. Figure 6.25 shows the distribution of anthropogenic background taken from a numerical simulation. The final anthropogenic background with 1σ uncertainty is $0.57^{+0.93}_{-0.22}$.

6.6.4 Set Clustering Cut

As discussed in Section 6.5.2, every event can be projected as a combination of $\lambda\sigma$ angular contour and $d/2$ km radius contour. This combined contour is all the information we need to do a clustering analysis, i.e. whether events can be clustered or not. Those λ and d are the clustering cut parameters and the choice of those clustering parameters should be done in an unbiased way. Here we want to set those clustering parameters by optimizing the final flux limit of neutrinos. The flux upper limit f

Table 6.2: The ABCD table when $\lambda = 3\sigma$ and d=0 km. ClusterSize is the number of events in the cluster. When the ClusterSize is 1, it is a singlet cluster. When the ClusterSize is between 2 and 5, it is the so-called small clusters. The assumption is the distribution of ClusterSize for events near base and events not near any base is similar. So we can use $bg = A \times \frac{D}{B}$ to estimate the anthropogenic background. For example, from the current table, the anthropogenic background in box C is $2 \times /7 = 0.57$

ClusterSize	noBase	nearBase
1<n<6	A=2	B=7
1	C blinded	D=2

Figure 6.25: The distribution of anthropogenic background. It is simulated with assumption that A, B and D all follow Poisson distribution

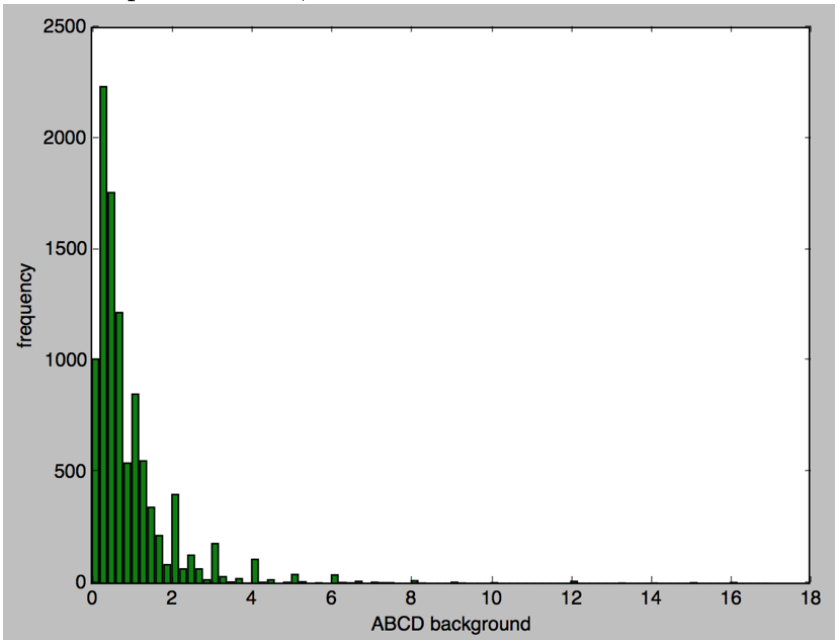

follows:

$$f = E_\nu \frac{dN_\nu}{dE_\nu} = \frac{N_{90}}{A_\Omega T \varepsilon \Delta} \tag{6.2}$$

where N_{90} is the Feldman-Cousin sensitivity with the expected background. A_Ω is the ANITA-IV acceptance, which is calculated from IceMC simulation and includes all the effects such as the ice thickness and the trigger efficiency. $T = 27.3$ days is the live time of ANITA-IV. $\Delta = 4$ is a constant factor independent of model [84]. ε is the analysis efficiency: it is related to the product of the efficiency of the quality cut ε_q and the efficiency of clustering cut ε_c :

$$\varepsilon = \varepsilon_q \varepsilon_c \tag{6.3}$$

So the neutrino flux upper limit can be rewritten as:

$$f(\lambda, d) = \frac{N_{90}(\lambda, d)}{A_\Omega T \varepsilon(\lambda, d)} = \frac{1}{A_\Omega T \varepsilon_q} \times \frac{N_{90}(\lambda, d)}{\varepsilon_c(\lambda, d)} \tag{6.4}$$

So only N_{90} and ε_c are a function of clustering parameters. By varying λ and d we can get different flux upper limits. When the flux upper limit reaches a minimum, we have the best λ, d values. Figure 6.26 shows how the anthropogenic background changes with different settings of λ and d. The total background is the sum of thermal background and anthropogenic background. For each value of total background, the sensitivity of the experiment is the upper limit of the signal given no events observed [85]. Figure 6.27 shows how the Feldman-Cousin sensitivity changes with different settings of λ and d. The next step is to calculate a flux upper limit that is proportional to the FC-sensitivity in Figure 6.27 and in inverse proportion to clustering efficiency in Figure 6.22. From Figure 6.28 the flux limit reaches a minimum when $\lambda = 3.0$ and d = 0 km. Other setting such as $\lambda = 3.0$ and d = 10 km or $\lambda = 4.0$ and d = 0 km have a little less but similar flux upper limit. It probably means there is no such thing as a "best" setting to the clustering. The λ and d are not independent so multiple ways of setting λ and d can both work for our analysis. However, we finally choose $\lambda = 3.0$ and d = 0 km and it has 0.67 background for the combined polarization. The uncertainty of

Figure 6.26: The anthropogenic background is a function of λ and d (the clustering cur parameters). This obvious because λ and d can directly affect the clustering of events. Then using the ABCD method, we will get different anthropogenic background estimations. Here each line is with a fixed d and it represents the relation between the anthropogenic background and λ. As λ and d increase, the estimated anthropogenic background tends to decrease and the clustering efficiency will decrease. So the balance between a low anthropogenic background and high clustering efficiency is the main concern when optimizing those clustering parameters (λ and d).

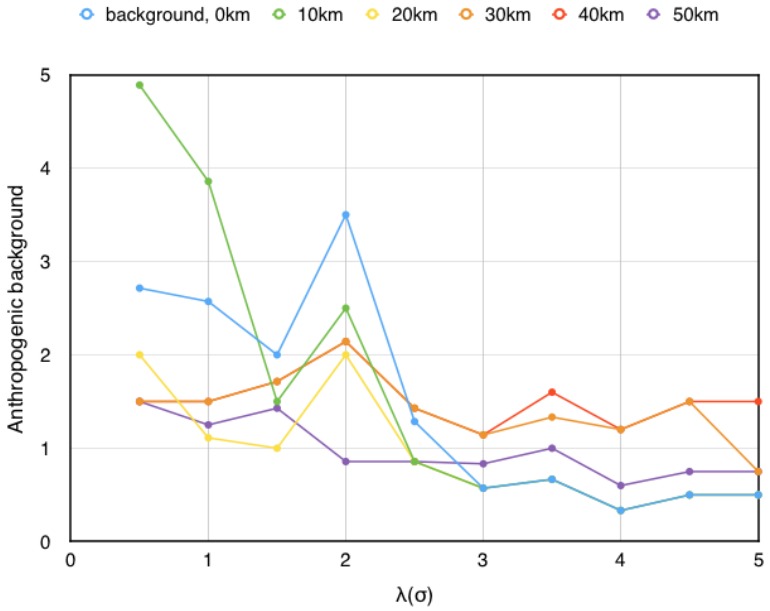

anthropogenic background can be obtained in Figure 6.25 and the clustering efficiency (78.2%) can be obtained from Figure 6.22. The total analysis efficiency (70.7%) are multiplication of quality cut efficiency (91.8%), thermal cut efficiency (98.5%) and clustering efficiency (78.2%).

In summary, the thermal cut and clustering cut gives a thermal background of $0.1^{+0.04}_{-0.03}$ and an anthropogenic background of $0.58^{+0.94}_{-0.22}$ for the combined two polarizations. The total background is $0.68^{+0.94}_{-0.22}$. Here the backgrounds sum together while the uncertainties sum quadratically. The number of HPol events and VPol events for

Figure 6.27: Feldman-Cousin sensitivity is the upper limit of the number of signal given 0 observed events and certain background in Figure 6.26. Currently we use N_{90} which has 90% confidence interval. Here each line is a plot of N_{90} vs λ with a fixed d.

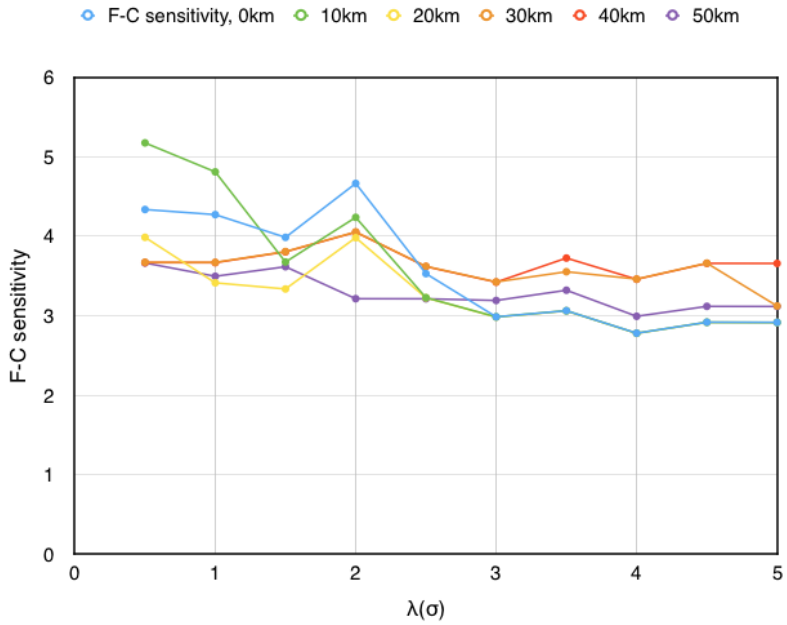

Figure 6.28: The neutrino flux upper limit in arbitrary units. The limit is calculated by N_{90} in Figure 6.27 and divided by ε_c in 6.22 Here each line is a plot of the anthropogenic background vs λ with a fixed d.

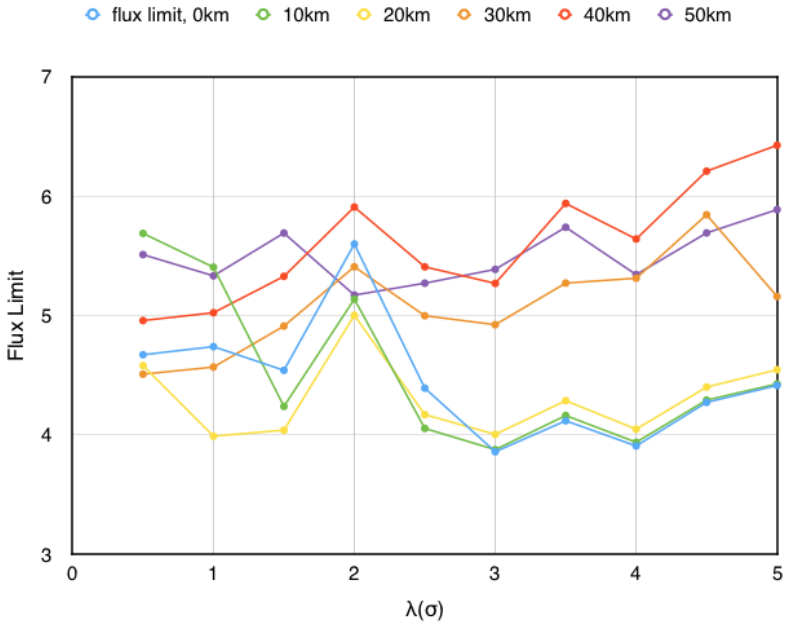

small anthropogenic clusters is 23 and 25. So there is no indication of any significant asymmetry between the two polarizations. Here we assume that there exists an equal background expectation in HPol and VPol such that the background of each polarization is $0.34^{+0.66}_{-0.16}$.

6.7 IceMC Simulation

IceMC is a Monte Carlo simulation program to simulate the UHE neutrino interactions for the ANITA experiments. This tool is written in C++ based on the ROOT data environment. IceMC combines information of ANITA payload status (location and system response), the ice thickness in Antarctica, the interaction rate of UHE neutrinos and the ray tracing of Askaryan radiation. It can provide the most accurate acceptance for ANITA for calculating the final flux limit. It also provides the simulated signal waveform with a synthetic impulsive signal in real background noise. The background noise is selected from the ANITA-III Min-Biased events (which are

Figure 6.29: IceMc program flow chart. Plot by Linda.

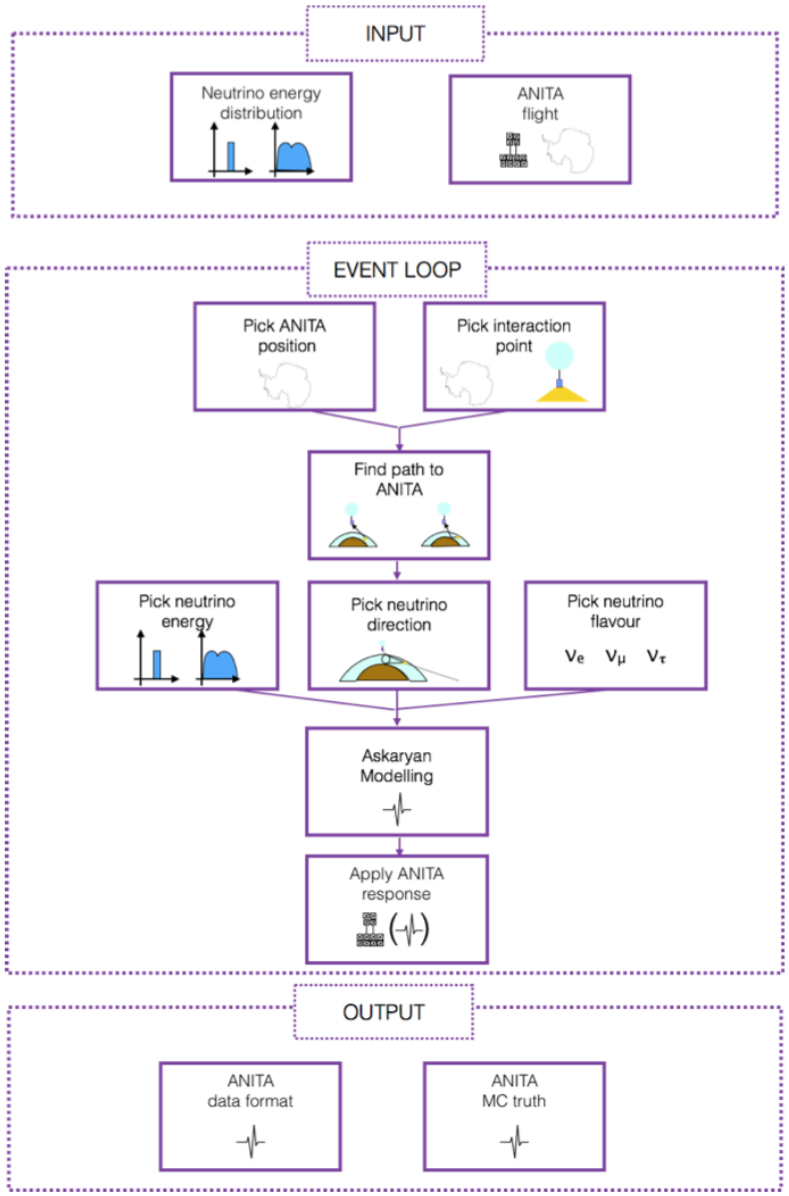

the software triggered events during quiet runs from 204 - 250). The output will be the ROOT data file in the same data structure with real flight data. The flow chart of IceMC program is shown in Figure 6.29. The neutrino spectrum model, such as Kotera Max model [3], and the ANITA flight information is in the configuration of the program. In the first step, the neutrino events with all flavors are generated in random directions, considering the weights from attenuation length, and interact with matter at random positions in the ice. The energy and flavor of the neutrino are all randomly selected from the model. In the second step, the Askaryan signal is produced and propagates in the ice and air to ANITA payloads. All possibilities in the first two steps are combined in the final weights of the event. The third step is adding system response and background noise to the signal. Moreover, the final waveforms will be stored into the ROOT data file, which is the common data format for real ANITA events. The additional information about the energy, direction, weight of the neutrino event are stored in SimulatedAnitaTruthFileX.root, where X represents the run number.

Chapter 7

RESULTS AND CONCLUSIONS

After the data analysis in Chapter 6, the estimated background is $0.34^{+0.66}_{-0.16}$ for each polarization, with the assumption of an equal amount of VPol and HPol background. The total analysis efficiency is 70.7%. This Chapter focuses on unblinding, i.e. open the signal box, and summarizes the results. The signal box, so-called signal region, are the impulsive events not near any known bases or clustered with other events. Section 7.1 defines the polarization and polarity and reviews their importance in event classification. Section 7.2 discusses the result of box opening in both HPol and VPol. Section 7.3 calculates the neutrino flux upper limit. Section 7.4 summarizes the results from my analysis. Section 7.5 discusses the future of ANITA mission, ANITA-V.

7.1 Polarization and Polarity

As described in Section 1.5.5, if the electric field $\boldsymbol{E}$ detected by ANITA has a vertical orientation, that event could be a neutrino candidate, but if $\boldsymbol{E}$ is horizontal the event would be a cosmic ray candidate. The polarity of CR events changes if the event is reflected or direct. Here the definition of polarization and polarity are discussed in detail. The polarization is defined as (see Section 6.1) the product of its impulsivity and the peak value in the interferometric map. The polarity is the sign of the electric field or the CSW. The polarity is more interesting in CR events because they could be direct or reflected events, where the polarity are opposite. Though there is no absolute polarity, in this analysis the polarity is defined such that a reflected CR event has polarity +1, and a direct CR event has polarity -1. The relation between polarity and elevation angle for CR candidates is an important component in the analysis. Since ANITA does not have a simulation of CR events, the polarity of CRs can be determined by

the cross-correlation value of CSW between it and other CR candidates after opening the signal box. A CR template can be further made by averaging among all the CSW of CR candidates by flipping the waveform of events with negative polarity. The CR template is used as a visual check on the quality of the waveforms. The polarity used in this work is due to Peter Gorham.

7.2 Open the Signal Box

In order to do an unbiased search, one is required to be blinded to the signal region during all analysis in Chapter 6. So the results of events in the signal region will not affect our decision of thermal cut and clustering. Once all the cuts are fixed, and the background is estimated, one is allowed, for the first time, to see the signal region that is the singlets not from any known base. 24 HPol events and one VPol event were found. Table 7.1 lists these events index, event number, polarization and polarity. A summary of the events reconstruction for these 25 events can be found in the Appendix.

7.2.1 HPol Cosmic Ray Candidates

The 24 horizontally polarized isolated events not from any known bases are EAS cosmic ray candidates. Figure 7.1 plots the positions of all the 24 EAS events on the Antarctica ice-depth map, with green crosses representing the shower vertex on the ice and the red crosses representing the payload position. Indexed event numbers are labeled in the map to establish the relation between event position and payload position. Meanwhile, all the known bases near the flight path are light blue dots. All the known air-plane paths are purple dots. There are also 0.7 million green dots representing the reconstructed positions of impulsive events, with their 3σ contours painted in dark blue.

One of the 24 events, event 35963950, is identified as background event because its deconvolved summed waveform is quite noisy and its linear polarization fraction is quite low compared to other events, as shown in Figure 7.2. The poor quality of

Table 7.1: After opening the signal box, we find 24 HPol events and one VPol event. Events 35963950, 17904564, 72164985 and 69261214 are discussed in the text.

Index	event#	polariztion	polarity	detail
0	12131787	H	+1	
1	15738420	H	+1	
2	16821419	H	+1	
3	17904564	H	+1	off from geomagnetic polarization expectation
4	20936205	H	+1	
5	25580797	H	+1	
6	25855454	H	+1	
7	45684620	H	+1	
8	35963950	H	NA	waveform not like CR, notch 460 is on
9	36785931	H	+1	notch 460 is on
10	39236841	H	+1	
11	40172984	H	+1	
12	47396999	H	+1	
13	54063721	H	+1	
14	64472798	H	+1	
15	64859493	H	+1	
16	64861754	H	+1	
17	66509677	H	+1	
18	72164985	H	-1	near horizon
19	83074427	H	+1	
20	88992443	H	+1	
21	91525988	H	+1	
22	93744271	H	+1	
23	95576190	H	+1	
24	69261214	V	+1	close to another Vpol event

Figure 7.1: This shows the position of all 24 HPol events in the signal box. The green crosses are events' projected position, and the red crosses are the corresponding payload position. The dark blue regions denote the 3σ contour for all events. The green dots represent 700 thousand events projected position on the map. The blue dots are the known bases, and the purple dots are the known planes. The red path is the ANITA-IV payload flight path.

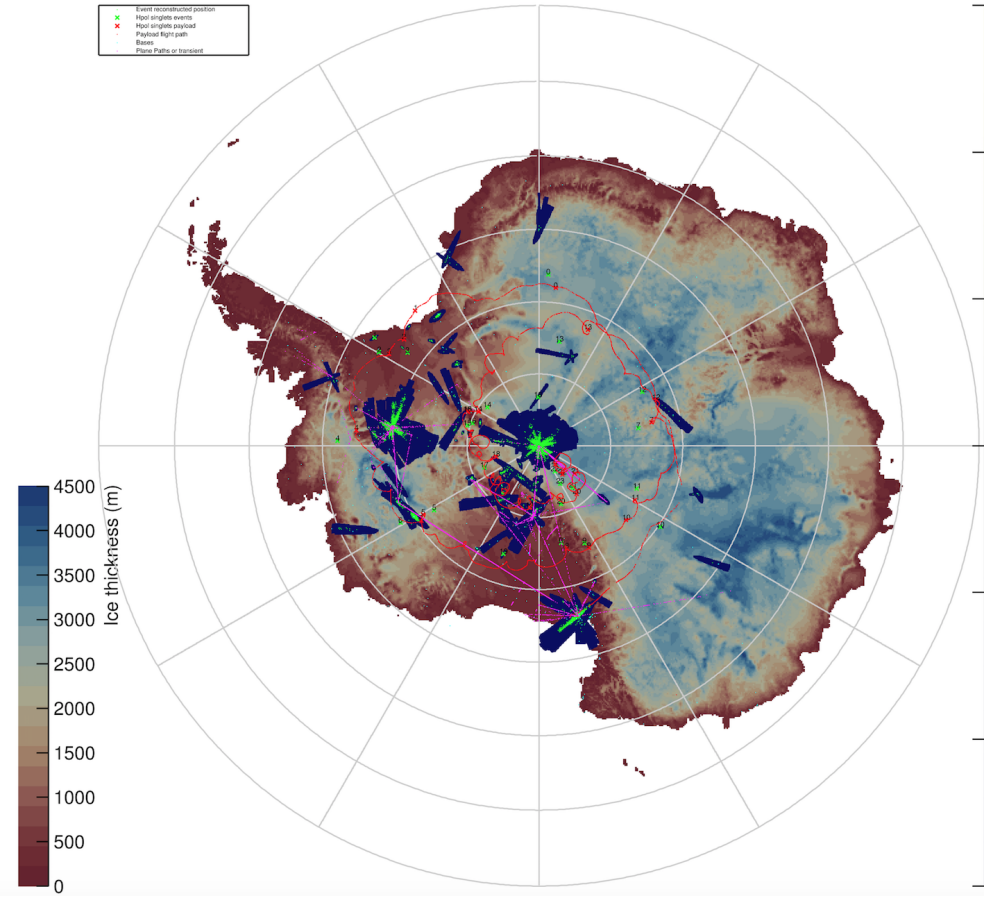

Figure 7.2: The Linear Polarization Fraction histogram for the 24 CR candidates. Events 35963950 and 17904564 are outliers from the other CR candidates.

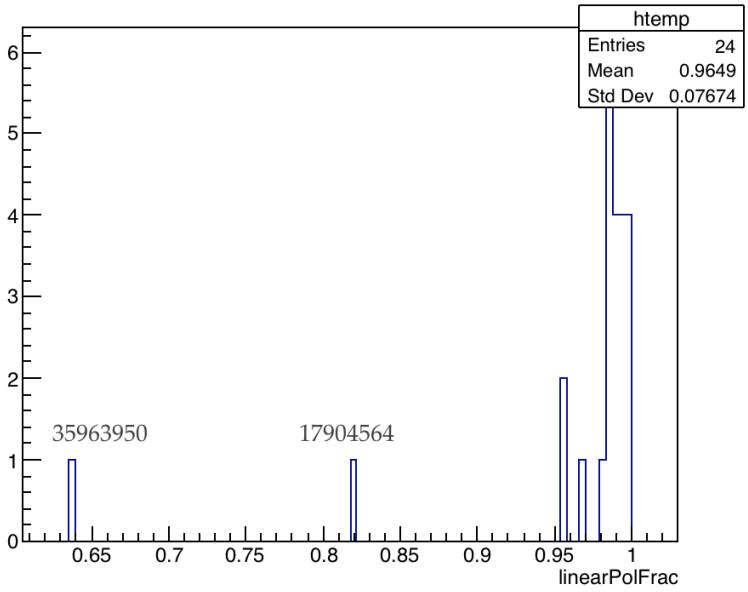

the waveform could be partly due to the notch filter at 460 MHz, which is discussed previously in Section 2.3.2. The next event, 36785931, is also affected by notch 460. But its waveform has better quality and is kept in the CR candidates.

Another event, 17904564, is also recognized as background because, as in Figure 7.3, it is 5σ off from the expected polarization angle. All the other 22 HPol events are consistent with the geomagnetic prediction. A sub-threshold analysis near event 17904564 did not find any nearby similar events. Its linear polarization fraction is also significantly less than the other 22 events. However, we can not explain why its waveform is similar to CR events. Event 17904564 directs to Ronne Ice Shelf, which has 483m of ice on the top of the 420 m deep of sea water. It also has a relatively equal amount of power in horizontal and vertical. Further investigation is necessary, and we can not declare this event as a CR event based on current knowledge.

Of the remaining 22 events, 21 have +1 polarity, but event 72164985 has -1 polarity. As discussed in Section 1.5.4, -1 polarity usually means a direct CR event and +1 polarity mean a reflected CR event. Event 72164985's elevation angle is $-6.17°$ and it local horizon elevation is $-6.02°$. At $0.15°$ below the horizon, with a $1\sigma_\theta = 0.12°$

pointing resolution in elevation, the uncertainty of the pointing allows a direct event hypothesis.

The other 21 CR candidates all look consistent with the current CR model. So in total, we have 22 good CR events and two background event. The two additional black dots in Figure 7.3 are from a post-unblinding result with an extended elevation range from below horizon to below horizontal. These two events have -1 polarity, correct for direct events, and are consistent with their expected geomagnetic polarization angles. If we include them in the CR list, there are 24 good CR events, where 21 events are reflected, and 3 events are direct, and 2 background events. Figure 7.4 shows the polarity and elevation angle for the 24 good CR events. The step change of polarity at $\theta \approx -6.3^\circ$ can be explained by the reflection on the ice.

In previous ANITA flights, two anomalous CR events, also known as the unusual upward-going cosmic-ray-like events, were observed in ANITA-I and ANITA-III [86]. The waveforms for these events looks like a direct CR event, but their reconstructioned elevation angles are very steep from the ice (-27.4°, -35.0°). No such anomalous events are observed in ANITA-IV.

7.2.2 VPol Neutrino Candidates

One VPol neutrino candidate, event 69261214, was observed . Its polarization angle is 87.8°, and its Linear Polarization Fraction is 0.95. It is a vertically linear polarized event, with elevation angle -13.5°, and ice depth 1686 m. The elevation angle and ice depth are consistent with Askaryan radiation from an UHE neutrino-induced shower. Figure 7.5 shows its reconstruction and coherently summed waveforms. The interferometric map indicates a strong plane-wave in vertical polarization. The deconvolved summed waveform also displays a strong impulse signal along the reconstructed direction.

Figure 7.6 shows the reconstructed position of this event. Because it is a signal event, it must be a singlet not clustering with any other events. However, it is physically close to some other events. For example, event 65532804 is only 17 km away from the

Figure 7.3: The measured polarization angle vs. the expected polarization angle. The red, orange and blue dots are the 23 CR events except the background event 35963950. The red dot, event 72164985, is a near horizon event, which could come from above horizon. The orange dot, event 17904564, has polarization angle inconsistent with expectation. The blue dots represent 21 high-confidence CR candidates. The two black dots are above horizon events originally from an independent analysis at the University of Chicago by Andrew Ludwig. They could appear in the present analysis if the elevation cut angle θ was moved from below horizon ($\approx -6^\circ$) to below horizontal (0°).

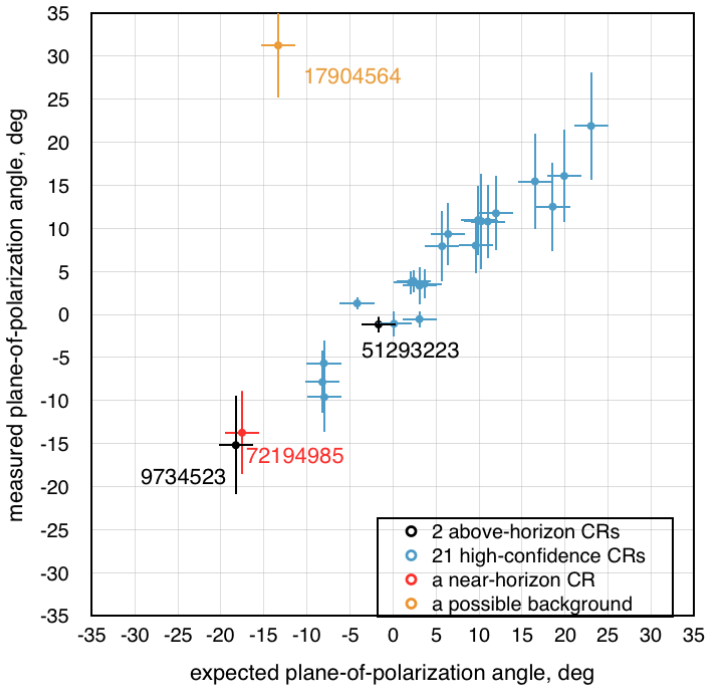

Figure 7.4: Polarity vs elevation angle for 22 good CR and 2 additional above horizon events. Polarity of +1/-1 indicates reflected/direct CR geometry.

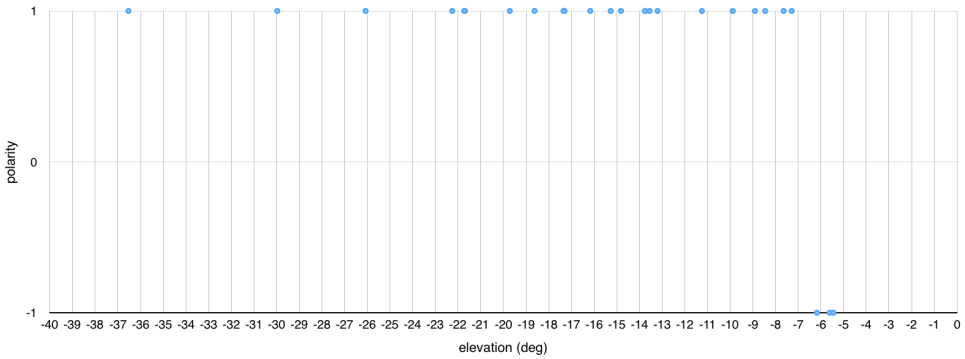

Figure 7.5: The reconstruction results of event 69261214. The interferometric map, deconvolved summed waveform in time domain and frequency domain are shown for each polarization. The interferometric map of VPol has a bright spot representing the most likely direction of the signal. The interferometric map of HPol is consistent with a thermal background. In the DSW of VPol, the waveform shows an impulsive signal.

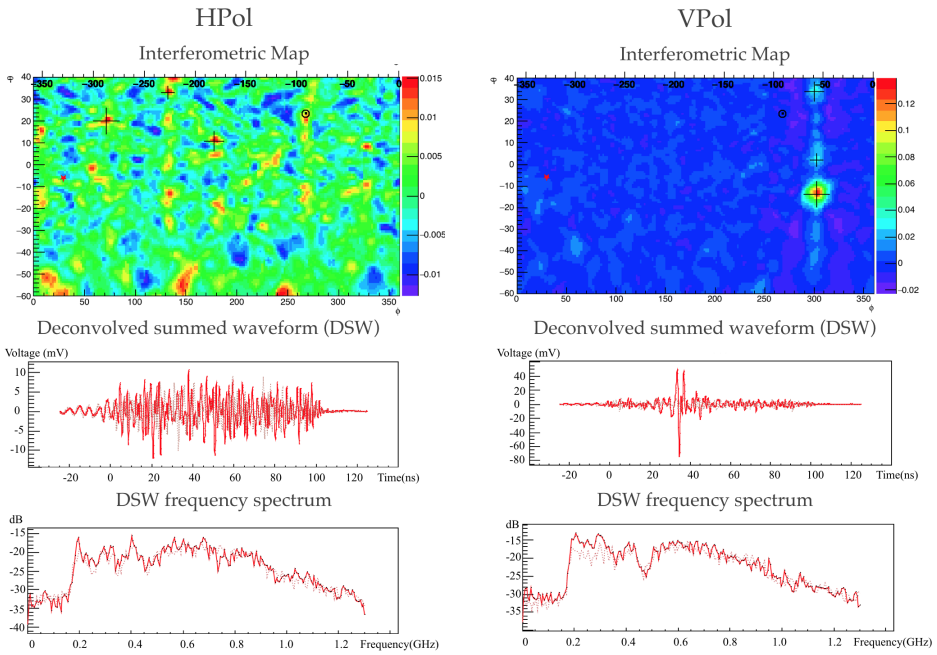

Figure 7.6: The location of event 69261214 in west Antarctica. The green cross represents the reconstructed position of events on the ice. The red cross represents the payload position when the event was triggered. Light blue dots are the known bases and the purple dots are airplane flight paths. The red dots are the ANITA-IV payload path.

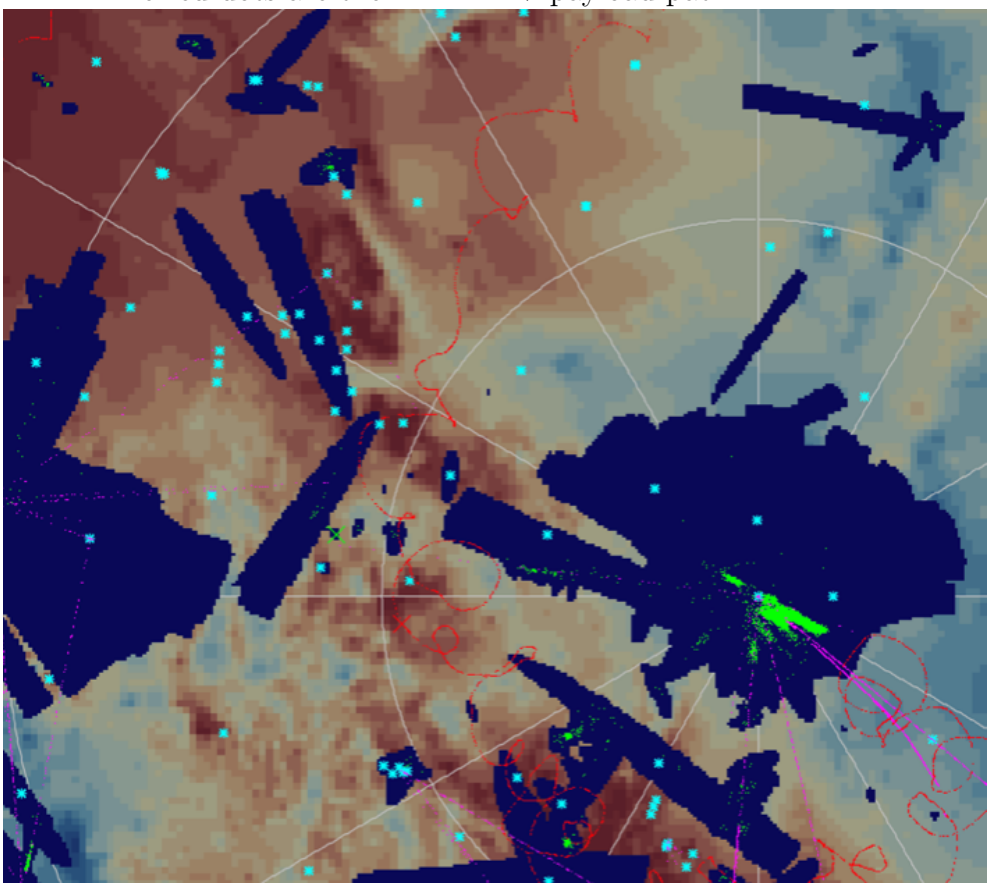

candidate event, although their deconvolved summed waveforms do not show a strong correlation. Another small cluster containing three events is within 45 km from the candidate. If we use a larger distance metric to cluster the events, this candidate event will merge into other clusters and never get into the signal region. If we keep our current clustering method and use a looser thermal cut threshold, event 69261214 is still quite isolated and not clustering with any other nearby events.

There is also one neutrino candidate in each of ANITA-II and ANITA-III flights, Figure 7.7 shows the background, deconvolved summed waveform and interferometric map for VPol candidates of the three ANITA flights. Although the background decreases in the ANITA-IV, the one observed event relative to the background and its uncertainty is not significant enough to claim a discovery. The polarity of the ANITA-IV candidate seems opposite from the previous two flight's candidates (all three events are just candidates, no guarantee of a real UHE neutrino event).

With all the facts mentioned above, we have one VPol candidate in ANITA-IV at the background of 0.34. However, the evidence is not significant enough to make the claim of an UHE neutrino observation. We can only give a neutrino flux upper limit in Section 7.3.

7.3 Neutrino Flux Limit

The neutrino flux upper limit can be calculated with formula 6.2

$$f = E_\nu \frac{dN_\nu}{dE_\nu} = \frac{N_{90}}{A_\Omega T \varepsilon \Delta} \tag{7.1}$$

in Section 6.6.3. Given 1 event observed and 0.34 background in the vertical polarization, the sensitivity with 90% confidence interval N_{90} [85] is 4.02. The total analysis efficiency ε is 70.7% averaged from the KAO "Max" model. The live time T of ANITA-IV is 27.3 days. The ANITA-IV acceptance A_Ω is simulated by IceMC:

$$A_\Omega = 4\pi\varepsilon_t \frac{V_{ice}}{L_{int}} \tag{7.2}$$

where 4π is the solid angle of the whole sky, ε_t is trigger efficiency of MC simulated neutrino events and L_{int} is the neutrino attenuation length based on the Standard Model.

Figure 7.7: Comparing analysis exposure (at $10^{20}eV$), background, deconvolved summed waveform and interferometric map for VPol candidates from ANITA-II to ANITA-IV. The polarity of the candidate in ANITA-IV seems opposite to the previous two flights. The background estimation improved in ANITA-IV due to improvements of cuts, clustering, filter and trigger.

	ANITA2	ANITA3	ANITA4
Analysis Exposure AΩTε [m^2 sr s]	1.21E+07	1.79E+07	3.03E+07
# Vpol Candidate	1	1	1
Event Number	16014510	83139414	69261214
Expected Background	$0.97^{+0.42}_{-0.42}$	$0.7^{+0.5}_{-0.3}$	$0.34^{+0.49}_{-0.26}$
deconvolved summed waveform	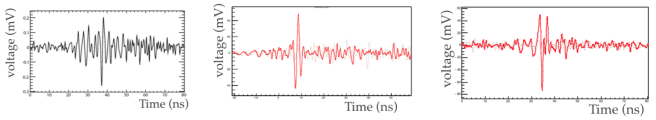		
interferemetric map	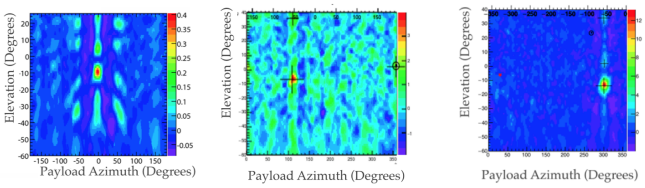		

Figure 7.8: The neutrino flux limit in ANITA-IV compared with prior ANITA flights and the latest data from Auger[25] and IceCube [26]. Predicted neutrino flux from Kotera, Allard and Olinto (KAO) [9] and from Ahlers and Halzen (AH) [27] are also compared. The plot is generated using a script from Linda Cremonesi.

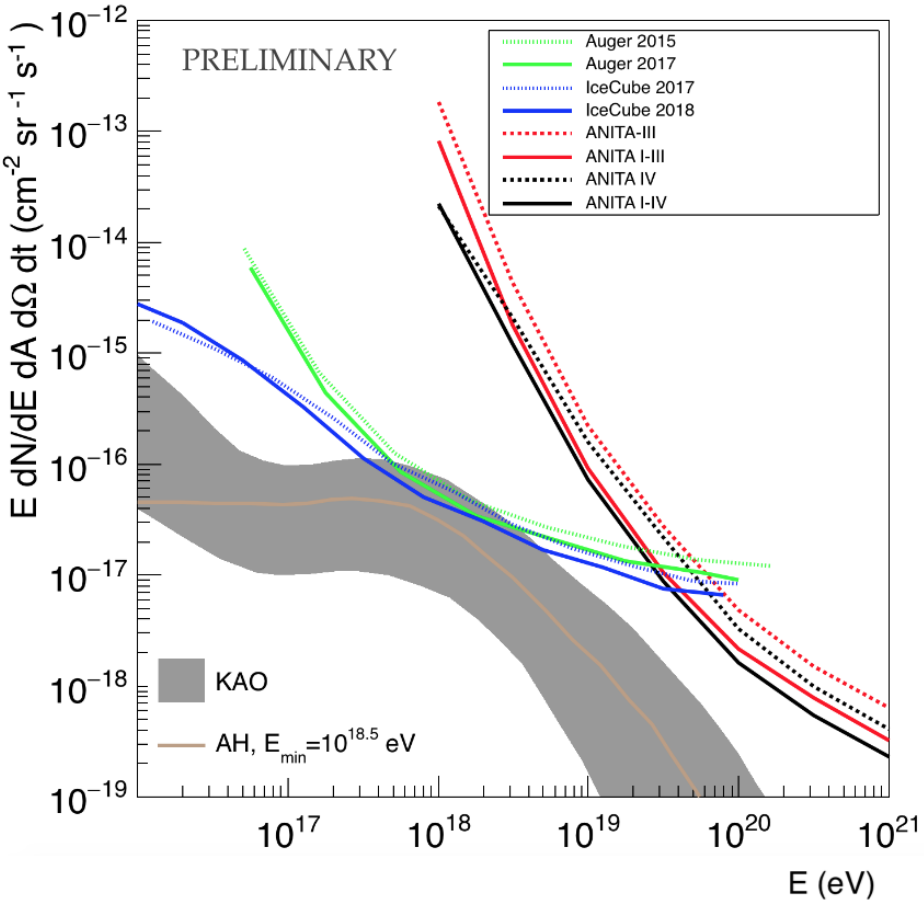

V_{ice} is the volume of ice seen by ANITA as modeled in IceMC. The simulation is still being refined to include all flight information. Moreover, the results for ANITA-IV do not include the parallel analysis by Andrew Ludwig at University of Chicago. Finally, previous analysis of ANITA I-III data used a value of $N_{90} = 2.3$, and the collaboration has not adopted a uniform standard for presentation of limits. Accordingly, the results in Figure 7.8 are marked "PRELIMINARY".

7.4 Summary

HPol signal region unblinding gives 24 CR candidates on a background of $0.34^{+0.66}_{-0.16}$, where 21 events are identified as reflected CR events, 1 event is direct CR event, and 2 events are possible background events. VPol signal region unblinding gives one neutrino candidate on a background of $0.34^{+0.66}_{-0.16}$; however, both the signal to background significance and post-unblinding analysis do not support a claim of a diffuse flux of UHE neutrino. The analysis efficiency for ANITA-IV is 70.7%. As the ν fluxes shown in Figure 7.8, the combined data from ANITA-I to ANITA-IV gives the lowest neutrino flux upper limit so far for energy above 4×10^{19} eV. The combined ν flux limit from several ANITA experiments is tricky because those experiments have different the number of observed ν candidates n_{obs}, background estimation b, effective area A_Ω, effective flight time T and analysis efficiency ε. The calculation of combined ν flux follows Equation 7.1, where the numerator N_{90} is calculated from summed n_{obs} and summed b and the denominator $A_\Omega T \varepsilon \Delta$ are summed from all the experiments.

There are still several things to be done beyond my current analysis: 1) estimate the energy of CR and neutrino candidates; 2) compare the spectrum of neutrino candidate event with simulated IceMC neutrino events; 3) need to figure out why the polarity uncertainty in HiCal is large compared to the previous flight (see Section 4.3).

Figure 7.9: The new beam-forming trigger proposed in ANITA-V. The beam-forming step increases the signal to noise ratio (SNR) in the power and can improve our sensitivity.

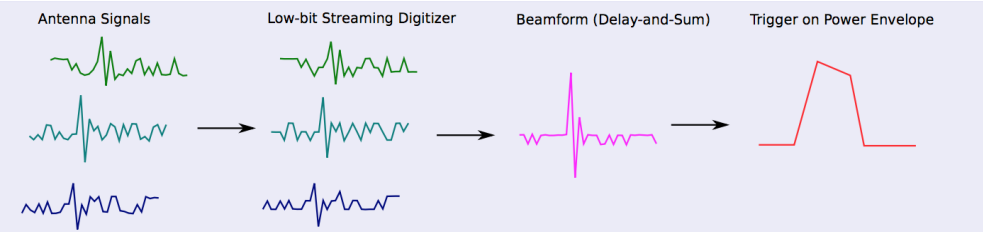

7.5 Outlook for ANITA-V

The ANITA collaboration is expected to propose for another science flight ANITA-V. Although the new design has not yet been finalized, there would be significant hardware changes in both trigger and digitizer.

As in Figure 7.9, instead of using three-level trigger logic in ANITA-IV, ANITA-V plans to have a realtime beam-forming trigger summing power through an FPGA board. A new Realtime Independent Three-bit Converter (RITC) will perform continuous and low-resolution digitization to carry out interferometry of all incoming waveforms in real-time [87].

The new high-resolution SURFv5 digitizer will have more even data sampling, wider bandwidth, and longer waveform by using new LABRADOR chips (LAB4D) [18]. Each SURFv5 board will have 12 new LAB4Ds. The LAB4D can digitize the data from RF change with 32 blocks of SCAs. The sampling rate of SCA is 3.2 Gsa/s. Eight of the 32 blocks will be used each time, so there are four buffers per LAB4D. The bandwidth of the SURFv5 would also increase as shown in Figure 7.10.

All these electronic upgrades will lead to less trigger deadtime and higher trigger efficiency and improve sensitivity to UHE cosmic ray and neutrinos. With the results from the previous ANITA flights, ANITA-V would further constrain the UHE neutrino parameter space or, very luckily, discover the first UHE neutrino event. Since a balloon-borne experiment like ANITA is far from the event vertex, it has relatively large neutrino energy threshold compared to ground-based experiments, such as ARA and

Figure 7.10: The bandwidth of SURFv5 compared with old ANITA SURF. Plot by Eric Oberla.

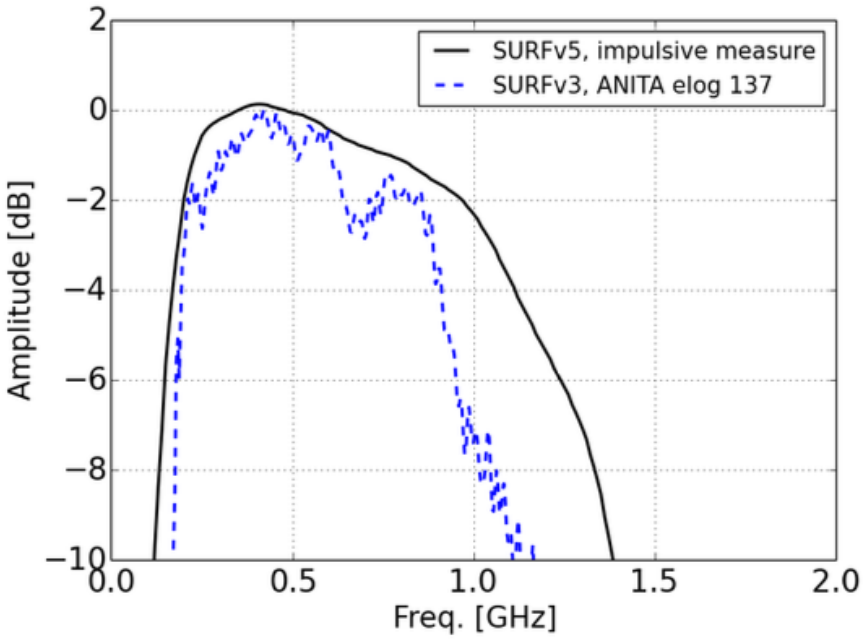

ARIANNA. It is exciting that ground-based experiments would have longer livetime and lower background. The mystery of cosmogenic neutrinos may soon be unveiled!

BIBLIOGRAPHY

[1] https://home.cern/science/physics/standard-model.

[2] K. Olive, et al. Review of Particle Physics. *Chin. Phys.*, C38:090001, 2014.

[3] Kumiko Kotera and Angela Olinto. The Astrophysics of Ultrahigh-Energy Cosmic Rays. *Annual Review of Astronomy and Astrophysics*, 49(1):119–153, 2011.

[4] Ben Strutt. A Search for Ultra-High Energy Neutrinos and Cosmic Rays with ANITA-III. *PhD thesis*, 2017.

[5] Raj Gandhi, Chris Quigg, Mary Reno, and Ina Sarcevic. Ultrahigh-energy neutrino interactions. *Astroparticle Physics*, 5(2):81–110, 1996.

[6] Amy Connolly, Robert S. Thorne, and David Waters. Calculation of high energy neutrino-nucleon cross sections and uncertainties using the Martin-Stirling-Thorne-Watt parton distribution functions and implications for future experiments. *Phys. Rev. D*, 83:113009, Jun 2011.

[7] John N. Bahcall. Solar Neutrinos: A Popular Account. *ArXiv*, page physics/0411190, November 2004.

[8] Markus Ahlers and Francis Halzen. High-energy cosmic neutrino puzzle: a review. *Rept. Prog. Phys.*, 78(12):126901, 2015.

[9] Kumiko Kotera, Denis Allard, and Angela V Olinto. Cosmogenic neutrinos: parameter space and detectabilty from PeV to ZeV. *Journal of Cosmology and Astroparticle Physics*, 2010(10):013, 2010.

[10] V.S. Beresinsky and G.T. Zatsepin. Cosmic rays at ultra high energies (neutrino?). *Physics Letters B*, 28(6):423 – 424, 1969.

[11] O. C. Allkofer. Introduction to cosmic radiation. *NASA STI/Recon Technical Report A*, 75, 1975.

[12] Jeferson A. Ortiz, Gustavo Medina-Tanco, and Vitor de Souza. Longitudinal development of extensive air showers: Hybrid code SENECA and full Monte Carlo. *Astroparticle Physics*, 23(5):463 – 476, 2005.

[13] Jaime Alvarez-Muñiz, Washington R. Carvalho Jr, Harm Schoorlemmer, and E Zas. Calculations of radio emission from ultra-high energy cosmic ray air showers: a practical approach. 02 2014.

[14] P. Gorham et al. *Phys. Rev. Lett.*, 99:171101, 2007.

[15] Ben Strutt. Cosmic Ray And Neutrino Astrionphysics With The ANITA-III Telescope. *PhD thesis*, 2017.

[16] P. W. Gorham et al. ANITA-IV Proposal. [ANITA internal notes].

[17] M. Mottram. A Search for Astrophysical Ultra-High Energy Neutrinos and Cosmic Rays with ANITA-II. *PhD thesis*, 2011.

[18] P. Allison et al. Dynamic tunable notch filters for the Antarctic Impulsive Transient Antenna (ANITA). *Nuclear Instruments and Methods in Physics Research A*, 894:47–56, June 2018.

[19] Oindree Banerjee, John Russell, and Peter Gorham. AMPA update: testing gain with network analyzer, 2016.

[20] Luke Batten, Linda Cremonesi, Carsten Hast, John Russell, and Nan Wang. AMPAs retested at LDB for gain and noise figure , 2016.

[21] Rene Brun and Fons Rademakers. ROOT-an object oriented data analysis framework. *Nuclear Instruments and Methods in Physics Research Section A: Accelerators, Spectrometers, Detectors and Associated Equipment*, 389(1-2):81–86, 1997.

[22] Ryan Nichole. AWARE website. http://www.hep.ucl.ac.uk/uhen/anita/aware/mapView.php.

[23] Ben Strutt et al. WAIS Divide Pulsing Notes. https://www.phys.hawaii.edu/elog/anita_notes/170222_052317/pulsingNotes.pdf, 2017. [ANITA internal notes].

[24] P. Gorham et al. The HiCal-2 Instrument: Calibration and Antarctic Surface Reflectivity Measurement for the ANITA Experiment. 2017.

[25] Pierre Auger Collaboration. Improved limit to the diffuse flux of ultrahigh energy neutrinos from the Pierre Auger Observatory. *Phys. Rev. D*, 91:092008, May 2015.

[26] IceCube Collaboration. Differential limit on the extremely-high-energy cosmic neutrino flux in the presence of astrophysical background from nine years of IceCube data. *ArXiv*, July 2018.

[27] Markus Ahlers and Francis Halzen. Minimal Cosmogenic Neutrinos. *Phys. Rev. D*, 86:083010, Oct 2012.

[28] The CMS Collaboration. Evidence for the direct decay of the 125 GeV Higgs boson to fermions. *Nature Physics*, 10(557), 2014.

[29] V. Hess. Über Beobachtungen der durchdringenden Strahlung bei sieben Freiballonfahrten. *Physikalische Zeitschrift*, 13:1084, 1912.

[30] Luis Alvarez and Arthur H. Compton. A Positively Charged Component of Cosmic Rays. *Phys. Rev.*, 43:835–836, May 1933.

[31] Pierre Auger, P. Ehrenfest, R. Maze, J. Daudin, and Robley A. Fréon. Extensive Cosmic-Ray Showers. *Rev. Mod. Phys.*, 11:288–291, Jul 1939.

[32] J. Linsley. Evidence for a Primary Cosmic-Ray Particle with Energy 10^{20} eV. *Physical Review Letters*, 10:146–148, February 1963.

[33] Andrew W. Strong, Igor V. Moskalenko, and Vladimir S. Ptuskin. Cosmic-Ray Propagation and Interactions in the Galaxy. *Annual Review of Nuclear and Particle Science*, 57(1):285–327, 2007.

[34] P. Goret, J. J. Engelmann, L. Koch-Miramond, J. P. Meyer, N. Lund, I. L. Rasmussen, and C. Perron. A comparison of the elemental abundances in the cosmic ray sources with local galactic and solar energetic particle abundances. *International Cosmic Ray Conference*, 9:122–125, 1981.

[35] Kenneth Greisen. End to the cosmic-ray spectrum? *Physical Review Letters*, 16(17):748, 1966.

[36] GT Zatsepin. GT Zatsepin and VA Kuzmin, JETP Lett. 4, 78 (1966). *JETP Lett.*, 4:78, 1966.

[37] Fred L. Wilson. Fermi's Theory of Beta Decay. *American Journal of Physics*, 36(12):1150–1160, 1968.

[38] Ivan Anicin. The Neutrino - Its Past, Present and Future. 04 2005.

[39] K. Kodama et al. Observation of tau neutrino interactions. *Phys. Lett.*, B504:218–224, 2001.

[40] B. T. Cleveland, T. Daily, et al. Measurement of the Solar Electron Neutrino Flux with the Homestake Chlorine Detector. , 496:505–526, March 1998.

[41] Q. R. Ahmad, R. C. Allen, et al. Measurement of the Rate of $\nu_e + d \rightarrow p + p + e^-$ Interactions Produced by ^8B Solar Neutrinos at the Sudbury Neutrino Observatory. *Phys. Rev. Lett.*, 87:071301, Jul 2001.

[42] Ziro Maki, Masami Nakagawa, and Shoichi Sakata. Remarks on the Unified Model of Elementary Particles. *Progress of Theoretical Physics*, 28(5):870–880, 1962.

[43] Y. Fukuda, T. Hayakawa, Ichihara, et al. Measurements of the Solar Neutrino Flux from Super-Kamiokande's First 300 Days. *Phys. Rev. Lett.*, 81:1158–1162, Aug 1998.

[44] Y FUKUDA, Takashi Hayakawa, et al. Atmospheric v ve ratio in the multi-GeV energy range. *Physics Letters B*, 335:237–245, 09 1994.

[45] R. Becker-Szendy, C. B. Bratton, et al. Electron- and muon-neutrino content of the atmospheric flux. *Phys. Rev. D*, 46:3720–3724, Nov 1992.

[46] http://www.kayelaby.npl.co.uk/atomic_and_nuclear_physics/4_7/4_7_1.html.

[47] Observation of a neutrino burst from the supernova SN1987A, author = Hirata, K. and Kajita, T. and others. *Phys. Rev. Lett.*, 58:1490–1493, Apr 1987.

[48] R. M. Bionta, G. Blewitt, et al. Observation of a neutrino burst in coincidence with supernova 1987A in the Large Magellanic Cloud. *Phys. Rev. Lett.*, 58:1494–1496, Apr 1987.

[49] ICECUBE COLLABORATION, FERMI -LAT, MAGIC, AGILE, ASAS-SN, HAWC, H.E.S.S., INTEGRAL, KANATA, KISO, KAPTEYN, LIVERPOOL TELESCOPE, SUBARU, SWIFT/NUSTAR, VERITAS, VLA/17B-403 TEAMS. Multimessenger observations of a flaring blazar coincident with high-energy neutrino IceCube-170922A. *Science*, 361(6398), 2018.

[50] Neutrino emission from the direction of the blazar TXS 0506+056 prior to the IceCube-170922A alert. *Science*, 361(6398):147–151, 2018.

[51] *The Pierre Auger Observatory: Contributions to the 34th International Cosmic Ray Conference (ICRC 2015)*, 2015.

[52] A. Aab et al. Inferences on Mass Composition and Tests of Hadronic Interactions from 0.3 to 100 EeV using the water-Cherenkov Detectors of the Pierre Auger Observatory. *Phys. Rev. D*, 96:122003, 2017.

[53] Katharine Mulrey. Characterizing radio emission from extensive air showers with the SLAC-T510 experiment, with applications to ANITA. *PhD thesis*, 2018.

[54] W. Heitler. *The Quantum Theory of Radiation*. Dover Books on Physics and Chemistry. Dover Publications, 1954.

[55] C. Patrignani et al. Review of Particle Physics. *Chin. Phys.*, C40(10):100001, 2016.

[56] Walter R. Nelson, Theodore M. Jenkins, Richard C. McCall, and Joseph K. Cobb. Electron-Induced Cascade Showers in Copper and Lead at 1 GeV. *Physical Review*, 149:201–208, 08 1966.

[57] Jaime Alvarez-Muniz, Andres Romero-Wolf, and Enrique Zas. Cherenkov radio pulses from electromagnetic showers in the time-domain. *Phys. Rev.*, D81:123009, 2010.

[58] G. A. Askaryan. *Soviet Journal of Experimental and Theoretical Physics*, 21:658, 1965.

[59] H. Falcke, P. Gorham, and R. J. Protheroe. Prospects for radio detection of ultra-high energy cosmic rays and neutrinos. , 48:1487–1510, December 2004.

[60] D. Saltzberg et al. *Phys. Rev. Lett.*, 86:2802, 2001.

[61] P. W. Gorham, D. Saltzberg, R. C. Field, E. Guillian, R. Milinčić, P. Miočinović, D. Walz, and D. Williams. Accelerator measurements of the Askaryan effect in rock salt: A roadmap toward teraton underground neutrino detectors. *Phys. Rev. D*, 72:023002, Jul 2005.

[62] K. Belov, K. Mulrey, A. Romero-Wolf, et al. Accelerator Measurements of Magnetically Induced Radio Emission from Particle Cascades with Applications to Cosmic-Ray Air Showers. *Phys. Rev. Lett.*, 116:141103, Apr 2016.

[63] H. Schoorlemmer and K. Belov and A. Romero-Wolf and D. García-Fernández and V. Bugaev and others. Energy and flux measurements of ultra-high energy cosmic rays observed during the first ANITA flight. *Astroparticle Physics*, 77:32 – 43, 2016.

[64] J. Jelley, et al. Radio Pulses from Extensive Cosmic-Ray Air Showers. *Nature*, 205:327, 1965.

[65] K. Belov, K. Mulrey, A. Romero-Wolf, S. A. Wissel, et al. Accelerator Measurements of Magnetically Induced Radio Emission from Particle Cascades with Applications to Cosmic-Ray Air Showers. *Phys. Rev. Lett.*, 116:141103, Apr 2016.

[66] P. Gorham, and P. Allison and B. Baughman, et al. The Antarctic Impulsive Transient Antenna ultra-high energy neutrino detector: Design, performance, and sensitivity for the 2006-2007 balloon flight. *Astroparticle Physics*, 32(1):10 – 41, 2009.

[67] P. Gorham, and P. Allison and S. Barwick, et al. New Limits on the Ultrahigh Energy Cosmic Neutrino Flux from the ANITA Experiment. *Phys. Rev. Lett.*, 103:051103, Jul 2009.

[68] P. Gorham, and P. Allison and B. Baughman, et al. Observational constraints on the ultrahigh energy cosmic neutrino flux from the second flight of the ANITA experiment. *Phys. Rev. D*, 82:022004, Jul 2010.

[69] P. W. Gorham, P. Allison, O. Banerjee, et al. Constraints on the diffuse high-energy neutrino flux from the third flight of ANITA. *Phys. Rev. D*, 98:022001, Jul 2018.

[70] Peter Gorham. ANITA SMEX proposal. https://www.phys.hawaii.edu/~gorham/ANITA/AnitaCSR.pdf.

[71] M. G. Aartsen, R. Abbasi, M. Ackermann, J. Adams, J. A. Aguilar, M. Ahlers, D. Altmann, C. Arguelles, J. Auffenberg, and et al. Bai, X. Probing the origin of cosmic rays with extremely high energy neutrinos using the IceCube Observatory. , 88(11):112008, December 2013.

[72] IceCube Collaboration. Evidence for High-Energy Extraterrestrial Neutrinos at the IceCube Detector. *Science*, 342:1242856, November 2013.

[73] Taylor Barrella, Steven Barwick, and David Saltzberg. Ross Ice Shelf (Antarctica) in situ radio-frequency attenuation. *Journal of Glaciology*, 57(201):61–66, 2011.

[74] Ara Collaboration, P. Allison, J. Auffenberg, R. Bard, et al. Design and initial performance of the Askaryan Radio Array prototype EeV neutrino detector at the South Pole. *Astroparticle Physics*, 35:457–477, February 2012.

[75] Jaime Alvarez-Muñiz et al. The Giant Radio Array for Neutrino Detection (GRAND): Science and Design. 2018.

[76] Ralph Engel. Upgrade of the Pierre Auger Observatory (AugerPrime). *PoS*, ICRC2015:686, 2016.

[77] E. Kido. The TA×4 Experiment. In *Ultra-High Energy Cosmic Rays (UHECR2016)*, page 011025, 2018.

[78] M. G. Aartsen, M. Ackermann, J. Adams, J. A. Aguilar, M. Ahlers, M. Ahrens, D. Altmann, et al. IceCube-Gen2: A Vision for the Future of Neutrino Astronomy in Antarctica. 2014.

[79] Abigail Vieregg. Private Communication of the Radio Neutrino Observatory from Abigail Vieregg.

[80] Cosmin Deaconu. UChicago ANITA-3 Analysis: Overview, Background Estimation, HPol Events, 2017.

[81] Steven Prohira. ANITA Internal Meeting. http://kicp.uchicago.edu/~avieregg/anitaAnalysisMeeting/021418/SP_021418.pdf.

[82] Konstantin Belov. ANITA Note. ANITA-IV Payload Geometry. https://www.phys.hawaii.edu/elog/anita_notes/170323_170625/ANITA-IV_McM_geometry.pdf, 2016. [ANITA internal notes].

[83] A. G. Vieregg. *The Search for Astrophysical Ultra-High Energy Neutrinos Using Radio Detection Techniques*. PhD thesis, University of California, Los Angeles, 2010.

[84] I. Kravchenko et al. RICE limits on the diffuse ultrahigh energy neutrino flux. *Phys. Rev. D*, 73:082002, Apr 2006.

[85] Gary J. Feldman and Robert D. Cousins. A Unified Approach to the Classical Statistical Analysis of Small Signals. *Phys. Rev. D*, 57:3874, 1998.

[86] P. W. Gorham, B. Rotter, P. Allison, O. Banerjee, et al. Observation of an Unusual Upward-Going Cosmic-Ray-like Event in the Third Flight of ANITA. *Phys. Rev. Lett.*, 121:161102, Oct 2018.

[87] K. Nishimura, M. Andrew, Z. Cao, M. Cooney, P. Gorham, L. Macchiarulo, L. Ritter, A. Romero-Wolf, and G. Varner. A low-resolution, GSa/s streaming digitizer for a correlation-based trigger system. *ArXiv*, March 2012.

Appendix

EVENT LIST FOR CR AND NEUTRINO CANDIDATES

Table A.1: Term definition in Table A.2, A.3 and A.4.

Term	Definition
event	The event number
time	UTC time
run	The run number
pol	The dominate polarization, with 0 for H and 1 for V
theta	Elevation angle at payload
phi	Azimuth angle at payload
snr	Signal to Noise Ratio in Deconvolved Summed Waveform
longitude	Intercept of arrival direction with the ice surface
latitude	Intercept of arrival direction with the ice surface
payloadLongitude	The longitude of payload at the time of the event
payloadLatitude	The latitude of payload at the time of the event
payloadAltitude	The altitude of payload at the time of the event
horizon	Elevation angle of arrival direction
p_ground	The probability of that the event is from ground
impulsivity	The impulsivity measure in the dominate pol
powerH	The total power in CSW of HPol
powerV	The total power in CSW of VPol
LinearPolFrac	Linear polarization fraction in the dominate pol
LinearPolAngle	Linear polarization angle in the dominate pol

Table A.2: The summary of 25 candidates (part 1)

event	time (s)	run	pol	theta (deg)	phi (deg)	snr	longitude (deg)	latitude (deg)
12131787	1481004034	90	0	-17.30	295.75	21.75	3.1366496	-78.09059
15738420	1481105460	104	0	-7.64	74.76	21.82	-56.65791	-76.33855
16821419	1481128623	107	0	-11.25	339.76	19.01	-59.62909	-77.14705
17904564	1481153050	111	0	-16.17	140.48	16.89	-54.72484	-78.80864
20936205	1481229953	121	0	-13.56	298.77	19.41	-88.57316	-76.03138
25580797	1481360136	139	0	-22.25	101.31	17.37	-121.5946	-81.44553
25855454	1481367999	140	0	-13.21	85.48	18.57	-119.0485	-78.99688
45684620	1481798889	200	0	-17.35	139.38	17.34	79.943793	-82.97518
35963950	1481592879	171	0	-31.74	249.16	15.59	167.17449	-83.06688
36785931	1481611879	174	0	-36.53	219.86	15.02	154.84765	-82.50869
39236841	1481662148	181	0	-8.45	346.68	20.40	123.83417	-79.84236
40172984	1481682502	184	0	-21.70	105.47	17.79	113.65821	-82.57714
47396999	1481833888	204	0	-15.27	107.55	19.68	62.573232	-81.88100
54063721	1481973903	224	0	-9.89	345.27	22.17	11.199702	-82.60776
64472798	1482212444	257	0	-26.08	121.64	16.92	-53.26098	-85.52373
64859493	1482222146	258	0	-19.72	130.90	16.34	-74.15743	-84.82921
64861754	1482222198	258	0	-21.73	151.19	16.46	-71.28959	-85.10125
66509677	1482259842	263	0	-8.91	244.64	19.64	-111.8776	-85.91676
72164985	1482388094	281	0	-6.17	201.99	20.82	-0.782681	-86.62659
83074427	1482649054	318	0	-7.29	327.14	15.50	-161.8937	-82.07579
88992443	1482791932	338	0	-14.82	54.55	15.53	159.10317	-85.66996
91525988	1482851016	346	0	-18.63	335.88	18.60	141.22118	-86.26595
93744271	1482901552	353	0	-29.97	123.19	16.16	147.47259	-87.89643
95576190	1482945371	359	0	-13.76	239.03	14.46	150.40268	-86.96689
69261214	1482322800	272	1	-13.46	300.78	20.03	-81.64195	-84.33753

Table A.3: The summary of 25 candidates (part 2)

event	payload Longitude (degree)	payload Latitude (deg)	payload Altitude (m)	horizon (deg)	p_ground
12131787	6.1087088	-78.97279	38613.52	-6.02	1.01
15738420	-42.44280	-77.27892	39506.70	-6.15	1.00
16821419	-51.69440	-78.06629	39446.71	-6.16	1.00
17904564	-58.48012	-77.81190	38925.00	-6.22	1.00
20936205	-85.18151	-77.30244	39443.33	-6.24	1.02
25580797	-120.8038	-80.63749	37701.73	-6.03	1.02
25855454	-122.5008	-80.29754	37504.95	-6.08	1.00
45684620	78.321365	-81.99905	37527.15	-5.94	1.01
35963950	164.73516	-82.58843	39148.65	-6.11	1.15
36785931	153.83769	-82.08718	38548.73	-6.05	1.00
39236841	130.40564	-82.02016	37451.39	-5.81	0.99
40172984	119.54671	-82.31624	38613.38	-5.91	1.02
47396999	68.630920	-81.22016	36376.83	-5.85	1.00
54063721	22.859579	-81.23259	39412.67	-6.19	1.00
64472798	-60.49925	-85.17269	38575.04	-6.03	1.00
64859493	-64.44461	-84.51849	38319.07	-6.18	1.01
64861754	-64.47505	-84.51482	38316.28	-6.16	1.01
66509677	-81.29826	-85.17917	39380.28	-6.32	1.00
72164985	-104.2873	-86.92644	38575.09	-6.03	0.90
83074427	-171.5618	-85.63632	39665.74	-6.30	1.00
88992443	141.73188	-85.74044	39277.30	-6.30	1.00
91525988	127.80501	-86.84223	39118.05	-6.27	1.01
93744271	140.55596	-87.39863	39572.65	-6.20	1.01
95576190	138.36908	-88.26123	38870.97	-6.12	1.00
69261214	-94.57179	-85.26274	39071.94	-6.25	1.00

Table A.4: The summary of 25 candidates (part 3)

event	impulsivity	powerH	powerV	linearPolFraction	linearPolAngle (deg)
12131787	0.90	83393.39	781.81	0.995	2.24
15738420	0.89	71457.13	14928.00	0.990	23.30
16821419	0.88	62289.43	5942.03	0.987	16.50
17904564	0.84	98172.23	43044.90	0.818	32.68
20936205	0.90	84055.96	8103.26	0.996	15.94
25580797	0.90	101823.39	1190.00	0.991	-6.20
25855454	0.87	46622.57	1434.23	0.984	7.88
45684620	0.91	314671.87	12565.04	0.999	11.58
35963950	0.81	112833.46	29965.42	0.639	-22.02
36785931	0.85	53421.74	4192.85	0.992	-4.50
39236841	0.88	68750.68	1413.13	0.992	-8.78
40172984	0.91	150491.85	3882.36	0.997	1.34
47396999	0.90	138242.14	5670.72	0.987	10.85
54063721	0.88	49584.96	1483.77	0.985	13.10
64472798	0.85	62086.22	3608.37	0.985	-9.84
64859493	0.87	80640.88	1437.74	0.992	9.33
64861754	0.85	36616.47	670.84	0.997	1.63
66509677	0.88	679465.87	3946.81	0.996	3.99
72164985	0.92	170552.00	16140.29	0.957	-14.23
83074427	0.91	527941.68	30378.92	0.990	12.60
88992443	0.82	39348.86	1174.28	0.969	11.03
91525988	0.82	26666.57	698.16	0.955	10.42
93744271	0.89	133184.85	6055.67	0.985	-0.75
95576190	0.82	22306.23	601.94	0.981	3.03
69261214	0.88	675.08	39112.68	0.957	87.89